



UNIVERSITAT POLITÈCNICA
DE CATALUNYA
BARCELONATECH

Numerical investigation and modelling of the unsteady behavior and erosion power of cloud cavitation

Linlin Geng

ADVERTIMENT La consulta d'aquesta tesi queda condicionada a l'acceptació de les següents condicions d'ús: La difusió d'aquesta tesi per mitjà del repositori institucional UPCommons (<http://upcommons.upc.edu/tesis>) i el repositori cooperatiu TDX (<http://www.tdx.cat/>) ha estat autoritzada pels titulars dels drets de propietat intel·lectual **únicament per a usos privats** emmarcats en activitats d'investigació i docència. No s'autoritza la seva reproducció amb finalitats de lucre ni la seva difusió i posada a disposició des d'un lloc aliè al servei UPCommons o TDX. No s'autoritza la presentació del seu contingut en una finestra o marc aliè a UPCommons (*framing*). Aquesta reserva de drets afecta tant al resum de presentació de la tesi com als seus continguts. En la utilització o cita de parts de la tesi és obligat indicar el nom de la persona autora.

ADVERTENCIA La consulta de esta tesis queda condicionada a la aceptación de las siguientes condiciones de uso: La difusión de esta tesis por medio del repositorio institucional UPCommons (<http://upcommons.upc.edu/tesis>) y el repositorio cooperativo TDR (<http://www.tdx.cat/?locale-attribute=es>) ha sido autorizada por los titulares de los derechos de propiedad intelectual **únicamente para usos privados enmarcados** en actividades de investigación y docencia. No se autoriza su reproducción con finalidades de lucro ni su difusión y puesta a disposición desde un sitio ajeno al servicio UPCommons No se autoriza la presentación de su contenido en una ventana o marco ajeno a UPCommons (*framing*). Esta reserva de derechos afecta tanto al resumen de presentación de la tesis como a sus contenidos. En la utilización o cita de partes de la tesis es obligado indicar el nombre de la persona autora.

WARNING On having consulted this thesis you're accepting the following use conditions: Spreading this thesis by the institutional repository UPCommons (<http://upcommons.upc.edu/tesis>) and the cooperative repository TDX (<http://www.tdx.cat/?locale-attribute=en>) has been authorized by the titular of the intellectual property rights **only for private uses** placed in investigation and teaching activities. Reproduction with lucrative aims is not authorized neither its spreading nor availability from a site foreign to the UPCommons service. Introducing its content in a window or frame foreign to the UPCommons service is not authorized (*framing*). These rights affect to the presentation summary of the thesis as well as to its contents. In the using or citation of parts of the thesis it's obliged to indicate the name of the author.



UNIVERSITAT POLITÈCNICA
DE CATALUNYA
BARCELONATECH

Numerical Investigation and Modelling of the Unsteady Behavior and Erosion Power of Cloud Cavitation

Article-Based Thesis

Doctor by the Universitat Politècnica de Catalunya

Presented to the Department of Fluid Mechanics of the
Universitat Politècnica de Catalunya (UPC) by

Linlin Geng

Under the supervision of
Professor Xavier Escaler

Barcelona, November 2020

Contents

ACKNOWLEDGEMENT	I
RESUM	II
ABSTRACT	IV
CAPTIONS	VI
NOMENCLATURE	VIII
CHAPTER 1 INTRODUCTION	1
1.1 BACKGROUND OF CAVITATION AND EROSION	1
1.1.1 <i>Cavitation</i>	1
1.1.2 <i>Cavitation Erosion</i>	4
1.2 STATE OF THE ART	8
1.2.1 <i>Modelling unsteady cavitation</i>	8
1.2.2 <i>Modelling cavitation erosion</i>	17
1.2.3 <i>Comment on the cavitation and erosion modelling</i>	21
1.3 OBJECTIVES	24
1.4 METHODOLOGY	24
1.5 ORGANIZATION OF THIS THESIS.....	25
CHAPTER 2 NUMERICAL APPROACH	26
2.1 TURBULENCE MODELLING	26
2.1.1 <i>Standard k-ε model</i>	28
2.1.2 <i>RNG k-ε model</i>	29
2.1.3 <i>The Wilcox k-ω Model</i>	29
2.1.4 <i>SST k-ω Model</i>	30
2.2 CAVITATION MODELLING	31
2.3 EROSION MODELLING	33
CHAPTER 3 ASSESSMENT OF URANS MODELS AND EMPIRICAL COEFFICIENTS	35
CHAPTER 4 IMPROVEMENT OF CAVITATION MODELS	36
4.1 CAVITATION MODEL CORRECTION	36
4.2 TEST CASES AND MESH CONVERGENCE STUDY	38
4.3 CAVITATION MODEL VALIDATION	40
CHAPTER 5 NUMERICAL PREDICTION OF CAVITATION EROSION	45
CHAPTER 6 CONCLUSIONS AND OUTLOOK	46
6.1 CONCLUSIONS	46
6.2 OUTLOOK	47
REFERENCES	48
ANNEXES	55
ANNEX A	55
ANNEX B.....	73

Acknowledgement

In the past three and a half years, I enjoyed my life in Barcelona and my research in the Department of Fluid Mechanics of UPC. All of these would not been achieved without the help of a number of people. First of all, I would like to express my deepest gratitude to my thesis supervisor, Professor Dr. Xavier Escaler. for his constant support. During these years, he always gives me his valuable and professional advices regardless of in life or in doing research.

I also would like to thanks to all my group members of CDIF, especially to Oscar De La Torre and Jian Chen for their kindly helps. Thank to my other colleagues of CDIF and the Fluid Mechanics Department for their kind treatment with me: Prof. Dr. Eng. Eduard Egusquiza, Dr. Eng. Carme Valero, Dr. Eng. Alfredo Guardo, Dr. Eng. Esteve Jou, Dr. Eng. Alex Presas, Dr. Eng. David Valentín Dr. Eng. Mònica Egusquiza and Eng. Rafel Roig Bauzà, to get along with them are very happy. Thanks to Weiqiang Zhao, Jian Chen, Ming Zhang for their accompanies during these years.

Finally, I want to express my gratitude to my parents who support me and give me motivations and courage for these years. I also would like to give the dearest gratitude to my wife Qian Huan, who always gives me her continuous support and love during these years. This work would not be possible without them. I hope I can spend more time with them in the future.

Special thanks should be given to the Chinese Scholarship Council (CSC), without whose financial support, it would be much more difficult for me to learn abroad.

Barcelona, October 2020

Linlin Geng

RESUM

La cavitació de núvol és un fenomen no desitjat que té lloc en moltes màquines hidràuliques que danya les superfícies de les parets sòlides a causa de l'agressivitat erosiva induïda pel procés de col·lapse. Per tant, és necessari predir amb precisió l'ocurrència de la cavitació de núvol i quantificar-ne la intensitat d'erosió per millorar el disseny i ampliar el cicle de vida de les màquines i sistemes existents. L'aplicació de la simulació numèrica (CFD) ofereix l'oportunitat de predir la cavitació inestable. Per a això, és de suma importància investigar com seleccionar els models més adequats per obtenir els resultats més precisos d'una manera eficient i com relacionar el col·lapse de les estructures de vapor amb el seu poder erosiu. En l'estudi actual, es s'ha avaluat la influència dels diferents models de turbulència i s'ha millorat el rendiment dels models de cavitació. La relació entre el comportament inestable i el seu caràcter erosiu també s'ha considerat implementant un model d'erosió.

Per a l'avaluació dels models de turbulència, s'han emprat tres models de turbulència Unsteady Reynolds Average Navier-Stokes (URANS) per simular la cavitació de núvol al voltant d'un perfil hidràulic NACA65012 en vuit condicions hidrodinàmiques diferents. Els resultats indiquen que el model Shear Stress Transport (SST) pot captar millor el comportament de la cavitat inestable que els models $k-\epsilon$ i RNG si la resolució de la malla propera a la paret és prou bona.

Per millorar els models de cavitació, s'ha investigat primerament la influència de les constants empíriques del model de Zwart en la dinàmica de la cavitat. Els resultats mostren que el comportament de la cavitat és sensible a la seva variació i, per tant, es proposa un rang òptim que pot proporcionar una millor predicció de la fracció de volum de vapor i del pic de pressió instantània generat pel col·lapse de la cavitat principal del núvol. En segon lloc, s'han corregit els models originals de cavitació de Zwart i Singhal tenint en compte el terme de segon ordre de l'equació de Rayleigh-Plesset. L'efectivitat dels models originals i dels corregits s'ha comparat per a dos patrons de cavitació diferents. Els resultats per una cavitat fixa demostren que el model corregit prediu millor la distribució de la pressió a la regió de tancament de la cavitat i la longitud de la cavitat en comparació amb les observacions de l'experiment. Els resultats per la cavitació de núvol inestable també confirmen que la predicció de la freqüència de despreniment es pot millorar amb el model Zwart corregit.

Per a la investigació del poder erosiu de la cavitació, es s'ha emprat un model d'erosió basat en el balanç energètic. S'ha comprovat que la distribució espacial i temporal de l'agressivitat de l'erosió és sensible a la selecció del model de cavitació i a la pressió motriu del col·lapse. En particular, l'ús de nivells mitjans de pressió combinats amb el model de cavitació de Sauer permeten obtenir resultats fiables. S'han observat dos mecanismes d'erosió, un que es produeix a la regió de tancament de la cavitat principal de la làmina caracteritzada per col·lapses de baixa intensitat però

amb alta freqüència, i l'altre induït pel col·lapse de la cavitat de núvol que presenta una alta intensitat d'erosió però amb baixa freqüència. Finalment, s'ha comprovat que la intensitat de l'erosió segueix una llei de potència amb la velocitat de flux principal amb exponents que oscil·len entre 3 i 5 segons el paràmetre d'estimació que s'utilitzi.

ABSTRACT

Cloud cavitation is a unwanted phenomenon taking place in many hydraulic machines which damages the surfaces of the solid walls due to the erosive aggressiveness induced by the collapse process. Therefore, it is necessary to accurately predict the occurrence of cloud cavitation and quantify its erosion intensity to improve the design and to extend the life cycle of existing machines and systems. The application of numerical simulation (CFD) offers the opportunity to predict unsteady cavitation. For that, it is of paramount importance to investigate how to select the most appropriate models to obtain more accurate results in an efficient way and how to relate the collapsing vapor structures with their erosion power. In the current study, the influence of the different turbulence models was assessed and the performance of cavitation models was improved. The relationship between the unsteady behavior and its erosion character was also considered by implementing an erosion model.

For the assessment of the turbulence models, three Unsteady Reynolds Average Navier-Stokes (URANS) turbulence models were employed to simulate the cloud cavitation around a NACA65012 hydrofoil at eight different hydrodynamic conditions. The results indicate that the Shear Stress Transport (SST) model can better capture the unsteady cavity behavior than the $k-\varepsilon$ and the RNG models if the near wall grid resolution is fine enough.

For the improvement of the cavitation models, the influence of the empirical constants of the Zwart model on the cavity dynamics was firstly investigated. The results show that the cavity behavior is sensitive to their variation, and thereby an optimal range is proposed which can provide a better prediction of the vapor volume fraction and of the instantaneous pressure pulse generated by the main cloud cavity collapse. Secondly, the original Zwart and Singhal cavitation models were corrected by taking into account the second order term of the Rayleigh-Plesset equation. The performances of the original and corrected models were compared for two different cavitation patterns. The results for a steady attached cavity demonstrate that the corrected model predicts better the pressure distribution at the cavity closure region and the cavity length in comparison with the experiment observations. The results for unsteady cloud cavitation also confirm that the prediction of the shedding frequency can be improved with the corrected Zwart model.

For the investigation of the cavitation erosion power, an erosion model based on the energy balance approach was employed. It has been found that the spatial and temporal distribution of the erosion aggressiveness is sensitive to the selection of the cavitation model and to the collapse driving pressure. In particular, the use of average pressure levels combined with the Sauer cavitation model permit to achieve reliable results. Then, two erosion mechanisms have been observed, one occurs at the closure region of the main sheet cavity characterized by low-intensity collapses but with high frequency, and the other is inducted by the collapse of the shed cloudy cavity which presents a high

ABSTRACT

erosion intensity but with low frequency. Finally, it has been found that the erosion power follows a power law with the main flow velocity with exponents ranging from 3 to 5 depending on the erosion estimate being used.

CAPTIONS

LIST OF FIGURES

Figure 1.1	Travelling Bubble Cavitation on the Suction Side of a Hydrofoil in a Hydrodynamic Tunnel. Reproduced from [2].	1
Figure 1.2	Typical visualization of tip and hub vortex cavitation on a propeller. Reproduced from [4].	2
Figure 1.3	Different cavitation patterns on a NACA 16012 hydrofoil. Reproduced from [1].	3
Figure 1.4	Leading Edge Cavity on the Suction Side of a Foil. Reproduced from [2].	4
Figure 1.5	The typical types of cavitation erosion in (a) Francis turbine and (b) Kaplan turbine. Reproduced from [6].	5
Figure 1.6	The pressure field when bubble collapses. Reproduced from [1].	6
Figure 1.7	Series of photographs showing the development of the microjet in a bubble collapsing very close to a solid wall. Reproduced from [9].	6
Figure 1.8	Typical examples of cavitation erosion impulsive loads measured using PVDF pressure. Reproduced from [15].	7
Figure 2.1	Physical cavitation erosion scenario based on the energy balance approach. Reproduced from [80].	33
Figure 4.1	Computational domains with named boundaries. Reproduced from [102].	39
Figure 4.2	Details of the mesh. Reproduced from [102].	40
Figure 4.3	Comparison between computed and measured C_p over NACA0009, $\sigma=0.9$. Reproduced from [102].	41
Figure 4.4	Vapor volume fraction distribution obtained by the original (top) and the corrected (bottom) cavitation model at $\sigma = 0.9$. Reproduced from [102].	41
Figure 4.5	Condensation rate distribution obtained by the original (top) and the modified (bottom) cavitation model at $\sigma = 0.9$. Reproduced from [102].	41
Figure 4.6	Comparison between the computed and the measured C_p values on the NACA0009 at $\sigma = 0.8$. Reproduced from [102].	42
Figure 4.7	Vapor volume fraction distribution obtained by the original (top) and the corrected (bottom) cavitation model at $\sigma = 0.8$. Reproduced from [102].	42

Figure 4.8	Comparison between the computed and the measured C_p values over the hemispherical body at $\sigma = 0.5$. Reproduced from [102].42
Figure 4.9	Vapor volume fraction distribution obtained by the original (top) and the corrected (bottom) cavitation model at $\sigma = 0.5$. Reproduced from [102].43
Figure 4.10	Comparison between the computed and the measured C_p values on the hemispherical body at $\sigma = 0.3$. Reproduced from [102].43
Figure 4.11	Vapor volume fraction distribution obtained by original (top) and modified (bottom) cavitation model, $\sigma = 0.3$. Reproduced from [102].43
Figure 4.12	Comparison of experimental and numerical cloud cavitation evolutions during one shedding period using the original and the modified cavitation models. The simulation results show an isosurface of $\alpha = 0.1$. Reproduced from [102].44

LIST OF TABLES

Table 1.1	Summary of the advantages and disadvantages of the turbulence models.12
Table 1.2	Summary of the advantages and disadvantages of the cavitation models.16
Table 2.1	Mathematical expressions of the cavitation models.32
Table 4.1	Flow conditions of the simulated cases. Reproduced from [102].39
Table 4.2	Features of the grids and numerical uncertainty evaluation based on the GCI indexes. Reproduced from [102].39
Table 4.3	Numerical and experimental shedding frequencies, deviations and improvements of modified models. Reproduced from [102].44

NOMENCLATURE

γ	Relative stand-off distance defined by $\gamma = H/R_0$ (-)
H	Distance between the bubble center and the solid boundary (m)
Re	Reynolds number (-)
N	Number of grid elements (-)
κ	Constant for computing the turbulent length scale near surface wall (-)
y	Distance from the wall (m)
T	Temperature (K)
p	Pressure (Pa)
μ	Viscosity (kg s/m ²)
ρ	Density (kg/m ³)
u, \bar{u}, u'	Velocity, time-average velocity, fluctuating velocity (m/s)
k	Turbulent kinetic energy (m ² /s ²)
ε	Turbulence dissipation rate (m ² /s ³)
ω	Turbulence frequency (1/s)
$C_{1\varepsilon}, C_{2\varepsilon}, \sigma_k, \sigma_\varepsilon, C_\mu$	Model constants for standard k - ε model ($C_{1\varepsilon}=1.44, C_{2\varepsilon}=1.92, \sigma_k=1.0, \sigma_\varepsilon=1.3, C_\mu=0.09$)
P_k	Production term of turbulence kinetic energy (kg/m/s ³)
F_{DES}	A limiter in DES model (-)
L_t	Character turbulence length scale (m)
Δ_{DES}	Mesh length scale (m)
C_{des}	Model constant for DES model (-)
L_{VK}	Von Karman length scale (m)
U''	Second velocity gradient (m)
Q_{SAS}	Source term in SAS-SST model (kg/m ³ /s ²)
F_1, F_2	Blending functions for SST model (-)
α	Vapor volume fraction (-)
p_v, p_∞	Vapor saturation pressure, Surrounding pressure (Pa)
\dot{m}	Mass transfer rate between the water and vapor phases (kg/m ³ /s)
α_{nuc}	Nucleation site volume fraction ($\alpha_{nuc}=0.0005$)
R, R_0, R_B	Bubble radius, initial bubble radius, bubble radius in Zwart model (m)

C_{prod}, C_{dest}	Empirical coefficients for vaporization and condensation (-)
U_{inf}	Inflow velocity of inlet (m/s)
C	Chord length (m)
V	Volume (m ³)
P_{pot}	Potential power (W)
E_{pot}	Potential energy inside a vapor structure (J)
P_{pot}^{mat}	Flow aggressiveness potential power (W)
P_{waves}^{mat}	Pressure wave power (W)
η^*, η^{**}	Energy transfer efficiency (-)
β	Mechanical transfer function (-)
ΔS	Area of analyzed sample surface (m ²)
\dot{R}, \ddot{R}	The first and second time derivative of bubble radius (m/s, m/s ²)
S	Surface tension (N/m)
P_G	the pressure of the non-condensable gas (Pa)

Subscripts

i, j, k	integer number
m, l, v	mixture, liquid, vapor
t	Turbulent

Abbreviations

DNS	Direct Numerical Simulation
SRS	Scale Resolved Simulation
URANS	Unsteady Reynolds Averaged Navier-Stokes
LES	Large Eddy Simulation
SAS	Scale Adaptive Simulation
DES	Detached Eddy Simulation
SST	Shear Stress Transport
RSM	Reynolds Stress Model
EVM	Eddy Viscosity Model
CFD	Computational Fluid Dynamics

NOMENCLATURE

VOF	Volume of Fraction
2D, 3D	Two Dimension, Three Dimension
EOS	Equation of State
TEM	Transport Equation Model
FSI	Fluid-Structure Interaction
CCFD	Computational Cavitating Fluid Dynamics
MPI	Message Pass Interface
ALE	Arbitrary Lagrangian Eulerian
CAI	Cavitation Aggressiveness Index
RNG	Renormalization Group

Chapter 1 Introduction

1.1 Background of Cavitation and Erosion

Cavitation is an unique phase changing phenomenon which is defined by the appearance of vapor phase due to a reduction in the local pressure to the saturation vapor pressure. Similarly, another well-known phenomenon is boiling that is defined as the transition of water into vapor by increasing the local temperature. Generally, the term cavitation is reserved for the condition in which the temperature of water is not changed because in the context of industrial and engineering hydraulic machines, the temperature change during the cavitation process can be ignorable and thus can be regarded as iso-thermal. However, in some cases like cryogenic-cavitating fluids, the thermal effects due to the latent heat transfer during the phase change process need to be considered. In addition, the cavitation can occur in any fluid, not just in water, like the blood in an artificial heart and all types of fluids transferred by pumps or valves. Because our interests are mainly studying the cavitation in hydraulic systems or components, the following section is particularly concerned with the cavitation in flowing fluids with a high Reynolds number.

1.1.1 Cavitation

Cavitation appears in hydraulic systems and components in various types of vapor structures depending on the properties of the fluid, the design of the geometry and the flow configuration. Generally, they can be classified into the following patterns:

(1) Travelling bubbles

As shown in Figure 1.1, this cavitation patterns takes a form of separated bubbles attached to the blade, which are developed in the low pressure region, flows downstream and finally implode when they are moving to the zone of higher pressure. The formation of his type of cavitation depends strongly on the water quality. In brief, this type of cavitation is sensitive to the liquid nuclei content and the pressure distribution [1].

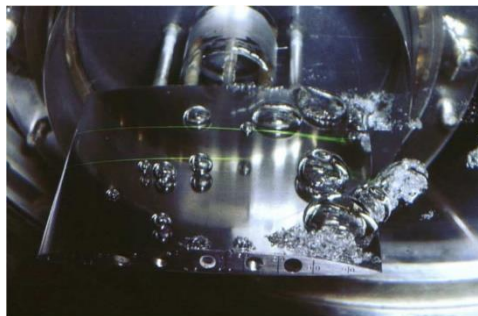


Figure 1.1: Travelling Bubble Cavitation on the Suction Side of a Hydrofoil in a Hydrodynamic Tunnel. Reproduced from [2].

(2) Vortex cavitation

This kind of cavitation occurs in the core of the vortex because of the fact that rotational flow generates a concentration of strong vorticity that creates a region with much lower pressure than far away. Such vortex cavitation tends to start even for a higher cavitation number than in other types of cavitation. It can often be observed at different fluid machineries. For example, as shown in Figure 1.2 at the tip of a propeller, a vortex forms due to the pressure difference between pressure side and suction side, the cavitation occurs in vortex core, which is an important source of the noise and vibration in the marine environment. And similarly another vortex cavitation is also observed in the downstream of the hub. In addition, the vortex cavitation commonly develops in hydraulic turbines, a typical example is the cavitation vortex-core flow below the runner cone in the center of the draft tube, which can provoke large pressure fluctuations. And other two examples are the inter-blade vortex cavitation and Von Karman vortex cavitation, more details can be found in reference [3].

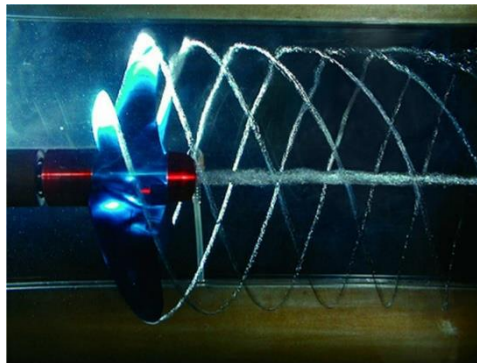


Figure 1.2. Typical visualization of tip and hub vortex cavitation on a propeller. Reproduced from [4].

(3) Shear cavitation, Cloud cavitation, Supercavitation and Attached cavitation

These different cavitation patterns can be visualized according to the cavitation number and the attack angle. Figure 1.3 maps the various types of cavitation observed on a NACA 16012 hydrofoil for a fixed Reynolds number at 1×10^6 . In this case, the water was deaerated so that the travelling bubble cavitation is no longer activated.

As shown in regions 1, 2 and 3, supercavitation appears for any attack angle when the cavitation number is small. In region 1, for small attack angles, the location of supercavity detachment is close to the rear part of the hydrofoil. When the angle of attack increases (region 2), the detachment point moves upstream and it is non uniform in span-wise direction. As the attack angle further increases, the detachment point comes to the leading edge and the whole hydrofoil is covered by the mixture of vapor and water. The evolution of detachment point is actually related to the nature of boundary layer which develops as a function of the attack angle. By the way, supercavitation can also be used for underwater vehicle drag reduction and noise suppression [5].

When cavitation number increases and the attack angle is larger than 4 degrees, three different cavitation patterns appears. In region 3', the partial cavitation occurs, which is famous by its unsteady behaviors, i.e. the sheet cavity periodically grows, sheds a cloud cavity and then it

collapses downstream. And for the higher attack angle (region 5), a shear layer between the main flow and the separated region forms with a high velocity gradient, which results in a higher concentration of vorticity. As a result, pressure in the shear flows drops to a low level so that cavitation appears. In addition, a narrow domain (region 4) exists as a transition area from region 3 to region 5. The cavity behavior in this region is also unsteady but not periodical, and the two phase cavity is featured with a foamy structure and a small void fraction.

In addition to the cavitation types shown in Figure 1.3, another commonly observed cavitation type is attached cavitation or sheet cavitation (see Figure 1.4). Such type of cavity is attached on the hydrofoil surface in a quasi-steady way. At their fore part, it is characterized with thin thickness, and with smooth and transparent interface, while at their rear part especially at the closure region, it presents a slight and weak pulsation because of the shedding of small vapor structures.

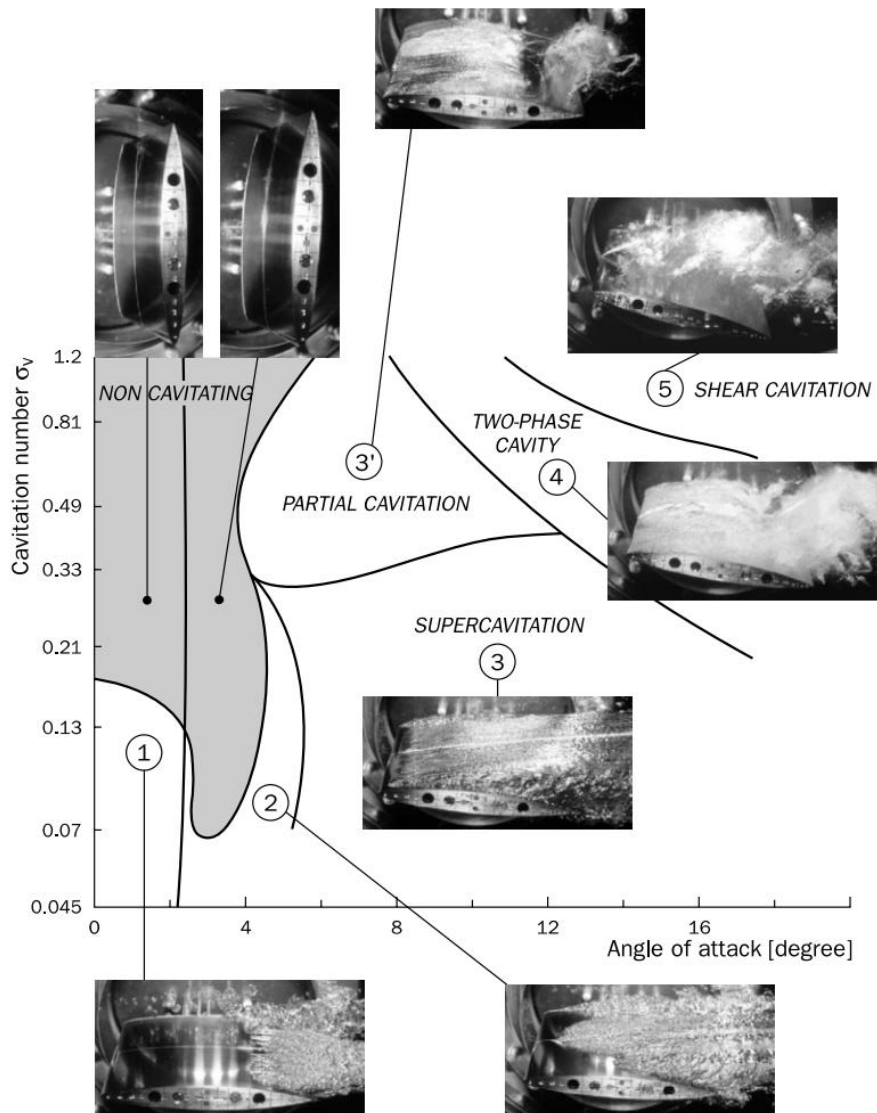


Figure 1.3. Different cavitation patterns on a NACA 16012 hydrofoil. Reproduced from [1].

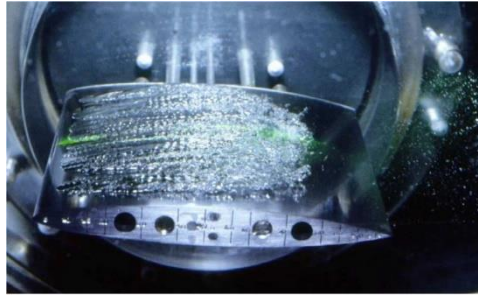


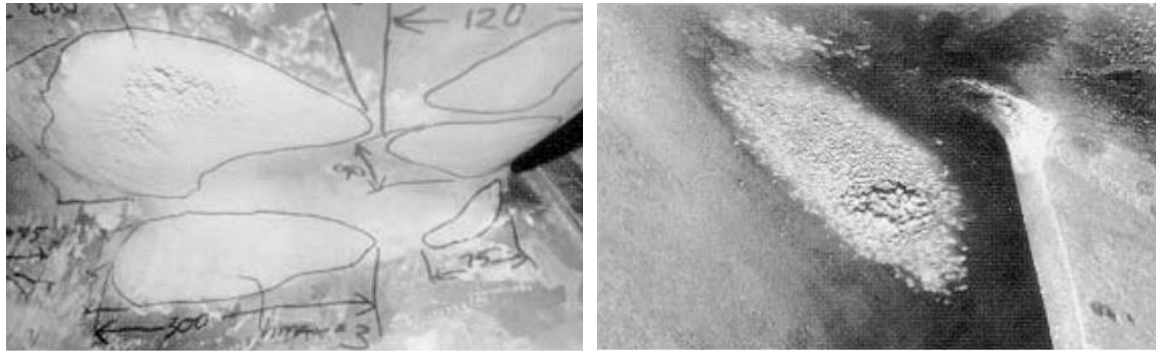
Figure 1.4. Leading Edge Cavity on the Suction Side of a Foil. Reproduced from [2].

Among these different cavitation patterns, the unsteady cloud cavitation is the most aggressive one. This is because when it takes place in hydraulic machinery it induces strong unsteadiness due to its dynamic behavior consisting of the cavity growth, the shedding and the collapse which are the cause of undesired effects like pressure fluctuations, noise generation and head drop. In addition, it is also the most erosive one because it always attaches to the blade and is accompanied by the near-wall induced bubbles collapses which are responsible for the surface damage. As a result, it is more and more important to know how to accurately model and predict this unsteady cavity behavior and to understand the relationship between the cavity behavior and its erosive power.

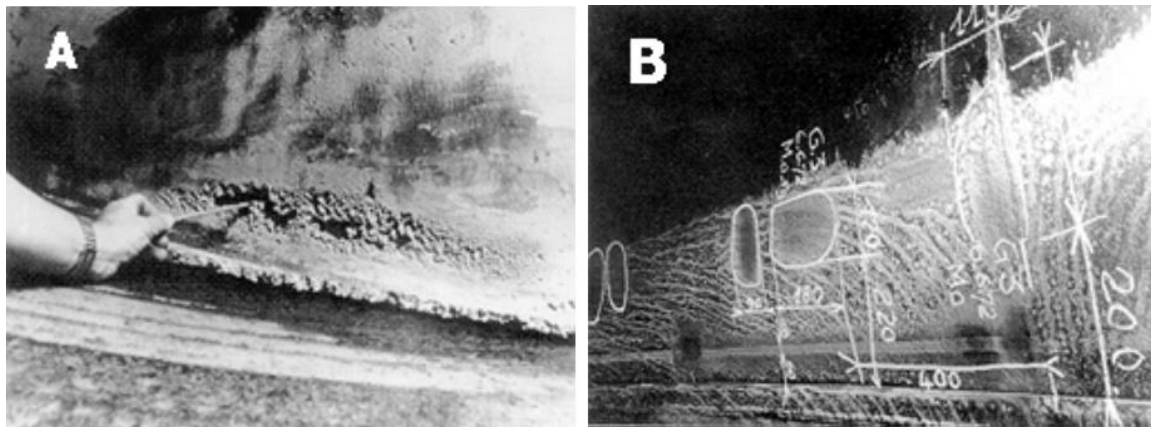
1.1.2 Cavitation Erosion

As a matter of fact, cavitation is generally a malevolent process because of the unwanted consequences in the flow field of hydraulic systems. For example, the deterioration of machine performance demonstrated by a dramatic drop of the turbine efficiency when the cavitation number is decreasing because the cavity develops and extends up to the throat of the flow passage in the impeller. The vibration and noise induced by the constant generation and collapse of vapor bubbles, which induces intense pressure fluctuations and the generation of noise and structure vibrations. For example, this can lead to an unsafe potential of a ship structure or a hydraulic installation. Besides it can also alter the stability of the machine operation [3,6].

Apart from the undesired effects mentioned above, another negative effect is the surface damage caused by cavitation erosion, which is perhaps the most damaging nuisance since it may cause severe material damage leading to increased maintenance costs, and deterioration in performance together with aggravated vibration and noise. Figure 1.5 shows some typical types of erosion in Francis and Kaplan runners. It can be observed from the left picture of Figure 1.5(a) that a damaged area with a “frosted” shape appears on the blade suction side due to the leading edge cavitation, and the inter-blade cavitation vortices provoke the erosion area on the runner hub (see Figure 1.5(a) right). And in Figure 1.5(b), for Kaplan turbine, the most critical erosion area can be found on the blades tips and the casing which is caused by the tip clearance cavitation.



(a)



(b)

Figure 1.5. The typical types of cavitation erosion in (a) Francis turbine and (b) Kaplan turbine. Reproduced from [6].

1.1.2.1 Cavitation Erosion Mechanisms

The cavitation erosion is mainly caused by two mechanisms, the first is the emission of high pressure shock waves. Figure 1.6 shows the pressure field during a bubble collapse which is theoretically derived based on the Rayleigh-Plesset equation. It can be seen that there is a maximum pressure pulse once the bubble has been compressed more than 0.63 times its initial radius. With further bubble compression, the maximum pressure continues to increase continually. When $R/R_0=1/20$ where R and R_0 are the bubble radius and the initial bubble radius, respectively, the maximum pressure can reach up to 1260 bars if the pressure difference between the surrounding pressure p_∞ and the saturation pressure p_v is one bar. And the amplitude of the pressure wave depends on the pressure difference and the radius of the bubble. In addition, if there is non-condensable gas inside the bubble, the non-condensable gas will work like a spring, leading to many rebounds and subsequent collapses which further result in successive emissions of pressure waves with attenuation.

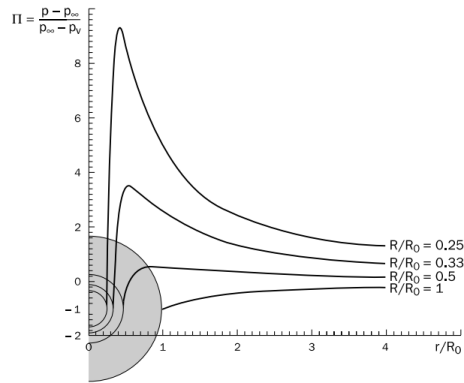


Figure 1.6. The pressure field when bubble collapses. Reproduced from [1].

The second mechanism is the formation of micro-jet. Figure 1.7 shows the formation of the micro-jet when the bubble collapses in the vicinity of a solid wall. When the bubble reaches its maximum radius, the pressure inside the bubble is much lower than the ambient pressure, leading to the collapse of the bubble. The fluid below the lower surface of the bubble is retarded due to the solid wall. This results in a low pressure and a high pressure on the lower and upper surfaces of the bubble, respectively. This pressure gradient causes a strong acceleration of the upper surface with a change in curvature. Therefore, a liquid jet forms and it is forced to hit the solid wall after penetrating the bottom surface of the bubble. Because the formation of the jet is caused by the asymmetry of the bubble evolution due to the existence of the boundary, the stand-off distance $\gamma = H/R_0$ is a main parameter that affects the property of the micro-jet. And according to Arvind's numerical and experimental study [7], an optimum standoff distance exists to that results in a maximum jet moment, and thus which has the maximum potential for erosion damage.

In addition, after the micro-jet pierces the lower surface, the initial bubble becomes a vapor torus that moves towards the solid wall. And almost at the same time, this torus may split into tiny bubbles, and evolve to a collective violent collapse with the emission of another shock wave, which is also aggressive [8].

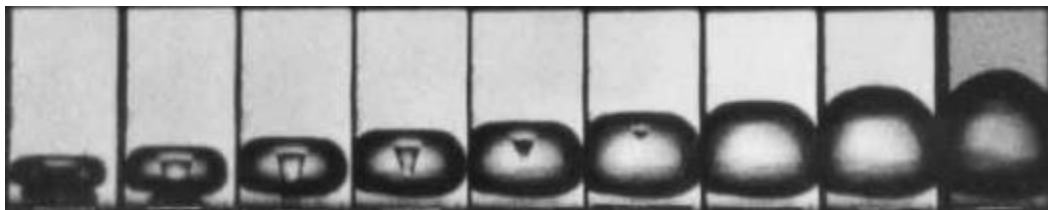


Figure 1.7. Series of photographs showing the development of the microjet in a bubble collapsing very close to a solid wall. Reproduced from [9].

A large number of experimental and numerical investigations have been carried out by different researchers to figure out which mechanisms mentioned above are more responsible for the cavitation erosion. However, all the studies reviewed so far did not reach any consensus. For example, Hammit

[10] pointed out that the cavitation erosion is due to micro-jets because the jet speed is able to reach the hundred m/s and generate impact pressures of the order of a hundred MPa. And Benjamin's study [11] support this hypothesis by comparison of the shapes of the holes obtained by a liquid micro-jet. On the other side, Fujikawa and Akamatsu [12] provided some experimental evidence and indicated that the water jet did not produce any detectable effects. In fact, they stated that the pressure wave had a much higher intensity with an order of 10^4 atm. Fortes-Patella et al. [13] simulated the dynamic response and surface deformation of different materials exposed to pressure wave impacts by numerical simulation, and she found that the numerically predicted pit profile and volume were in good agreement with the experimentally generated pit samples. Thus, it was concluded that the pressure wave is the main factor contributing to the cavitation damage. In addition, another finding by Tomita and Shima [14] demonstrated that the damage mechanism depends on the distance of the bubble away from the material surface.

1.1.2.2 Cavitation Erosion Characteristics

The erosion loads have the following features regardless of the erosion mechanisms:

(1) Short duration. Figure 1.8 shows the typical impulsive loads measured with a polyvinylidene fluoride (PVDF) pressure sensors [15]. It can be observed that the duration of the impact is only of the order of ten μs . And another experiment [12] measured an even shorter duration of 2-3 μs .

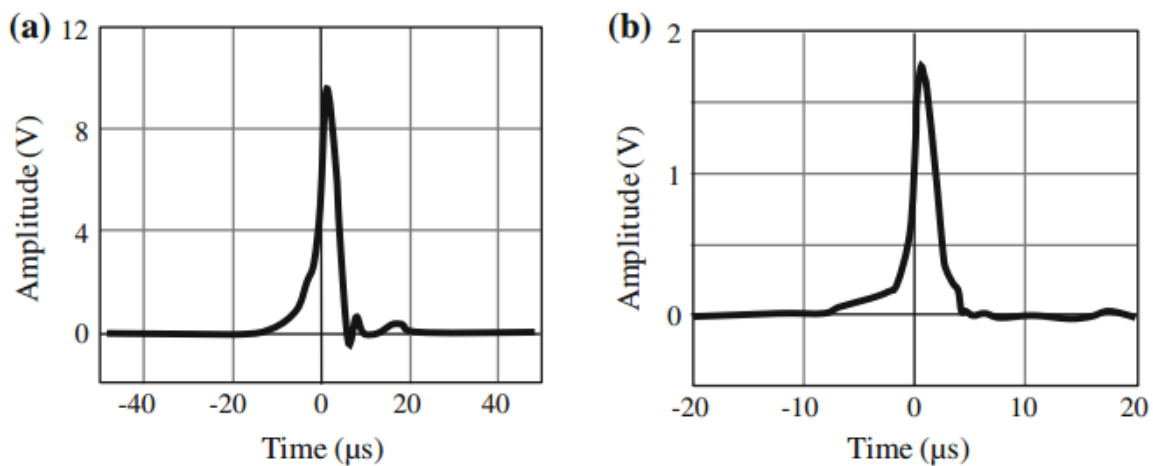


Figure 1.8. Typical examples of cavitation erosion impulsive loads measured using PVDF pressure. Reproduced from [15].

(2) Very small impacted area. The area subjected to the impacted is very small related to the size of the micro-jet which is always approximately one tenth of the maximum bubble size [16], and according to the pitting test experiment on Duplex Stainless Steel 2205 [17], the characteristic diameter of the pits lies in the range of 35–57 μm under different flow velocities.

(3) High amplitude. References [18, 19] have reported the amplitude of the impacts load is of the order of tens to hundreds of Newtons, and considering the small impacted area, the amplitude of the

pressure is able to reach the order of GPa. This high amplitude exceeds the yield stress of most engineering materials and explains the erosive potential of the cavitation.

(4) Highly repeated and randomly distributed impulsive. The intensity of the erosion is highly dependent on various physical parameters (e.g., bubble shape and size, distance from the wall, surrounding pressure, and material properties), and these parameters change with time especially for the highly unsteady cavitation flow, leading to a series of impacts developing spatially and temporally.

Therefore, it is very complex and difficult to measure the impact of a bubble collapse directly and accurately due to the above extreme features. The time scale is too short to enable a proper time response of the selected pressure gauge, the size of the area impacted is too small compared with the sensor surface which may lead to an underestimation of the pressure pulse, and the high amplitude of the impact can break the sensor if it is not resistant to the energy of the collapse. So in the experiment, the pitting test is often used as an indirect way to predict the impacts loads. With this method, the material itself is used as a sensor (limited to loads exceeding the material elastic limit) and each erosion pit is considered as the signature of an impact. The method consists of estimating the impact load which is at the origin of each pit from the geometric features of the pit and the properties of the material, which may be deduced from nano-indentation tests [15].

1.2 State of the art

Due to cavitation erosion, various hydraulic components including turbine runners, bearings and pump impellers may need replacement after several weeks or require a regular repair. Therefore, from an industrial point of view concerning both design and maintenance, the evolution of the erosive power of cavitating flows and the prediction of the cavitation erosion remains a major concern to manufactures and operators. And the unsteady cloud cavitation, considered the most erosive cavitation form, is the main research objective for cavitation erosion prediction. As a result, the accuracy of erosion prediction depends both on the modelling of the unsteady cavitation behavior and the estimation of the erosive potential.

1.2.1 Modelling unsteady cavitation

Unsteady cavitation flow often takes place at a high-Reynolds number, and it is essentially turbulent and is always related to vortex movement. Therefore, turbulence and cavitation modelling are both very important aspects for the accuracy of unsteady cavitation prediction and its erosive power.

1.2.1.1 Turbulence modelling

As it is well known, a turbulent flow is characterized by an unsteady character with a large range of scales of eddies. The objective of modelling the turbulence is to reproduce these various scales in

the turbulent flow by means of difference strategies. Generally speaking, and according to how to treat the various scales, the turbulence models can be divided into three strategies which are 1) Direct Numerical Simulation (DNS), 2) Scale Resolved Simulation (SRS) and 3) Unsteady Reynolds Averaged Navier-Stokes Simulation (URANS). These three strategies provide different levels of turbulent flow description, and thus they vary in complexity, range of applicability as well as accuracy. In the subsequent sections, these three strategies are described.

Direct Numerical Simulation means, as its name implies, numerically solving the Navier-Stokes equations directly with specifying appropriate boundary and initial conditions and without introducing any modelling. This method can describe perfectly the various scales of the motions in the turbulent flow, and its solution can also provide some interesting information that cannot be obtained readily by experimental measuring, like the vortex structure, the turbulent stress, and multi-time, multi-point statistics. Every coin has two sides, the drawback of this method is its applicability—it just can be used within a very narrow range. Because it aims to resolve the whole range of spatial and temporal scales of the turbulence, from the smallest dissipative scales (Kolmogorov microscales), up to the largest scale in the Energy-containing range, the computational cost is the main concern of its application. It is estimated that the computational cost required to perform a DNS grows rapidly as Re^3 where Re is the turbulent Reynolds number [20]. Therefore, for most engineering problems the flow tends to have a much higher Reynolds number, which leads to the fact that DNS becomes prohibitive and it is just a research tool for low or moderate Reynolds number flows. Recently, some researchers [21, 22] have only applied this method to simulate a single bubble's motion, and to predict cavitation in very small regions.

Scale Resolved Model (SRS). In this approach, the mean velocity and large scale of motions in a turbulent flow are regarded as more important because the energy and anisotropy are mainly contained in the large eddies, and the information of the smallest sizes is not so important. So the objective of SRS model is to resolve directly the motion of the larger eddies and modelling the eddies that are smaller than the mesh size.

The most known method one using this strategy is the **Large Eddy Simulation (LES)**. The idea of LES is based on a filtering operation which firstly decomposes any quantity into filtered and sub-filtered components by a filter function. Typically, the filter function is characterized by a length scale, i.e. the mesh scale. In physical space, the eddies with sizes larger than mesh scale are treated as large eddies and are directly resolved, while the eddies smaller than mesh scale are modeled. This filtering operation on the Navier-Stokes (NS) equations yields a sub-grid stress tensor which includes the effect of the small scales. So, the subgrid turbulent viscosity is introduced to compute the sub-grid stresses so that the governing system of equation is closed. Different subgrid turbulent viscosity models have been developed, the most classical one being the form of the Smagorinsky in 1963 [23]. The Dynamic Smagorinsky-Lilly model [24, 25] and the Wall-adapted Local Eddy-viscosity model

(LES WALE) proposed by Nicoud and Ducros [26] are also widely used. Because LES modelling can be considered as a “poor” DNS and it has a superficial ability to reproduce the real flow information, there are many limitations for its application. Firstly, LES is based on resolving most of the turbulent energy k whereas modelling most of the dissipation ε . This requires that at least 80% of k should be resolved to get a sensible result. And according to Pope’s theory [20], approximately 80% of the energy is mainly contained in the energy-containing range. This indicates that the mesh size must be smaller than the smallest eddy size in the energy-containing range, or in other words, the grid size must be located in the inertial subrange. This requirement may be easy to meet for high Reynolds number flow far away the boundaries but is very hard to achieve for high-Re flows near walls. Secondly, for modelling wall-bounded flow, the scale of the large eddies is linearly dependent on the wall distance, i.e., $L_t = \kappa y$, where κ is a constant and y is the distance from the wall [27]. Hence, the largest eddies become very small when they are close to the wall. This demands a high resolution in all three space dimensions and in time. And as Re increases, the large eddy size outside the viscous sublayer becomes smaller and smaller. Therefore, this restricts the application of LES for the modelling of most engineering flows. Reference [28] mentioned that when modelling free shear flows with LES, the number of grid elements, N , increased with scales $N \sim Re^{0.4}$, while when modelling wall-bounded flows, the computational cost requires scales in the range $N \sim Re^{1.76}$, which is comparable to DNS. Therefore, it is very expensive to use LES for simulations of complex wall-bounded engineering and environmental flows at high Reynolds numbers. Thirdly, there are some points which are important for the successful application of LES but they are always disregard. One affects the numerical discretization scheme especially for the convection term. It is recommended to use the central difference rather than the high resolution scheme because it is less dissipative. For the transient term, the transient scheme should select a 2nd Order Backward Euler scheme, and a very small time step should be set to meet the requirement of Courant numbers smaller than 1. Another one is the setup of the inlet boundary condition which can significantly affect the accuracy of LES particular for the cases of developing boundary layers or turbulent jets. All of these considerations sets a high threshold for the application of LES in industrial flows. This has motivated that a lot of researchers have developed hybrid SRS models.

Regarding the **hybrid SRS models**, one main strategy is to couple LES with a RANS model. Hybrid models are based on the idea that the large eddies are resolved only away from walls and the wall boundary layers are covered by a RANS model. Examples of such global hybrid models are Detached Eddy Simulation – DES or Scale-Adaptive Simulation – SAS.

DES is designed to treat the boundary layer with RANS and the free shear region in LES. DES model was firstly proposed by Spalart et.al. [29] based on the one-equation Spalart-Allmaras turbulence model [30]. And nowadays, DES theory can be applied to many turbulence models (e.g. $k-\varepsilon$, $k-\omega$, SST) in different versions. Here, we mainly describe the SST-DES model because it has

been further developed and it is also recommended to be used by FLUENT and CFX. For the DES-SST transport equation, the ω equation is the same as for the SST model, while in the k equation, the original dissipation term is changed multiplying by a limiter, F_{DES} ($F_{DES} = \max(L_{t-DES}/C_{DES}\Delta_{DES}), 1$), where L_{t-DES} , Δ_{DES} are the characteristic turbulence length scale and the mesh length scale defined by DES, respectively, and C_{des} is a coefficient of order 1. The value of F_{DES} equals to 1 for the region where the mesh has a length scale larger than L_{t-DES} , and thus the k equation remains unchanged and a RANS model is applied. On the other hand, the value of F_{DES} is larger than 1 when the mesh is refined below the limit $C_{des}\Delta_{DES} < L_{t-DES}$ making the dissipation term larger, which further decrease the turbulence kinetic energy and reduce the resulting eddy viscosity, and thus the model is switched to LES mode.

For the SAS-SST model [31], the k equation is exactly the same as for the SST model, while for the ω equation an additional source term is added. The value of this source term depends on the ratio L_{t-SAS}/L_{VK} , where L_{t-SAS} is the characteristic turbulence length scale defined by SAS and L_{VK} the Von Karman length scale. This von Karman length scale that includes the second velocity gradient U'' is used to detect the local unsteadiness which will create velocity gradients that decrease L_{VK} , causing an increase in the L_{t-SAS}/L_{VK} ratio and making Q_{SAS} term larger than zero. As a result, this source term increases the production of ω , and thus the turbulent viscosity is reduced because it is proportional to the k/ω ratio. Then the decreased turbulent viscosity allows the unsteadiness to remain. Such an approach ensures that local unsteadiness emerges.

Unsteady Reynolds Averaged Navier-Stokes (URANS) models, unlike the models described above, is at the opposite side of the strategies for treating turbulence because it just models all scales of the turbulence motion. It is based on the Reynolds decomposition in which every instantaneous quantity is decomposed into its time-averaged part and its fluctuating part. After applying Reynolds decomposition on the instantaneous Navier-Stokes equations, an unsteady Reynolds Averaged Navier-Stokes equation is formulated with a Reynolds stress term which represents the effects of turbulence. To close the Reynolds stress term, there are two different modelling approaches. The first and the most popular one is the Eddy-Viscosity Model (EVM), which invokes the Boussinesq approximation that enforces a linear relationship between the Reynolds stress tensor and the mean strain-stress tensor with a so-called eddy viscosity serving as the isotropic proportionality factor. These includes zero, one and two equation models where zero, one or two additional modeled PDE's are solved to provide estimates for the turbulent length and velocity scales to evaluate the eddy viscosity in a dimensionally consistent fashion. Typical examples of such models are the $k-\varepsilon$ or the $k-\omega$ models in their different forms. Another one is the Reynolds Stress Model (RSM) in which an additional set of 6 modelled PDE's are solved to determine the Reynolds stress tensor directly without introducing the isotropic eddy viscosity assumption.

As a summary, there is no perfect turbulence model suitable for simulation all varieties of flows at least for the current level of development. Table 1.1 summarizes the advantages and disadvantages of the turbulence model described in the previous paragraphs.

Table 1.1 Summary of the advantages and disadvantages of the turbulence models.

Model		Advantages	Disadvantages
DNS		Reproduce the whole range of scales of motions of the turbulent flow and obtain flow information that is hard to measure in the experiment.	The computational cost grows rapidly as Re^3 , impractical for simulating the high Reynolds number flows.
SRS	LES	Directly resolve over 80% of the turbulent kinetic energy, provides closest results to DNS.	Very expensive for simulating wall bounded flow, Demanding numerical setting (discretization scheme, boundary condition)
	Hybrid SRS	Potential for improved accuracy when the resolution of the largest eddies is high.	Require higher mesh resolution and small time steps, long run times and large volumes of data.
URANS	EVM	Robust, easy to converge, economical computational cost, most widely used for most engineering application.	Fails to predict flows with sudden changes in mean strain rates, flows over curved surface and swirling flows.
	RSM	Physically the better URANS model, avoid isotropic eddy viscosity assumption.	Requires more CPU time and memory, hard to get well converged results.

1.2.1.2 Cavitation modelling

Cavitation flow is essentially a two phase flow with phase changing which involves the resulting mass and heat transfer between water and vapor phases. This type of flow is also characterized by a large difference of material properties between the phases. The density ratio of water to vapor is in the order of 10^4 and the sound speed in a cavitating flow ranges from less than 10 to more than 10^3 m/s. In addition, the flow is involved in complex multiple length scale nature phenomena, ranging from micron-scale nuclei bubbles to meter-scale large gas/vapor cavities. Moreover, it involves very complicated inter-scale transformations between the micro and macro scales as bubbles grow or merge to form larger bubbles or even cavities, or as bubbles shrink or break up from a large cavity. All of them make modelling a cavitation flow numerically challenging. Nowadays, with the development of CFD and the introduction of different assumptions, different cavitation modelling strategies has been extensively developed, which can be classified into two different categories according on how to treat the vapor phase. These two categories are the Euler-Lagrange, and the Euler-Euler approaches. These methods are described as follows.

1.2.1.2.1 Euler-Lagrange

In this approach, the liquid or the vapor/liquid mixture is treated as a continuum fluid and computed

in the Eulerian frame, where the continuity equation, momentum equations and energy equation for the mixture are solved. And the nuclei and microbubbles are treated as a dispersed phase and they are tracked in a Lagrangian framework where the dynamic behavior of these bubbles, including the bubble expansion and bubble shrinking, is solved with the Rayleigh-Plesset equation. The bubble trajectories can be obtained by solving the Newtonian motion of bubbles driven by a surrounding flow field. The above Euler-Lagrange has been widely accepted and used, however, there are still some problems when using this method.

Typically, a one-way coupling is used, i.e., the solution of the Eulerian field is imposed on the Lagrangian frame and the bubbles do not influence the liquid phase, and different forces are considered to act on bubbles such as drag, lift, pressure gradient force, shear force, etc. [32]. An overview of these forces acting on spherical bubbles and their influence on the bubble's trajectory can be found in [32, 34]. This one-way strategy is suitable to investigate cavitation inception in vortex flow. However, for developed cavitating flows the interaction between the liquid and vapor parts should be taken into account in both ways. Unfortunately, there are few researches considering this two-way coupling. Giannadakis et al. [35] used a source term in the momentum equation of the continuous phase to consider the exchange of momentum between the phases, and Abdel-Maksoud et al. [33] developed a two-way coupling concept based on the definition of volume fractions.

In addition, this approach involves different length scales from micro-scale dispersed bubbles to macro-scale vapor/liquid interfaces, the inter-scale transition and the relative scale of the bubble and grid cell. Furthermore, this method also needs to consider the bubble coalesce, the bubble breakup, and the bubble-bubble interactions etc. Hence, it is a big challenge on numerical scheme to accurately address the inter-scale transition because the sudden appearance of new/liquid interfaces imposes a strong disturbance in the solution domain, leading to the numerical instability and spurious pressure pulses and spurious vapor generation. To solve this problem, some investigation has been conducted. For example, Apte et al. [36] have implemented the collision of bubbles via a standard collision model, Ghahramani et al. [37] reformulated the coupling between the bubbles and the Eulerian governing equations to include the effects of bubbles on the Eulerian flow with higher accuracy. Hansch et al. [38] proposed a clustering-method, and suggested introducing extra "clustering" forces in the fluid cells when the vapor volume fraction is larger than a critical value. These forces then cause an aggregation of dispersed bubble volumes till the formation of air cavities, which in turn are to be resolved by Volume of Fraction (VOF). Hsiao et al. [39, 40] developed a meso-scale transition scheme to allow smooth transfer from dispersed small bubbles into large cavities by bridging a Level Set method for large size cavities and a Discrete Singularity Model for small bubbles.

Another controversial issue is how to release the bubbles and how to determine the bubble size and bubble density. References [41, 42] proved that the choice of nuclei population is crucial for the

successful application of the Eulerian-Lagrangian method. But various release methods have been used by different researchers. Eskilsson [43] set a plane ahead of the hydrofoil and injected 100 bubbles in a 20×5 matrix at every time step. Ochiai et al. [44] introduced the bubbles to the Eulerian field from five points ahead of the hydrofoil. Hsiao et al. [45] injected the cavitation nuclei from a plane upstream of the cavitation zones. However, in reference [40], Hsiao et al. proposed another novel approach by taking into account the nuclei from the foil surface, in which nuclei are released from the foil boundary cell when the pressure at the cell center drops below a threshold value, and they also suggested that some bubble releasing parameters can be a function of surface roughness, temperature and other physical-chemical parameters. In addition, for the vortex cavitation prediction, the bubble is always tangentially released from different radial distances away from the vortex axis [39, 41].

1.2.1.2.2 Euler-Euler

In practice, a two-phase bubbly flow usually contains a very large number of dispersed bubbles which can be modeled using averaging techniques. Continuum-based approaches are typically used in cases where bubbles are much smaller than the characteristic lengths associated with the motion of the overall mixture. In this case, the precise location and properties of individual bubbles are not directly apparent at the global mixture flow scales. The bubbles are instead considered collectively via the equivalent continuum mixture [39]. Therefore, in this method, liquid and vapor are both considered a continuum phase. And according to reference [46], this approach can be subdivided into two classes, the first class corresponds to Euler multi-fluid models and the second class to Euler single fluid models.

Euler Multi-Fluid

For this approach, liquid and vapor phases are both treated mathematically as a continuum. The fluid phases are simulated separately using multiple sets of balance equations. Each set describes the motion of the corresponding fluid, which has its own pressure, velocity, and temperature. In addition to the balance equations, a transport equation for the volume fraction evolution of one of the fluids is also solved to track the different fluids. And the interaction between water and vapor phases is calculated with interfacial transfer terms for heat, mass and momentum exchange. This approach is usually called the multi-fluid seven-equation model, or the parent model. The most complete seven-equation model is proposed by Baer et Nunziato [47], which considers the non-equilibrium effects between phases (unequilibrium of pressure, velocity and temperature). For example, this seven equation model has been used for supercavitation and expansion tube problems by Saurel [48, 49]. However, this method is considered to be expensive because it deals with the solution of a large system of equations, that is, 12 equations for a two-dimensional (2D) two-phase case and 14 equations for a three-dimensional (3D) case if the fluid is considered to be compressible. Afterwards, this seven equation model was reduced to a six equation version based on either having two pressures

with a single velocity and two temperatures or a single pressure, two velocities, and two temperatures [50, 51]. Kapila et al. [52] further reduced it to five equations by assuming the equilibrium of pressures and velocities between the phases, which thus consists of two continuity equations, one momentum equation, one energy equation and one volume fraction transport equation. This five equation model involves two temperatures which makes it possible to take into account the effects of thermodynamic imbalances between phases, as indicated in the model of Saurel [46] for cavitation simulation in diesel injectors.

Euler Single Fluid method

For this approach, the multiphase flow is considered to be one single fluid and two categories belong to this approach which are the Single-Phase Interface Tracking model and the Homogeneous Mixture model.

For the Single-Phase Interface Tracking Model, in this model, only the liquid phase is considered and the cavity region is assumed to correspond to the constant pressure region where the magnitude of the pressure is equal to the vapor saturation pressure. Therefore, this model is computationally achieved by seeking a liquid-vapor interface which can be tracked based on the above assumption. The deformation algorithm of the liquid-vapor interface is based on the idea of adapting the cavity shape in an iterative way until the vapor pressure is reached in the cavity boundary. The deformation procedure is performed according to the pressure distribution on the blade obtained from the liquid flow computation of the previous iteration [53]. The detailed description of this method can be found in Chen and Heister [54] and Deshpande et al. [55]. Although this method is proved to be capable of simulating steady sheet cavitation, it may not be adequate for predicting the unsteady cavitation [56].

For Homogeneous Mixture Model, in this model, the two phases are assumed to be in thermal and mechanical equilibrium, what it means that they share the same temperature T and the same pressure p . Thus, these two phases are considered to be a single mixture, and the properties of the mixture are defined as the summation of the separate equations of the phase quantities. As a result, the governing equations of the compressible mixture are the continuity, momentum and energy equations. To close the governing system, it is necessary to link the pressure to the thermodynamic variables. Nowadays, two strategies can be used to compute the density field which are based on either an equation of state (EOS) or on a volume fraction transport equation.

The former approach, EOS, assumes that the mass transfer between liquid and vapor phases occurs instantaneously. And the difficulty of this approach is the specification of a reasonable equation of state that should covers three possible states: pure liquid, pure vapor and two-phase mixture. Typically, the influence of thermal effects is not taken into account because for cold water or more generally for a non-thermosensitive fluid the dynamic and thermal phenomena are decoupled, so the energy equation is not necessarily included. But note that it is necessary to include the equation of

energy for thermosensitive fluid [57]. Typically, the Tait law and perfect gas law were used to take into account the compressibility of pure liquid and pure vapor [58]. For the mixture state law which control the phase change, literature [57] summarized several types of relations, among which there is the Sinusoidal [59] and the Schmidt's [60] barotropic laws. In addition, the viscosity for the pure liquid is determined by an exponential law, that for the pure vapor follows the Sutherland law, and that for the mixture is defined as the arithmetic mean of liquid and vapor viscosities [58].

However, this model cannot take into account the mass transfer within the cavitation, and it cannot capture the baroclinic vorticity production term that occurs in the vorticity transport equation which is equal to zero in a barotropic state law because the density and pressure gradients are parallels [61]. In addition, Mani et al. [62] also demonstrated that this strategy is very sensitive to the turbulence closure model.

The second approach is to solve an additional volume fraction transport equation (TEM) with an appropriate source term accounting for the mass transfer rate between the water and vapor phases. The source terms defined by different formulations are so called cavitation models. This method has the apparent advantages that, for example, the transport equation has the convective character, which allows modelling the impact of inertial forces on the cavities [56], and this method take the mass transfer rate between phases into consideration. Furthermore, in contrast to the EOS, this model can capture the baroclinic vorticity production because the gradient of density and pressure are not necessarily parallel. All these merits attracted a lot of researchers who developed different cavitation models based on the TEM. An overview of these models can be found in [63], and some of them have been set as the default option in popular CFD softwares. For instance, the Zwart model [64] and the Kunz model [65] are the native cavitation models in CFX® and OPENFOAM®, respectively. Meanwhile, Fluent® has adopted the Singhal [66] and Sauer [67] cavitation models. However, the main drawback of these TEMs is that almost all cavitation models introduce empirical constants to regulate the mass transfer rate, and these constant are not universal and need to be tuned according to the case being simulated.

In summary, the Table 1.2 summarizes the main advantages and disadvantages of the cavitation models.

Table 1.2 Summary of the advantages and disadvantages of the cavitation models.

Model		Advantages	Disadvantages
Euler-Lagrange		Best theoretical background, capable to capture the bubble dynamics	Coupling between Eulerian and Lagrangian fields, numerical complexity for inter-scale transition, sensitivity to bubble release on the result.
Euler Multi-Fluid		Capable of considering the thermodynamic or kinetic non-equilibrium effects.	Challenging and expensive for numerical computation, suitable for inviscid flows and simple geometries.
Euler	Interface	The cavitating flow region is	Hard to deal with the unsteady

Single Fluid	Tracking Model	assumed to be at a constant pressure equal to the saturation pressure	and detached cavitation.
	Homogeneous Mixture with EOS	Density and pressure are coupled by an EOS or an arbitrary barotropic equation.	Fails to capture vorticity production in the closure region; sensitive to the turbulent closure model.
	Homogeneous Mixture with TEM	Considers the mass transfer between phases, capable of capturing the vorticity production, easy to couple with turbulence models	Lack of reliable empirical constants for different flows.

1.2.2 Modelling cavitation erosion

The evaluation of the erosive power of cavitating flows and the prediction of the material damage remains a major concern to manufacturers and operators. In this sense, several methodologies have been developed to predict cavitation erosion using Computational Fluid Dynamics (CFD) and Structural Mechanics [68]. And according to already existing literatures, the method used to predict cavitation erosion by CFD can be divided into two classes: fluid-structure interaction (FSI) and computational cavitating fluid dynamics (CCFD).

1.2.2.1 Fluid-Structure Interaction

The FSI method can be subdivided into two categories which are the two way FSI and the one way FSI, respectively. The former one models the cavity collapse in the fluid domain and computes the material response in the solid domain. The latter one only applies the impact load, which is obtained by the pitting tests, to the solid domain and calculates the material response. There are some applications of the two categories developed by several researchers.

Regarding the two way FSI, Hsiao et al. [69] developed an in-house code which links an incompressible boundary element method solver and a compressible finite difference flow solver to capture non-spherical bubble dynamics efficiently and accurately. The flow code solves the fluid dynamics while intimately coupling the solution with a finite element structure code to enable simulation of the FSI. During bubble collapse, high impulsive pressures generate from the impact of the bubble re-entrant jet and from the collapse of the remaining bubble ring. A pit forms on the material surface when the impulsive pressure is large enough to make high equivalent stresses exceeding the material yield stress. These codes seem to provide a good solution between the flow field and material surface based on FSI. On the other hand, Paquette [70] developed a strategy that coupled the fluid and the solid solver by MPI (Message Pass Interface). For the fluid part, the compressible Arbitrary Lagrangian Eulerian (ALE) fluid solver was used to determine the pressure exerted by the fluid. For the solid part, the code CAST3M® was employed to model the displacement and velocity of the solid.

The one way FSI aims to model the response of the material to repeated impact loads. As a result, this method has two issues to solve, the first one is to determine the characteristics of the impact load, including its amplitude, duration, and diameter. The second is to simulate the behavior of the material with increasing number of impact loads, which includes the determination of the stress-strain relationship at a high strain rate, a reasonable model for fatigue taking the hardening mechanism into account, and an appropriate failure model for damage [71]. Roy et al. [72] assumed that the impact loads have a pressure distribution with a Gaussian shape and applied this load shape with different peak pressures and various peak sizes. They found that the load with a Gaussian pressure distribution is reasonable because the computed mean pit shape is close to the experimental pit shape, and that the pressure and the pit parameters have a one-to-one correspondence. Finally, they proposed an inversely analytical equation by which the impact load can be predicted with a given pit parameter, however this equation is material dependent. Thereafter, they analyzed the influence of strain rate sensitivity of the material on the erosion by investigating the effect of impact duration on the pit formation [73]. As a results, they indicated that the erosion resistance is higher for the material with a higher strain rate sensitivity and that a detectable pit may not form if the impact duration is quite short compared to the characteristic time of the material defined on the basis of its natural frequency, i.e. in the order of less than a nanosecond, even though the impact peak pressure is much higher than the yield strength of that material. In addition, Fivel et al. [71] modeled the material behavior under repetitive impact loads by proposing the kinematic hardening to account for the progressive increase in the plastic strain and by introducing a scalar damage variable, D , which is equal to 0 when material is intact and equal to 1 when the fracture occurs. Based on this variable, the evolution of the material fatigue, damage initiation and failure was simulated. However, they acknowledged that the method was too simple and needed further research to be confirmed. Similarly, the damage variable, D , was also used by Patella et al. [74] to predict the mass loss period. However, unlike the damage variable defined by Fivel M et al. [71], in which D is related to the cumulated plastic strain and two critical plastic strain are set corresponding to the damage initiation ($D = 0$) and failure ($D = 1$), Patella et al. [74] correlated D with three parameters related to material fatigue behavior, to energy transfer relationship between pressure wave and material, and to dimensionless passage time of the pressure wave responsible for the material damage, respectively. And finally different stages of the evolution of the material erosion were well predicted and the time duration of the incubation period and the steady-state erosion rate were determined from numerical simulations.

The two-way FSI simulation shows a great potential for modeling the cavitation erosion because it is more realistic since it considers the material's response. With this method, the whole damaging process including the generation of the pressure loading resulting from the micro-jet or the bubble collapse (or even the collapse of the remaining bubble ring), the propagation of the pressure wave,

and the time evolution of the stress distribution inside the material are considered in the simulation., The parameters influencing the intensity of the pressure loading such as the bubble volume, the standoff distance and even the bubble number can also be controlled to analyze the mechanism behind the cavitation erosion. As for the one-way simulation, the behavior of material to cavitation erosion can be simulated as long as the material property can be well defined, and the different stages of the material exposed to repetitive impact loads including plastic deformation, the hardening process, the damage initiation, and the final failure can be reproduced. However, this method has its limitations and disadvantages.

For the present application, the simple elastic-plastic model is only considered for the solid response when conducting the two-way simulation, therefore the following advanced stages of erosion are not well simulated. Moreover, this method nowadays can only model the material response under the collapse of a single bubble or a bubble cloud which is too simple compared to the erosive cavities taking place in real hydraulic machines, adding the fact that the whole modelling code needs to be developed in-house and no commercial versions are available in the market.

Regarding the disadvantages of the one-way simulation, firstly, the impact loads that are inversely derived from the pitting tests tend to be underestimated because only a part of the energy is absorbed by the material. And the erosion is characterized by a much higher strain rate while the simulated pit shape is obtained under quasi-steady loading conditions. Secondly, the material properties are difficult to be determined. When material is subjected to repeated impact loads with different amplitudes and different durations, the material behavior is unpredictable because it involves elastic-plastic deformation, the inertial effect and the kinematic hardening process. Thirdly, modelling the material behavior requires a fine mesh at least in the loading area but, according to the references [15, 69], the characteristic mean size of the impacts is close of $50 \mu m$, which means that mesh size should be less than the $1 \mu m$ at least. Therefore, the computational cost for the 3D simulation is huge in the case of the simulation of hydrofoil cavitation and even more high for a hydraulic machine.

1.2.2.2 Computational Cavitating Fluid Dynamics

Due to the limitations of the FSI method and the demand to predict the most likely eroded area in hydraulic machinery and systems, this second method does not consider the solid response in the computation. The CCFD only simulates the cavitation flow by different modelling strategies and then estimates the erosive intensity in the whole computation domain using different postprocessing methodologies. The CCFD approach can be subdivided into three categories.

The first category consists of using the Eulerian-Lagrangian method to model the cavitating flow, in which the macroscopic flow field is treated using Eulerian mechanics and the individual microscopic bubbles are treated using Lagrangian mechanics. Ochiai et al. [75] obtained the macroscopic flow field by solving continuity, momentum, and energy equations of a compressible

two-phase medium. For the microscopic bubbles simulation, they considered that the bubbles follow the equation of bubble motion driven by the pressure gradient, the drag and the virtual mass force, and that the equation of bubble oscillation could be used to evaluate the evolution of bubble radius. The cavitation erosion characteristics is then predicted by the impact pressure on the wall surface owing to the propagating pressure wave induced by the bubble collapse. Similarly, Wang and Zhu [76] applied the LES to obtain the unsteady ambient pressure and the velocity profiles around the bubbles, and employed the Rayleigh–Plesset equation to determine the bubble radius. The cavitation erosion was predicted with the evolution of several representative bubbles in the averaged unsteady cavitation flow. Although this method has the best theoretical background as it includes the collapse rebound, a major problem lies in the choice of bubbles' injection points that play a major role in the predicted erosion intensity, regardless of the fact that the macroscopic flow is identical and uninfluenced of the bubble dynamics [44]. In addition, as we described above, this method is expensive and challenging for its computation application.

The second category consists of using a compressible solver to predict the erosion intensity of the cavitating flow. This method, which was developed by Schmidt et al. [77, 78], treats the two phase flow as homogeneous, compressible and inviscid, and resolves the collapse-induced pressure waves to determine the spectrum of collapse events in the fluid domain. Blume and Skoda [79] has used this method to assess the erosive flow around a circular leading edge hydrofoil and the found a good agreement with the experiment. However, they indicated that this approach requires a very fine computational mesh in order to capture all the cavitation scales of events and a very small time step is needed because it requires capturing shock waves near an object surface which have the same speed of propagation as the high sound speed in the water. Consequently, the practical implementation of this method is very limited, as a simulation of full scale realistic objects, for instance such as a marine propeller, would take too much time.

The last approach, which is the most widely applied one, only resolves the macroscopic cavitating flow field and obtains the cavitation aggressiveness by using different functions based on different flow properties. The principal difference between this approach and the second approach is that there are no critical requirements to cell size and time step, so the calculation time becomes more reasonable. As a result, this approach has been widely used and developed by different researchers because it has the potential to be promoted to predict the erosion aggressiveness and erosion distribution in hydraulic machines and systems. Some erosion models found in the literature are the following ones. Fortes-Patella et al., [80, 81] suggested an energy balance approach where the potential energy of the macroscopic cavitation structures was regarded as the main factor that generates erosion. Thus, the potential energy of a cavitation cloud is supposed to be converted into acoustic energy in the form of pressure waves. These pressure waves travel through the fluid and are able to damage the solid wall. Nohmi et al., [82] developed four erosion indices which were

based on pressure and volume fraction time derivatives as well as on absolute pressure differences. Li et al., [83] stated a numerical erosion model where the rapid increase of the local static pressure needed to exceed a certain threshold level for erosion to occur. Koukouviniis et al., [84] defined a Cavitation Aggressiveness Index based on the total derivative of pressure on the surface with values from zero that indicates the level of the hydrodynamic cavitation aggressiveness. Lloyd's Register Technical Investigation Department [85] applied DES to simulate the cavitating flow and obtained good predictions of the eroded regions based on its own functions, but few details about them can be found in the open literature. Unlike the above mentioned erosion models in which the pressure wave is considered to be responsible for the cavitation erosion, some researchers assumed that the high-speed microjet was the main mechanism provoking the cavitation erosion. Dular et al. [86] proposed an erosion model where the velocity of the microjet needed to exceed a certain threshold to be erosive for a given material. Following this work, Peters et al. [87] calculated the erosion potential of a cavitating flow based the accumulation of the dimensionless intensity coefficient, defined by the ratio of the jet velocity to a threshold velocity value, on every element face along the total calculation time. The advantage of these approaches is that there are no critical requirements regarding the cell size and the time step and consequently the calculation time becomes more reasonable than for instance the methods included in the third approach. Nevertheless, they need to be further validated with experiments because they involve the use of some empirical coefficients.

1.2.3 Critical review of the modelling strategies

In the previous two sections, the approaches for modelling unsteady cavitation and cavitation erosion have been summarized. It is obvious that there is no perfect model that can be used in all fields, and that each model has their own advantages and disadvantages. However, considering that our main field of interest is to model the unsteady cavity behavior and its associated erosion power in hydraulic machinery, it is necessary to find out and tailor the most suitable models and set-ups.

For modelling turbulence, as indicated in Table 1.1, there is no doubt that DNS and LES have the capability to provide the most realistic flow information. However, the huge computational cost and the high requirements for the numerical scheme prevent their application, especially for modelling flow in hydraulic machines which size might reach the order of meters and high Re flows are dominated by the relatively thin boundary layers. For example, an estimate of the computer requirements for the simulation of a single turbine blade with end-walls indicated that the LES models requires computer resources ten thousand times higher than the URANS models [27]. In addition, the Hybrid SRS model has the potential to provide better flow information with relatively low computation cost, but there is still a high demand for the spatial and temporal resolution which is also much higher than for the URANS models. For example, the mesh scale needs to be smaller than the characteristic length scale in the region far away the boundary layer, and the time step needs

to be small enough to meet the requirement that the Courant number is less than one, which is almost impossible for modelling flow in high rotating speed machinery. In addition to that, when the simulation of the entire machine is required for the design of turbomachinery (or at least a significant number of its components), this also increases the size of the meshes and the calculation requirements. As a conclusion, nowadays the use of SRS models to simulate industrial problems appears to be unrealistic and therefore, the URANS models are a more suitable and economical approach which make them more dominant for engineering applications. Besides, the EVM model is more popular than RSM model according to the survey of ASME [88] due to the fact that RSM model is hard to converge when solving the six additional equations. Moreover, the proposal of Reboud's correction [89], which reduces the turbulent viscosity in the mixture of water and vapor by taking into account the compressibility effects, makes the URANS models capable of capturing the unsteady cavity behaviors, leading to that the EVM models can provide agreeable numerical results with the experiment data. However, with the development of CFD there are different forms of EVM available, but conclusive results are missing regarding the influence of different EVM models on the cavitation simulation.

Regarding the cavitation models, the Euler-Lagrange approach has the best theoretical background because it can not only predict the macro-scale cavity behavior, but it also provides the information relative to the growth and collapse of single bubble and the bubble-bubble interactions. Thus, this method is very challenging and it is still at a stage of developing its numerical algorithms. Therefore, the use of this approach is impractical especially in the context of engineering applications. Regarding the Euler-Euler approach for the multi-fluid approach, it has the ability to consider the non-equilibrium effects between phases, but it is still a real challenge for numerical simulation due to the complicated characteristics of the equation system and the troublesome due to the non-conservative terms. In conclusion, it remains mainly suited only for inviscid and simple geometries. In contrast, the single-fluid method (homogeneous method) has received more attention up to now and it has been developed maturely because of its lower computational cost and easier numerical calculation, but not all models belonging to this method are widely used. For example, the Single-Phase Interface Tracking Model is not able to predict the unsteady cavity behavior, and the EOS model do not consider the mass transfer between two phases and cannot capture the baroclinic vorticity production term. Comparatively speaking, the Transport Equation model is very attractive because it can not only predict the mass transfer when cavitation occurs, but also it is easier to couple with the turbulence models. Therefore, the TEM has been the most widely used model up to now and it will also be employed for our thesis work. However, almost all the TEMs have the problem that they need to introduce empirical constants to regulate the mass transfer rate. Thus, these constants are need to be tuned according to the case being simulated. In addition, different cavitation models require different source terms, which makes that the cavitation models perform differently.

As a result, in our work, the influence of the empirical constants and the effectiveness of several cavitation models will be evaluated in detail.

Regarding the erosion models, the FSI is a good approach to conduct theoretical investigations because it takes into account the material response, and even considers the effect of material on the bubble collapse if two way FSI is conducted. But in practice the actual erosion mechanism of unsteady large scale cavitation forms is much more complicated than the loading from single bubbles or the effects of repetitive loads with a constant amplitude. Therefore, this method can only provide some preliminary results and it cannot be easily generalized to respond to industrial applications due to its huge computational cost and its complexity. In addition, when using the CCFD method to investigate the cavitation erosion, the application of the Euler-Lagrange and the compressible methods are also quite limited. Firstly, the numerical application of the Euler-Lagrange is very difficult even just for modelling cavitation. Secondly, these two methods have a huge computation cost because the Euler-Lagrange requires the mesh scale to be less than the scale of the minimum bubble and the compressible method requires a very small time step to capture the shock waves when the bubbles collapse. This makes these two methods impractical in the engineering and industrial contexts. Hence, in our work, we have mainly an approach which implements the erosion model by means of a post processing procedure on the obtained set of results. However, all the erosion models proposed by different researchers have their weak points. For example, the model proposed by Nohmi et al. [82] does not provide a physical background for the formula proposed and it also lacks the definition of some additional exponents depending on the characteristics of a particular solid material. Li's [83] and Koukouvinis's [84] models are not directly related to the vapor volume fraction and the potential energy in vapor structures. Dular's [86] and Peters's [87] models consider the hammer pressure caused by the microjet to be the main responsible for the material damage, however, it is an issue how to determine the pressure driving the bubble collapse and the resulting jet. Furthermore, these two models are not easy to implement in commercial CFD codes. Comparatively speaking, the model proposed by Fortes-Patella et al. [80, 81] is proved to be better than other models [90] and has been widely used because it has been validated by various researchers and it provides a good agreement with the experiments [90–93]. In spite of that, the reliability of this model depends directly on the determination of two energy transfer ratios, and some uncertainties still need to be investigated and discussed to improve its performance and applicability. In summary, we have selected the Fortes-Patella's model to predict and study the erosive cavitation induced by cloud cavitation because our main interest has been to develop and validate an erosion model that can be used for an engineering and industrial applications

1.3 Objectives

General objective:

The cloud cavitation is one of the most aggressive cavitation forms which induces vibrations and noise, and provokes the damage of the material surfaces. Hence, it is necessary to predict the unsteady cloudy cavitation and its associated erosion aggressiveness. In this thesis, we aim to evaluate and improve the performance of existing numerical approaches for modelling cavitation so that they can reproduce the unsteady cavity behavior with more accuracy. Moreover, we try to apply and validate an erosion model to predict from the simulated cavitation structures its erosion aggressiveness.

Specific objectives:

1. Study the sensitivity of the numerical parameters and find the most adequate set-up configurations that permit to guarantee numerical accuracy while economizing the computational costs.
2. Find out the most adequate eddy-viscosity models and the required numerical settings for the simulation of unsteady cavitation around a hydrofoil by comparing their performance.
3. Improve the accuracy of the cavitation models by considering the second order term in the Rayleigh–Plesset equation and validating the improved model by simulating different cavitation patterns.
4. Investigate the influence of the empirical coefficients of the cavitation model selected on the cavitation behavior, and finding out their optimal range of values.
5. Implement an erosion model to investigate the relation between cavitation structures and their erosion power.
6. Investigate the factors influencing the erosion intensity and erosion distribution, including the definition of driving pressure and the cavitation model selected.
7. Analyze the main mechanisms of cavitation erosion under unsteady cavitation condition by comparing the numerical results with the experimental observations.
8. Evaluate the influence of the free stream velocity on erosion intensity and build a function of erosion power and inflow velocity.

1.4 Methodology

The methodology for present thesis is devised as follows:

The first steps are intended to select the best numerical models according to the available experimental data. For that, the influence of the numerical settings on the numerical results will be validated and the appropriate numerical configurations to balance the numerical accuracy and the

computation cost will be determined (including 2D or 3D simulations, boundary conditions definition, grid resolution and typology, time step, number of iterations and y^+).

Secondly, different eddy-viscosity models to conduct unsteady cavitation simulation will be applied, and the influence that they have on the numerical results based on the existing experimental data will be assessed. The model that can best reproduce the cavity dynamic behavior will be found out.

Then, the performance of the cavitation models will be improved by investigating the influence of empirical coefficients on the unsteady cavity evolution and by tuning the empirical coefficients using an optimizing method. In addition, the cavitation models will be corrected by considering the effect of the second-order term in the Rayleigh–Plesset equation, and the cavitation simulation results predicted by original and corrected cavitation models will be compared and validated.

Finally, the cavitation erosion will be investigated by implementing an erosion model with a post processing procedure, analyzing the influence of the driving pressure and the selected cavitation models on the erosion intensity distributions. As a result, the better choice for the accurate prediction of erosion will be determined. In addition, the influence of inflow velocities on the erosion power will be evaluated and the corresponding laws will be found out.

1.5 Organization of this thesis

This thesis is organized in the following chapters:

This first chapter introduces the general background of cavitation and cavitation erosion, the state of art regarding to the modelling of turbulent cavitating flows and cavitation erosion, the objectives of the thesis and the methodology used.

In Chapter 2, the numerical method used for the present thesis, including the turbulence model, the cavitation model, and the erosion model are illustrated in detail.

In Chapter 3, the numerical method, including the setting of numerical parameters, and the selection of the turbulence models are assessed by comparison with the experiment results. Furthermore, the influence of the empirical coefficients on the cavity behavior is investigated and an optimization method is used to find out the better coefficient range for reproducing the unsteady cavity behavior.

In Chapter 4, the performance of two cavitation models (Zwart and Singhal) are improved by considering the second order term in the Rayleigh–Plesset equation. Then, the improved model is assessed by modelling different cavitation patterns including the steady attached cavity and unsteady cloudy cavity.

In Chapter 5, the erosion mechanism of unsteady cavity is investigated by applying the erosion models. The factors influencing the erosion intensity and the energy transfer ratio are studied in detail. And finally, the relationship between flow velocity and erosive power is calculated.

In Chapter 6, the conclusions and a prospect of future research are finally summarized.

Chapter 2 Numerical Approach

In this chapter, the numerical approaches are described. Firstly, the mathematical derivations of the turbulence models are given, secondly, the cavitation modelling methods are presented. Then, an erosion model is introduced and described.

2.1 Turbulence modelling

Considering that our main field of interest is to achieve the modelling of cavitation erosion in hydraulic machinery and that DNS and SRS methods have a high computational cost, URANS models are considered to be more suitable for the present investigation. The following sections will provide the detailed mathematical derivations of some widely used URANS models which will be evaluated in the next chapter.

The Navier-Stokes equations are:

$$\frac{\partial \rho}{\partial t} + \frac{\partial}{\partial x_i} (\rho u_i) = 0 \quad (2-1)$$

$$\frac{\partial}{\partial t} (\rho u_i) + \frac{\partial}{\partial x_j} (\rho u_i u_j) = -\frac{\partial p}{\partial x_i} + \frac{\partial}{\partial x_j} \left[\mu \left(\frac{\partial u_i}{\partial x_j} + \frac{\partial u_j}{\partial x_i} - \frac{2}{3} \delta_{ij} \frac{\partial u_k}{\partial x_k} \right) \right] \quad (2-2)$$

where u and p are the flow velocity and pressure, t and ρ is the time and density, μ is the dynamic viscosity.

In Reynolds decomposition, every instantaneous quantity φ is decomposed into its time-averaged part and its fluctuating part, which means:

$$\varphi = \bar{\varphi} + \varphi' \quad (2-3)$$

where the time average of a variable is defined by:

$$\bar{\varphi} = \frac{1}{\Delta t} \int_t^{t+\Delta t} \varphi(t) dt \quad (2-4)$$

Then, the resulting RANS equations are:

$$\frac{\partial \rho}{\partial t} + \frac{\partial}{\partial x_i} (\rho \bar{u}_i) = 0 \quad (2-5)$$

$$\frac{\partial}{\partial t} (\rho \bar{u}_i) + \frac{\partial}{\partial x_j} (\rho \bar{u}_i \bar{u}_j) = -\frac{\partial \bar{p}}{\partial x_i} + \frac{\partial}{\partial x_j} \left[\mu \left(\frac{\partial \bar{u}_i}{\partial x_j} + \frac{\partial \bar{u}_j}{\partial x_i} - \frac{2}{3} \delta_{ij} \frac{\partial \bar{u}_k}{\partial x_k} \right) \right] + \frac{\partial}{\partial x_j} \left(-\rho \overline{u_i' u_j'} \right) \quad (2-6)$$

Equations (2-5) and (2-6) have the same general form as the instantaneous Navier-Stokes equations, with the velocities and other solution variables now representing time-averaged values, and new additional terms, $-\overline{\rho u_i' u_j'}$, that represent the effects of turbulence, which are known as Reynolds stress terms.

Therefore, for a general statistically three-dimensional flow, four independent equations govern the mean velocity field; namely three components of the Reynolds equations (Equation (2-6)) and one mean continuity equation (Equation. (2-5)). However, these four equations contain more than four unknown quantities. In addition to \bar{u}_i and \bar{p} , the Reynolds stress is still unknown. In order to close this system of equations, there are two approaches: the first one is based on eddy-viscosity hypothesis which relates the Reynolds stresses to the mean flow, known as eddy-viscosity model; the second is based on solving the transport equation for all components of the Reynolds stress tensor, known as Reynolds stress model. Hereafter, we mainly discuss the derivation and application of some popular eddy-viscosity models because the term RANS in hybrid RANS-LES typically represents the eddy-viscosity model and has nothing to do with Reynold stress model. Also, Reynolds stress model is not widely used in our interested field, for its derivation and explanation please refer to reference [20].

Eddy-viscosity models were developed on the basis of the Boussinesq hypothesis in 1877 [94], who proposed that the Reynolds stress is proportional to the mean rate of strain, which refers to:

$$-\overline{\rho u_i' u_j'} = \mu_t \left(\frac{\partial \bar{u}_i}{\partial x_j} + \frac{\partial \bar{u}_j}{\partial x_i} \right) - \frac{2}{3} \delta_{ij} \left(\rho k + \mu_t \frac{\partial \bar{u}_k}{\partial x_k} \right) \quad (2-7)$$

where μ_t is the so-called turbulent viscosity; $k = \overline{u_i' u_i'} / 2$ denotes the turbulent kinetic energy.

So with Equation 2-7, the Reynolds equation can be rewritten as;

$$\frac{\partial}{\partial t} (\rho \bar{u}_i) + \frac{\partial}{\partial x_j} (\rho \overline{u_i u_j}) = - \frac{\partial}{\partial x_i} \left(\bar{p} + \frac{2}{3} \rho k + \frac{2}{3} (\mu + \mu_t) \frac{\partial \bar{u}_k}{\partial x_k} \right) + \frac{\partial}{\partial x_j} \left[(\mu + \mu_t) \left(\frac{\partial \bar{u}_i}{\partial x_j} + \frac{\partial \bar{u}_j}{\partial x_i} \right) \right] \quad (2-8)$$

This is the final version of the Reynolds equation based on the turbulent-viscosity hypothesis. Consequently, there is only one unknown variable, μ_t , to be resolved. If μ_t can be specified, then the mean flow equations can be solved.

Hereafter, we introduce some widely applied specification of μ_t , i.e., eddy-turbulent model.

2.1.1 Standard k - ε model

The standard k - ε model is one of the most widely used models for industrial applications and it has been implemented in many different CFD codes because it offers a good accuracy and robustness. This model was proposed by Launder and Spalding [95] in 1972, in which the eddy viscosity was related to the turbulence kinetic energy k and turbulence dissipation rate ε (which is the rate that turbulent kinetic energy is converted into the thermal energy by the action of the viscosity, and is

defined by $\varepsilon = \nu \overline{\frac{\partial u_i}{\partial x_j} \frac{\partial u_i}{\partial x_j}}$ via the equation below:

$$\mu_t = \rho C_\mu \frac{k^2}{\varepsilon} \quad (2-9)$$

The values k and ε of can be directly obtained by solving their respective transport equations:

$$\frac{\partial}{\partial t}(\rho k) + \frac{\partial}{\partial x_i}(\rho k u_i) = \frac{\partial}{\partial x_j} \left[\left(\mu + \frac{\mu_t}{\sigma_k} \right) \frac{\partial k}{\partial x_j} \right] + P_k - \rho \varepsilon \quad (2-10)$$

$$\frac{\partial}{\partial t}(\rho \varepsilon) + \frac{\partial}{\partial x_i}(\rho \varepsilon u_i) = \frac{\partial}{\partial x_j} \left[\left(\mu + \frac{\mu_t}{\sigma_\varepsilon} \right) \frac{\partial \varepsilon}{\partial x_j} \right] + \frac{\varepsilon}{k} (C_{1\varepsilon} P_k - C_{2\varepsilon} \rho \varepsilon) \quad (2-11)$$

where $C_{1\varepsilon}$, $C_{2\varepsilon}$, σ_k , σ_ε , C_μ are model constants and they have the following default values: $C_{1\varepsilon}=1.44$, $C_{2\varepsilon}=1.92$, $\sigma_k=1.0$, $\sigma_\varepsilon=1.3$, $C_\mu=0.09$. Sometimes, the value of these constants can be changed for a particular flow. For example, when modelling the turbulence close to a wall, some damping function are added, also known as low k - ε model which damp the constants $C_{1\varepsilon}$, $C_{2\varepsilon}$, C_μ by times a function f_1 , f_2 and f_μ respectively. With these functions, the dissipation of ε near the wall is reduced and so more dissipation of k is expected, which in turn avoids that the eddies scale in the sub-viscos layer is too large and also the turbulent viscosity is over predicted.

Additionally, in these equations, P_k represents the generation of turbulence kinetic energy due to the viscous force, which is modeled using [96]:

$$P_k = \mu_t \left(\frac{\partial \bar{u}_i}{\partial x_j} + \frac{\partial \bar{u}_j}{\partial x_i} \right) \frac{\partial \bar{u}_i}{\partial x_j} - \frac{2}{3} \frac{\partial \bar{u}_k}{\partial x_k} \left(\rho k + 3\mu_t \frac{\partial \bar{u}_k}{\partial x_k} \right) \quad (2-12)$$

Based on Equations 2-9, 2-10 and 2-11, the eddy viscosity μ_t is obtained and then Equation 2-8 is closed. Generally, the standard k - ε model is mainly used for fully turbulent flows because the assumption in its derivation is that the flow is fully turbulent and that the eddies in all turbulence scales are isotropic whereby the normal stresses are equal, i.e. $\overline{u_1 u_1} = \overline{u_2 u_2} = \overline{u_3 u_3}$. Therefore, there are some particular flows not suitable for using this model, like rotating flows, boundary layer

separations and flows with sudden change in the mean strain rate for instance.

2.1.2 RNG k - ε model

RNG k - ε model [97] was derived using renormalization group (RNG) analysis of the Navier-Stokes equations. It has a similar form to the standard k - ε model. For example, the eddy viscosity is also calculated via Equation 2-9, and the transport equations for the turbulence kinetic energy and the turbulence dissipation rate are the same as those for the standard k - ε model. The major difference lies in the variation of the model constants e.g., the constant equals 0.0845 in the RNG model, and the constant in the transport equation of dissipation is replaced by a new constant, and the Equation 2-9 becomes:

$$\frac{\partial}{\partial t}(\rho\varepsilon) + \frac{\partial}{\partial x_i}(\rho\varepsilon u_i) = \frac{\partial}{\partial x_j} \left[\left(\mu + \frac{\mu_t}{\sigma_{\varepsilon RNG}} \right) \frac{\partial \varepsilon}{\partial x_j} \right] + \frac{\varepsilon}{k} (C_{1\varepsilon RNG} P_k - C_{2\varepsilon RNG} \rho\varepsilon) \quad (2-13)$$

where $C_{1\varepsilon RNG}$, $C_{2\varepsilon RNG}$, σ_{kRNG} , σ_{ε} are model constants and they have the following default values:

$$C_{1\varepsilon RNG} = 1.42 - f_\eta, \quad C_{2\varepsilon RNG} = 1.68, \quad \sigma_{kRNG} = 1.0, \quad \sigma_{\varepsilon RNG} = 0.7179$$

$$\text{And } f_\eta = \frac{\eta(1-\eta/4.38)}{(1+\beta_{RNG}\eta^3)}; \quad \eta = \sqrt{\frac{P_k}{\rho C_{\mu RNG} \varepsilon}}$$

2.1.3 The Wilcox k - ω Model

Wilcox [98] proposed a new approach to calculate the turbulent viscosity, which relates μ_t to turbulence kinetic energy, k , and the specific dissipation rate, ω , via the relation:

$$\mu_t = \rho k / \omega \quad (2-14)$$

And the values of the k and ω are obtained from the following differential transport equations:

$$\frac{\partial(\rho k)}{\partial t} + \frac{\partial(\rho u_j k)}{\partial x_j} = \frac{\partial}{\partial x_j} \left(\left(\mu + \frac{\mu_t}{\sigma_{k1}} \right) \frac{\partial k}{\partial x_j} \right) + P_k - \beta' \rho k \omega \quad (2-15)$$

$$\frac{\partial}{\partial t}(\rho\omega) + \frac{\partial}{\partial x_j}(\rho\omega u_j) = \frac{\partial}{\partial x_j} \left(\left(\mu + \frac{\mu_t}{\sigma_{\omega 1}} \right) \frac{\partial \omega}{\partial x_j} \right) + \alpha_1 \frac{\omega}{k} P_k - \beta_1 \rho \omega^2 \quad (2-16)$$

where P_k represents the generation of turbulence kinetic energy and is calculated as in the standard k - ε model, and the model constants are given by: $\beta' = 0.09$, $\alpha_1 = 5/9$, $\sigma_{k1} = 2$, $\sigma_{\omega 1} = 2$, $\beta_1 = 0.075$.

The advantage of this model is that it considers the effect of the Low-Reynolds number in the near wall region. However, one of its disadvantages is the sensitivity to the freestream conditions, i.e., the value of ω specified in inlet boundary will significantly affect the solution. In order to solve this

undesirable problem, considering the respective merits of standard $k-\varepsilon$ model (e.g. insensitive to the freestream condition) and of the $k-\omega$ model (e.g. the robust and accurate prediction in the near-wall region), Menter [99] proposed a new formulation of $k-\omega$ model, which incorporates the advantages of the standard $k-\varepsilon$ and $k-\omega$ model.

2.1.4 SST $k-\omega$ Model

Because the specific dissipation rate, ω , can also be thought as the ratio of ε to k , ($\varepsilon=0.09k\omega$) the transport equation for standard $k-\varepsilon$ model (Equations 2-10 and 2-11) can also be rewritten as a transformed $k-\varepsilon$ model:

$$\frac{\partial(\rho k)}{\partial t} + \frac{\partial(\rho u_j k)}{\partial x_j} = \frac{\partial}{\partial x_j} \left(\left(\mu + \frac{\mu_t}{\sigma_{k2}} \right) \frac{\partial k}{\partial x_j} \right) + P_k - \beta' \rho k \omega \quad (2-17)$$

$$\frac{\partial}{\partial t}(\rho \omega) + \frac{\partial}{\partial x_j}(\rho \omega u_j) = \frac{\partial}{\partial x_j} \left(\left(\mu + \frac{\mu_t}{\sigma_{\omega 2}} \right) \frac{\partial \omega}{\partial x_j} \right) + \alpha_2 \frac{\omega}{k} P_k - \beta_2 \rho \omega^2 + 2\rho \frac{1}{\sigma_{\omega 2} \omega} \frac{\partial k}{\partial x_j} \frac{\partial \omega}{\partial x_j} \quad (2-18)$$

where the model constants are: $\alpha_2 = 0.44$, $\sigma_{k2} = 1$, $\sigma_{\omega 2} = 1/0.856$, $\beta_2 = 0.0828$.

Now if the transformed $k-\varepsilon$ model is compared with the standard $k-\omega$ model (Equations 2-15 and 2-16), it can be observed that all the terms are the same with an exception that the model constants differ and that an additional term appears on the right hand side of Equation 18. With this small difference, a transformation of the $k-\varepsilon$ model to a $k-\omega$ formulation can be achieved by introducing a blending function F_1 . Now the equations of the $k-\omega$ model are multiplied by function F_1 , the transformed $k-\varepsilon$ equations by a function $(1-F_1)$ and the corresponding k and ω equations are added, which gives:

$$\frac{\partial(\rho k)}{\partial t} + \frac{\partial(\rho u_j k)}{\partial x_j} = \frac{\partial}{\partial x_j} \left(\left(\mu + \frac{\mu_t}{\sigma_{k3}} \right) \frac{\partial k}{\partial x_j} \right) + P_k - \beta' \rho k \omega \quad (2-19)$$

$$\frac{\partial}{\partial t}(\rho \omega) + \frac{\partial}{\partial x_j}(\rho \omega u_j) = \frac{\partial}{\partial x_j} \left(\left(\mu + \frac{\mu_t}{\sigma_{\omega 3}} \right) \frac{\partial \omega}{\partial x_j} \right) + \alpha_3 \frac{\omega}{k} P_k - \beta_3 \rho \omega^2 + 2(1-F_1) \rho \frac{1}{\sigma_{\omega 3} \omega} \frac{\partial k}{\partial x_j} \frac{\partial \omega}{\partial x_j} \quad (2-20)$$

where the model coefficients σ_{k3} , $\sigma_{\omega 3}$, α_3 and β_3 are linear combinations of the corresponding coefficients of the $k-\omega$ and the modified $k-\varepsilon$ turbulence models via: $\Phi_3 = F_1 \Phi_1 + (1-F_1) \Phi_2$.

The blending function defined by Equation 2-21 depends on the wall distance and it is equal to 1 near the surface and decreases to 0 outside the boundary layer:

$$F_1 = \tanh \left(\arg_1^4 \right) \quad (2-21)$$

with:

$$\arg_1 = \min \left[\max \left(\frac{\sqrt{k}}{0.09\omega y}, \frac{500\mu}{\rho y^2 \omega} \right), \frac{4\rho k}{CD_{kw} \sigma_{\omega 2} y^2} \right] \quad (2-22)$$

where y is the distance to the nearest wall, and:

$$CD_{kw} = \max \left(2\rho \frac{1}{\sigma_{\omega 2}} \frac{1}{\omega} \frac{\partial k}{\partial x_j} \frac{\partial \omega}{\partial x_j}, 10^{-10} \right) \quad (2-23)$$

Hence, this model (Equations 2-19 and 2-20) combines the advantages of the k - ω and the k - ε model, but it still fails to properly predict the onset and amount of flow separation from smooth surfaces. This is because it does not account for the transport of the turbulent shear stress, and over predicts the eddy-viscosity. Consequently, a limiter to the eddy-viscosity was introduced to capture the proper transport behavior. Then the eddy-viscosity based on SST model is calculated by:

$$\mu_t = \frac{\rho k}{\omega} \frac{1}{\max \left(1, \frac{SF_2}{a_1 \omega} \right)} \quad (2-24)$$

where $a_1 = 0.31$, F_2 is a blending function which restricts the limiter to the wall boundary layer, S is an invariant measure of the strain rate,

$$F_2 = \tanh(\arg_2^2) \quad (2-25)$$

with:

$$\arg_2 = \max \left(2 \frac{\sqrt{k}}{0.09\omega y}, \frac{500\mu}{\rho y^2 \omega} \right) \quad (2-26)$$

2.2 Cavitation modelling

In our simulation, homogeneous mixture models will be used in which the two phases are assumed to be in thermal and mechanical equilibrium: they share the same temperature T and the same pressure p , and thus these two phases are considered to be a single mixture with mixed properties. For that, the averaged Navier-Stokes equations for the mixture are solved. Note that in the present work, the thermal effects have been neglected due to the fact that the high specific heat capacity of water only leads to small temperature changes and that the variations of the vapor saturation pressure can be considered negligible. Therefore, the energy equation is not solved.

The governing equations of the mixture are the continuity and momentum equations expressed as follows:

$$\frac{\partial \rho_m}{\partial t} + \frac{\partial}{\partial x_i} (\rho_m u_i) = 0 \quad (2-27)$$

$$\frac{\partial}{\partial t} (\rho_m u_i) + \frac{\partial}{\partial x_j} (\rho_m u_i u_j) = -\frac{\partial p}{\partial x_i} + \frac{\partial}{\partial x_j} \left[(\mu_m + \mu_t) \left(\frac{\partial u_i}{\partial x_j} + \frac{\partial u_j}{\partial x_i} - \frac{2}{3} \delta_{ij} \frac{\partial u_k}{\partial x_k} \right) \right] \quad (2-28)$$

where ρ_m and μ_m are the mixture density and viscosity, which are defined as the summation of the separate equations of the phase quantities:

$$\rho_m = \alpha \rho_v + (1 - \alpha) \rho_l \quad (2-29)$$

$$\mu_m = \alpha \mu_v + (1 - \alpha) \mu_l \quad (2-30)$$

where the subscripts m , l and v denote the mixture, liquid and vapor respectively, and α is the vapor volume fraction defined by:

$$\alpha = \frac{V_v}{V_v + V_l} \quad (2-31)$$

And the vapor volume fraction can be obtained by an additional transport equation, the so-called transport equation model (TEM) in the first chapter:

$$\frac{\partial(\alpha \rho_v)}{\partial t} + \frac{\partial}{\partial x_i} (\alpha \rho_v u_i) = \dot{m} \quad (2-32)$$

where the term \dot{m} accounts for the mass transfer rate between the water and vapor phases, which is defined by each cavitation model. Table 2.1 lists the mathematical equations describing each of these cavitation models where R_B in the Zwart model is the vapor bubble radius with a constant value of 10^{-6} m. Meanwhile, in the Sauer model, it is a variable value that is function of the local vapor volume fraction. α_{nuc} is the nucleation site volume fraction with a default value of 0.0005. Then, $t_\infty = C/U_{inf}$ is the mean time scale and C_{prod} and C_{dest} are the empirical coefficients for vaporization and condensation, respectively, which were taken as 50 and 0.01 for the Zwart model, 0.01 and 0.01 for Singhal model, and 100 and 100 for the Kunz model.

Table 2.1 Mathematical expressions of the cavitation models.

Model	$\dot{m} (P < P_v)$	$\dot{m} (P > P_v)$
Zwart [65]	$C_{prod} \frac{3\alpha_{nuc}(1-\alpha_v)\rho_v}{R_B} \sqrt{\frac{2(p_v - p)}{3\rho_l}}$	$-C_{dest} \frac{3\alpha_v\rho_v}{R_B} \sqrt{\frac{2(p - p_v)}{3\rho_l}}$
Singhal [67]	$C_{prod} \frac{\max(1.0, \sqrt{k})}{S} \rho_l \rho_v \sqrt{\frac{2(p_v - p)}{3\rho_l}} (1 - \frac{\alpha\rho_v}{\rho_m})$	$-C_{dest} \frac{\max(1.0, \sqrt{k})}{S} \rho_l \rho_l \sqrt{\frac{2(p - p_v)}{3\rho_l}} \frac{\alpha\rho_v}{\rho_m}$
Sauer [68]	$\frac{\rho_v\rho_l}{\rho} \alpha_v(1-\alpha_v) \frac{3}{R_B} \sqrt{\frac{2(p_v - p)}{3\rho_l}}$	$-\frac{\rho_v\rho_l}{\rho} \alpha_v(1-\alpha_v) \frac{3}{R_B} \sqrt{\frac{2(p - p_v)}{3\rho_l}}$
Kunz [66]	$\frac{C_{dest}\rho_v\alpha_v(1-\alpha_v)^2}{t_\infty} + \frac{C_{prod}\rho_v(1-\alpha_v)\min[0, p - p_v]}{(0.5\rho_l U_{inf}^2)t_\infty}$	$-\frac{C_{dest}\rho_v\alpha_v(1-\alpha_v)^2}{t_\infty}$

In the next chapter, the performance of these models on predicting different cavitation patterns or on erosion will be evaluated.

2.3 Erosion modelling

In our present work, the erosion model proposed by Fortes Patella et al. [80, 81] has been used to investigate the erosion character of unsteady cavitation. In this model, the pressure wave generated by the bubble collapse is considered as the main mechanism of erosion and this erosion model is based on the concept of the energy cascade. As shown in Figure 2.1, a pressure wave is emitted during the collapse of the vapor structure and then it reaches the solid wall and interacts with the material, leading to the damage generation. And during this process, two efficiencies involved in the energy conversion are introduced which need to be assessed.

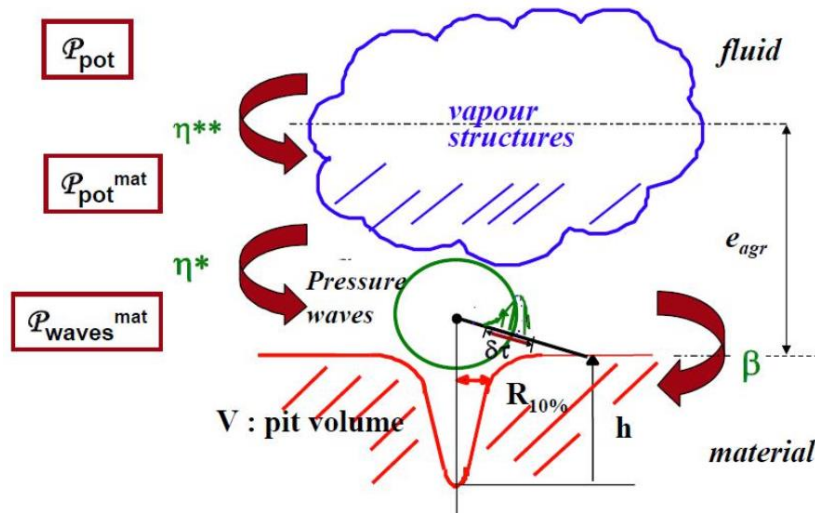


Figure 2.1. Physical cavitation erosion scenario based on the energy balance approach. Reproduced from [80].

In this cavitation erosion scenario, the potential energy and power of the cavitating flow is evaluated. The initial potential energy of vapor structures can be calculated with:

$$E_{pot} = \Delta p V_v = (p_d - p_v) V_v \quad (2-33)$$

where V_v is the volume of the vapor structure and p_d is the driving pressure which forces its collapse, and p_v is the saturation pressure. Then, an instantaneous potential power, P_{pot} , can be defined with Lagrangian time derivatives as expressed with:

$$P_{pot} = \frac{DE_{pot}}{Dt} = (p_d - p_v) \frac{DV_v}{Dt} + V_{vap} \frac{DP_d}{Dt} \approx (p_d - p_v) \frac{DV_v}{Dt} \quad (2-34)$$

where the pressure derivative has been neglected because it was found to be negligible compared to the vapor volume derivative [100].

Then, the flow aggressiveness potential power, P_{pot}^{mat} , is linked to the instantaneous potential power, P_{pot} and the energy transfer efficiency η^{**} via the relation:

$$P_{pot}^{mat} = \eta^{**} P_{pot} \quad (2-35)$$

where the energy transfer efficiency η^{**} is a function of the hydrodynamic characteristics of the main flow (e.g., the free stream velocity and the cavitation number) and the distance between the collapse center and the material surface. Therefore, the flow potential power is highly related to flow configuration like the cavitation flow behavior, the geometry of the hydrofoil, the angle of attack etc.

Next, the pressure wave power emitted when the vapor structure collapses, P_{waves}^{mat} , is defined by:

$$P_{waves}^{mat} = \eta^* P_{pot}^{mat} \quad (2-36)$$

where η^* is the efficiency which quantifies the effective energy transfer between the potential power of the vapor volume and the actually erosive power, and it depends mainly on the initial gas pressure and the surrounding pressure as well as the air content in the flow.

In the final stage, the estimated pressure wave hits the material surface and leads to a volume damage rate, V_d , that can be measured by a 3D laser profilometer and related to the pressure wave power by:

$$V_d = \frac{P_{waves}^{mat}}{\beta \Delta S} \quad (2-37)$$

where ΔS is the analyzed sample surface, and β is a mechanical transfer function depending strongly on the characteristics of the material.

Chapter 3 Assessment of URANS models and empirical coefficients

The numerical simulation of unsteady cavitation flows is of prime importance to assess the design and operation of hydraulic machinery due to their undesired effects such as noise and erosion. Since the predicted results are very sensitive to the selected models and the associated parameters, three Reynolds Average Navier-Stokes (RANS) turbulence models and the Zwart cavitation model have been selected to assess their performance for the simulation of cloud cavitation on 2D hydrofoils. The experimental cavitation tests from a NACA65012 hydrofoil at different hydrodynamic conditions have been used as a reference to tune the modelling parameters and the experimental tests from a NACA0015 have finally been used to validate them. The effects of near wall grid refinement, time step, iterations and mesh elements have also been investigated. The results indicate that the Shear Stress Transport (SST) model is sensitive to near wall grid resolution which should be fine enough. Moreover, the cavitation morphology and dynamic behavior at different hydrodynamic conditions are sensitive to the selection of the empirical vaporization, F_v , and condensation, F_c , coefficients required by the Zwart model. Therefore, a multiple linear regression approach with the single objective of predicting the shedding frequency has been carried out that permits to find out the range of coefficient values giving the most accurate results. In addition, it has been observed that they provide a better prediction of the vapor volume fraction and of the instantaneous pressure pulse generated by the main cloud cavity collapse.

The complete content of this chapter can be found in the paper entitled “Assessment of RANS turbulence models and Zwart cavitation model empirical coefficients for the simulation of unsteady cloud cavitation” and published in 2019 in the open access journal “Engineering Applications of Computational Fluid Mechanics” with an Impact Factor of 5.8 (first quartile 1) [101] which can be found in Annex A of this thesis report.

Chapter 4 Improvement of cavitation models

In this chapter, the Zwart and Singhal cavitation models were modified and improved by taking into account the second order term of the Rayleigh–Plesset (RP) equation. Firstly, the complete mathematical derivation of the corrected condensation mass transfer rate equation has been given and the significance of the second order term has been addressed. Secondly, the modified models have been validated with two experimental cases corresponding to a couple of steady cavitation flows around a hydrofoil and around a submerged cylindrical body with a hemi-spherical head, respectively. Lastly, the experimental unsteady cavitation test for a NACA0009 hydrofoil has been used as a reference to further validate the improvement of the current correction.

The content in this chapter reproduces the paper entitled “Improvement of cavitation mass transfer modeling by including Rayleigh–Plesset equation second order term” and published in 2020 in the non-open access journal “European Journal of Mechanics/B Fluids” with an impact Factor of 2.131 (second quartile Q2) [102] which can be found in the following link:

<https://www.sciencedirect.com/science/article/abs/pii/S0997754619304443>.

4.1 Cavitation model correction

In this section, the significance of the second order term of the RP equation is discussed and the detailed mathematical derivation from the RP equation to the definition of the source terms of the cavitation models are given. The well-known bubble dynamics RP equation is given as Equation (4-1) where, in most of the cases, three terms including the second order term, the viscous forces term and the surface tension term are all neglected because they are considered to be secondary. More specifically, the time derivative of the bubble radius is only thought to be related to the pressure change term. However, in our work we have decided to evaluate the effects of keeping the second order term. For that, the new corrected relationships between the time derivative of the bubble radius and the pressure change have been developed and this new formula is given as Equation (4-2). Based on Equation (4-2), the corrected bubble growth and collapse rates have been obtained as Equations (4-3) and (4-4), respectively. By comparing with the original bubble growth and collapse rates (see Equations (4-5) and (4-6)), it is found that the effect of the second order term is negligible for the bubble growth, but that the bubble collapse rate is underestimated.

Therefore, the new corrected condensation mass transfer expressions between the bubble growth/collapse rate and the corresponding evaporation/condensation sources terms of the Zwart and Singhal cavitation models have been obtained as equations (4-7) and (4-8). As a result, an improved cavitation models for Singhal are formulated as Equation (4-9), and for Zwart as Equation

(4-10). Meanwhile, their respective original versions are presented as Equations (4-11) and (4-12).

$$R\ddot{R} + \frac{3}{2}\dot{R}^2 = \left(\frac{p_v - p_\infty}{\rho_l} \right) + \frac{P_G}{\rho_l} - \frac{4\mu_l}{R\rho_l} \dot{R} - \frac{2S}{R\rho_l} \quad (4-1)$$

$$R\ddot{R} + \frac{3}{2}\dot{R}^2 = \frac{p_v - p_\infty}{\rho_l} \quad (4-2)$$

$$\dot{R}_{asym, evap} = \sqrt{\frac{2}{3} \frac{p_v - p_\infty}{\rho_l}} \quad p_v \geq p_\infty \quad (4-3)$$

$$\dot{R}_{asym, cond} = \left(\frac{R_0}{R} \right)^{\frac{3}{2}} \sqrt{\frac{2}{3} \frac{p_\infty - p_v}{\rho_l}} \quad p_v \leq p_\infty \quad (4-4)$$

$$\dot{R}_{evap} = \sqrt{\frac{2}{3} \frac{p_v - p_\infty}{\rho_l}} \quad p_v \geq p_\infty \quad (4-5)$$

$$\dot{R}_{cond} = \sqrt{\frac{2}{3} \frac{p_\infty - p_v}{\rho_l}} \quad p_v \leq p_\infty \quad (4-6)$$

$$\dot{m}_{c, Zwart} = F_{cond, Zwart} \frac{2.6\sqrt{\alpha}\rho_v}{R} \sqrt{\frac{2}{3} \frac{(p_\infty - p_v)}{\rho_l}} \quad p_\infty \geq p_v \quad (4-7)$$

$$\dot{m}_{c, Singhal} = F_{cond, Singhal} \frac{\max(1.0, \sqrt{k})}{S} \rho_l \rho_l \sqrt{\frac{2}{3} \frac{(p_\infty - p_v)}{\rho_l}} \frac{0.87\sqrt{\alpha}\rho_v}{\rho_m} \quad p_\infty \geq p_v \quad (4-8)$$

$$\dot{m} = \begin{cases} \dot{m}_e = F_{vap, Singhal} \frac{\max(1.0, \sqrt{k})}{S} \rho_l \rho_v \sqrt{\frac{2}{3} \frac{(p_v - p)}{\rho_l}} \left(1 - \frac{\alpha\rho_v}{\rho_m}\right) & p \leq p_v \\ \dot{m}_c = F_{cond, Singhal} \frac{\max(1.0, \sqrt{k})}{S} \rho_l \rho_l \sqrt{\frac{2}{3} \frac{(p - p_v)}{\rho_l}} \frac{0.87\sqrt{\alpha}\rho_v}{\rho_m} & p \geq p_v \end{cases} \quad (4-9)$$

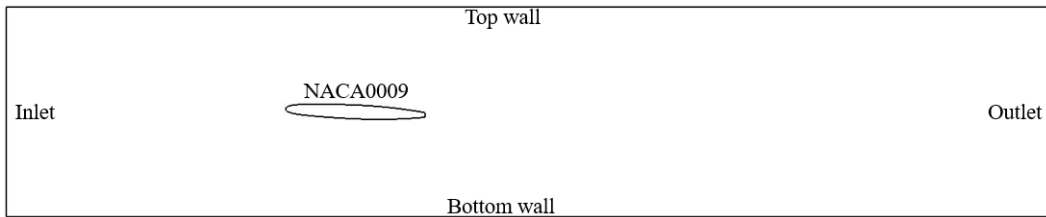
$$\dot{m} = \begin{cases} \dot{m}_e = F_{vap, Zwart} \frac{3\alpha_{nuc}(1-\alpha)\rho_v}{R} \sqrt{\frac{2}{3} \frac{(p_v - p)}{\rho_l}} & p \leq p_v \\ \dot{m}_c = F_{cond, Zwart} \frac{2.6\sqrt{\alpha}\rho_v}{R} \sqrt{\frac{2}{3} \frac{(p - p_v)}{\rho_l}} & p \geq p_v \end{cases} \quad (4-10)$$

$$\dot{m} = \begin{cases} \dot{m}_e = F_{vap, Singhal} \frac{\max(1.0, \sqrt{k})}{S} \rho_l \rho_v \sqrt{\frac{2}{3} \frac{(p_v - p)}{\rho_l}} \left(1 - \frac{\alpha\rho_v}{\rho_m}\right) & p \leq p_v \\ \dot{m}_c = F_{cond, Singhal} \frac{\max(1.0, \sqrt{k})}{S} \rho_l \rho_l \sqrt{\frac{2}{3} \frac{(p - p_v)}{\rho_l}} \frac{\alpha\rho_v}{\rho_m} & p \geq p_v \end{cases} \quad (4-11)$$

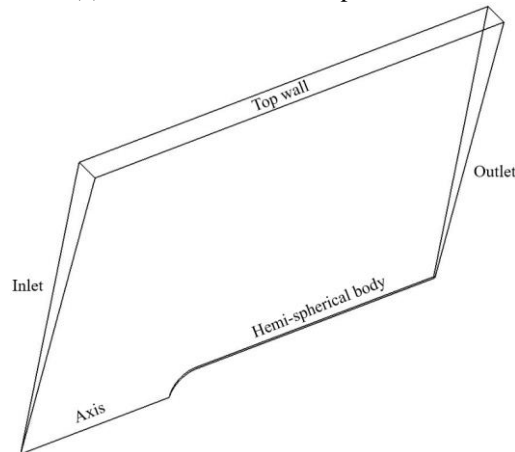
$$\dot{m} = \begin{cases} \dot{m}_e = F_{vap,Zwart} \frac{3\alpha_{nuc}(1-\alpha)\rho_v}{R} \sqrt{\frac{2(p_v - p)}{3\rho_l}} & p \leq p_v \\ \dot{m}_c = F_{cond,Zwart} \frac{3\alpha\rho_v}{R} \sqrt{\frac{2(p - p_v)}{3\rho_l}} & p \geq p_v \end{cases} \quad (4-12)$$

4.2 Test cases and mesh convergence study

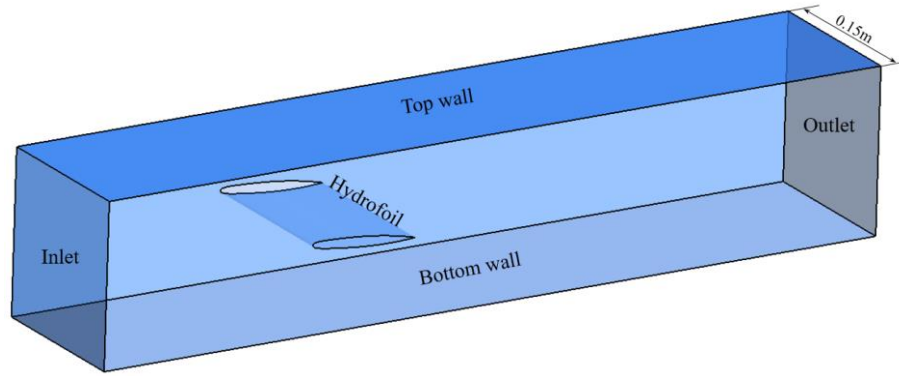
The corrected cavitation models have been evaluated by modelling three cavitation experiments with two different cavitation patterns. Two test cases for attached cavitating flow were selected, one corresponds to a cavitating flow around a NACA0009 2D hydrofoil for various free stream velocities, and another one is around a submerged hemi-sphere cylindrical body. In particular, for each of these two cases, the simulation has been done under two different cavitation numbers with a fixed Reynolds number. In addition, the corrected models have also validated by conducting unsteady sheet/cloud cavitation simulation around another NACA0009 hydrofoil. For these three test cases, the computational domains were built based on the respective tunnel dimensions and they are schematically plotted in Figure. 4.1 in which the corresponding boundary settings are also presented. The operation conditions for each test case are summarized in Table 4.1.



(a) NACA0009 2D computational domain



(b) Hemi-spherical body computational domain



(c) NACA0009 3D computational domain

Figure 4.1: Computational domains with named boundaries. Reproduced from [102].

Table 4.1: Flow conditions of the simulated cases. Reproduced from [102].

Test cases	Hemispherical body	NACA0009 (steady)	NACA0009 (unsteady)
U_{inf}	10 m/s	20 m/s	20 m/s
Re	$2.5 \cdot 10^5$	$2 \cdot 10^6$	$2 \cdot 10^6$
σ	0.5, 0.3	0.9, 0.8	1.2

Before the validation, a mesh convergence study has been conducted by applying the Grid Convergence Index method (GCI). For each case, three meshes with different mesh densities were created. The GCI value has been determined by monitoring the lift and drag coefficients for the NACA0009 hydrofoil and the value of pressure and velocity at the cutting point between the hemispherical fore-body and a cylindrical aft-body for the hemi-spherical body. And the mesh number, the monitor values and the resulted GCI values for each case are summarized in Table 4.2. And Figure 4.2 shows the details of the mesh being selected.

Table 4.2. Features of the grids and numerical uncertainty evaluation based on the GCI indexes. Reproduced from [102].

NACA0009 (steady)	Elements	C_l	GCI	C_d	GCI
Coarse	27,961	0.3469	GCI _{fine} =0.04% GCI _{medium} =0.11%	0.0147	GCI _{fine} =0.45% GCI _{medium} =1.3%
Medium	55,746	0.3464		0.0144	
Fine	110,169	0.3462		0.0143	
Hemi-spherical body	Elements	Pressure [Pa]	GCI	Velocity [m/s]	GCI
Coarse	33,579	74798	GCI _{fine} =0.17% GCI _{medium} =0.09%	11.82	GCI _{fine} =0.05% GCI _{medium} =0.36%
Medium	68,775	74843		12.03	
Fine	137,448	74923		12.06	
NACA0009 (unsteady)	Elements	C_l	GCI	C_d	GCI
Coarse	2,737,026	0.6097	GCI _{fine} =0.001% GCI _{medium} =0.04%	0.0143	GCI _{fine} =0.8% GCI _{medium} =3.7%
Medium	5,487,038	0.6208		0.0130	
Fine	11,253,879	0.6206		0.0127	

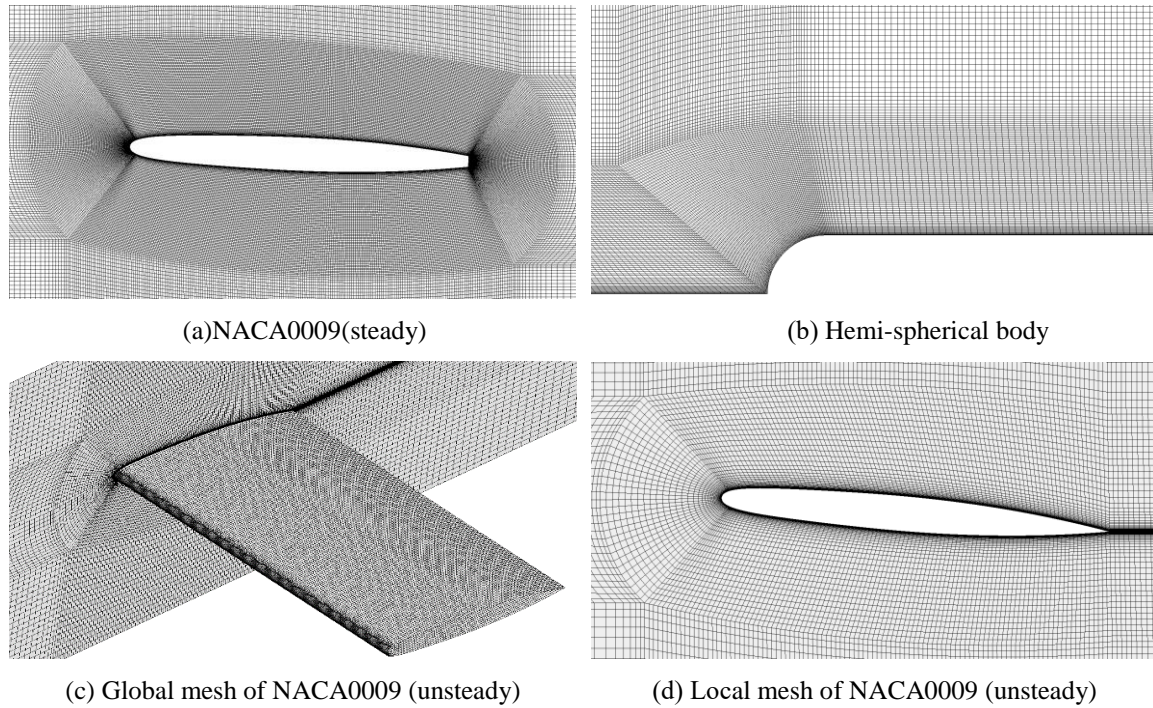


Figure 4.2: Details of the mesh. Reproduced from [102].

4.3 Cavitation model Validation

For attached cavitation, the experimental pressure coefficient, C_p , has been used to validate the numerical model, and the vapor volume fractions obtained with the original and the corrected Zwart and Singhal models have been compared for these two test cases. For case of NACA0009 hydrofoil at cavitation number $\sigma=0.9$, Figure 4.3 shows the experimental and the numerical C_p on the hydrofoil surface obtained with both the original and the corrected models. The corresponding vapor volume fraction distribution and the condensation rate distribution on the fluid domain are shown in Figures 4.4 and 4.5, respectively. These results indicate that the corrected cavitation models improve the accuracy of the pressure distribution at the closure region of the cavity and provides a relatively shorter cavity, as well as predicts a higher condensation rate. Moreover, when the cavitation number decreases to 0.8, analogous results have been obtained as presented in Figures 4.6 and 4.7. Therefore, the corrected models perform better than the original models because they predict a more agreeable results with the experiment. In addition, the performance of the original and corrected cavitation models is further evaluated for the hemi-spherical body. Figures 4.8 and 4.9 show the results at $\sigma=0.5$, and Figures 4.10 and 4.11 at $\sigma=0.3$. Similarly, it is confirmed again that the corrected models can predict a more accurate C_p distribution and a stronger adverse pressure gradient at the cavity closure region.

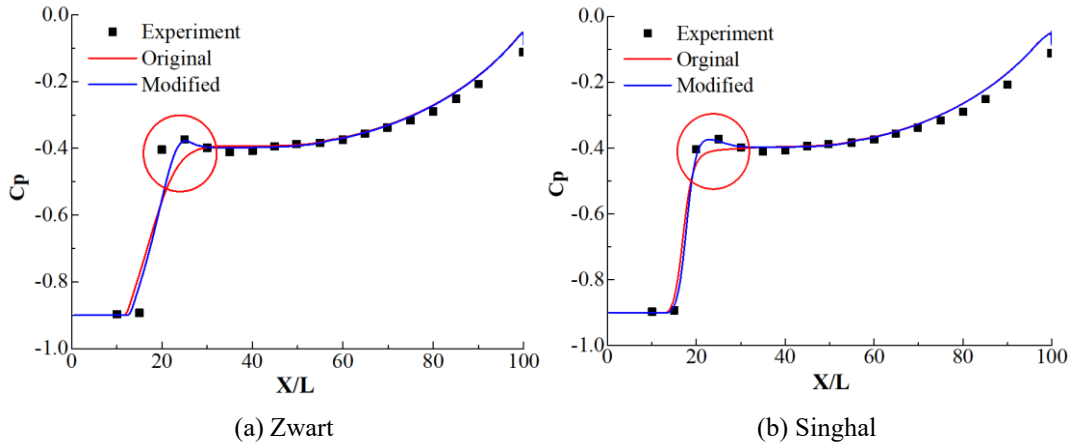


Figure 4.3: Comparison between computed and measured C_p over NACA0009, $\sigma=0.9$. Reproduced from [102].

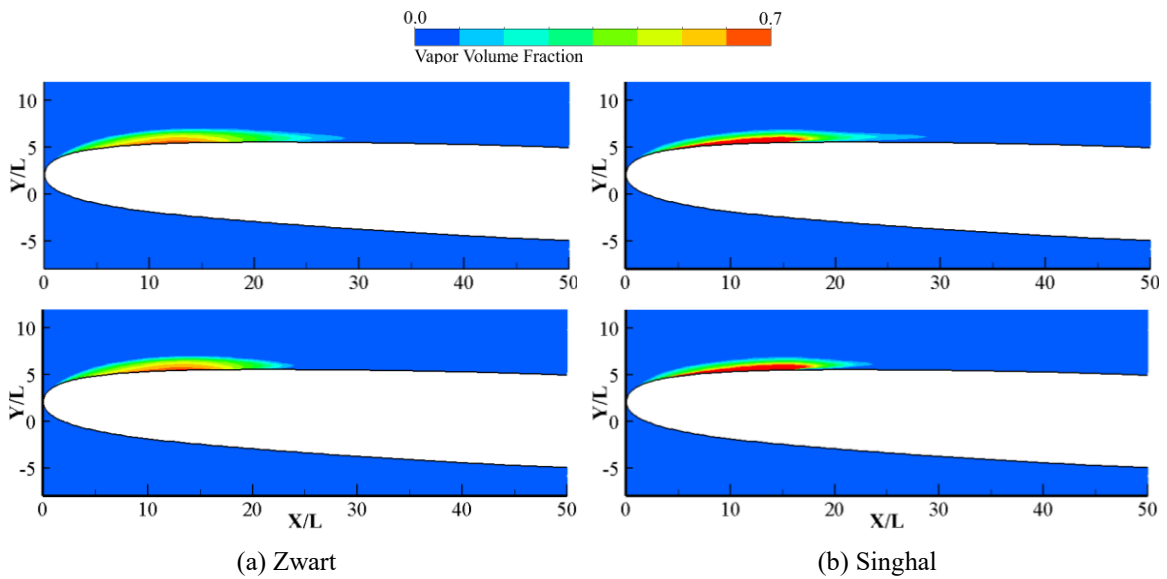


Figure 4.4: Vapor volume fraction distribution obtained by the original (top) and the corrected (bottom) cavitation model at $\sigma = 0.9$. Reproduced from [102].

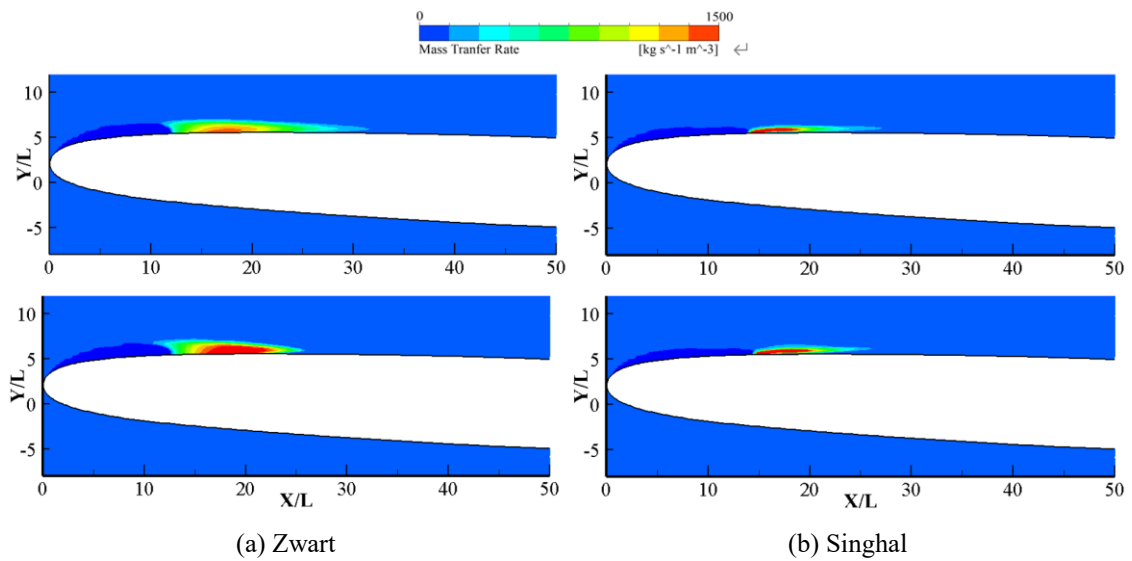


Figure 4.5: Condensation rate distribution obtained by the original (top) and the modified (bottom) cavitation model at $\sigma = 0.9$. Reproduced from [102].

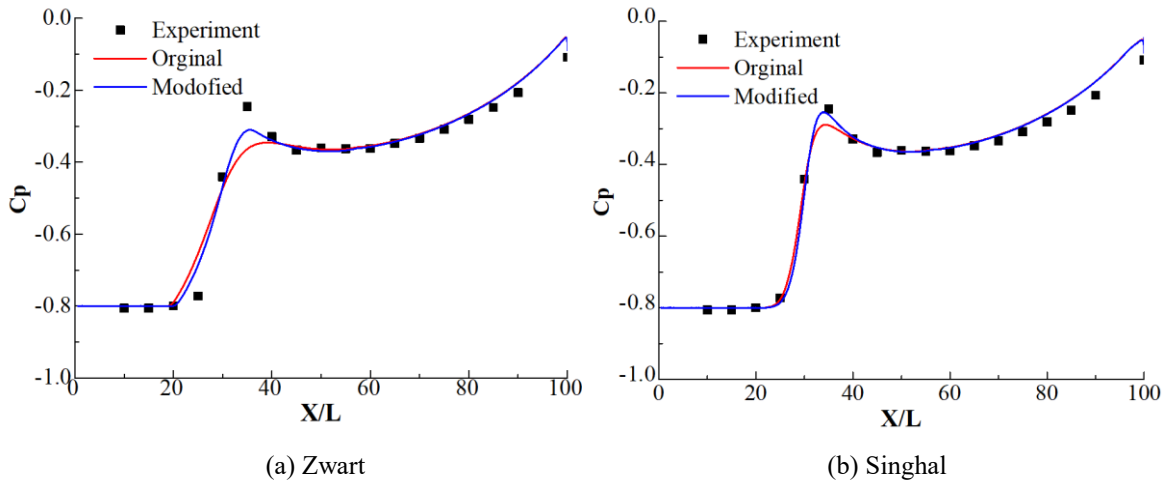


Figure 4.6: Comparison between the computed and the measured C_p values on the NACA0009 at $\sigma = 0.8$. Reproduced from [102].

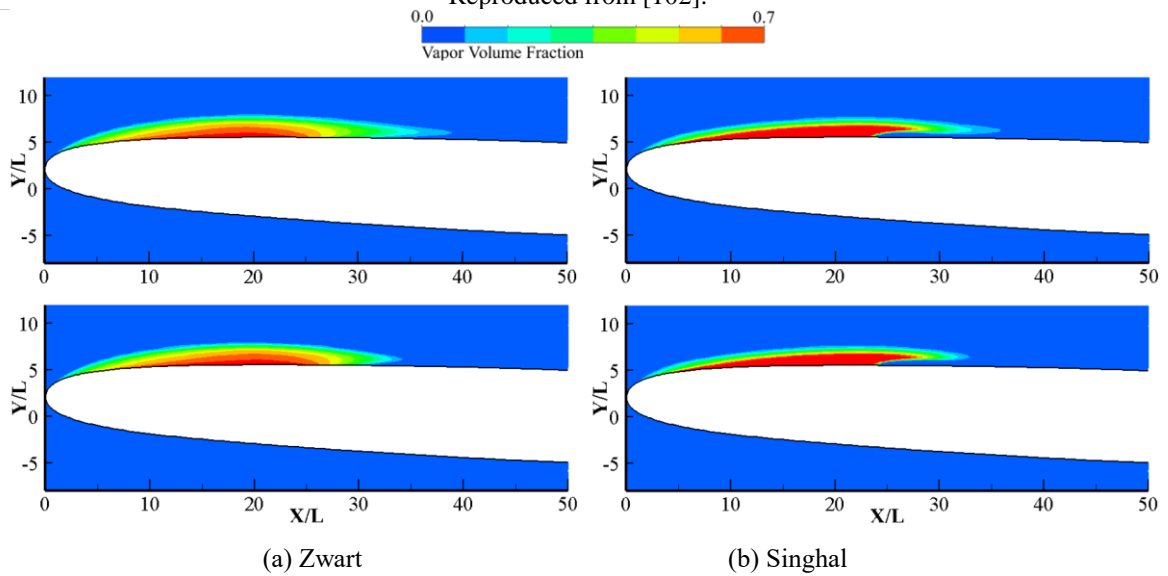


Figure 4.7: Vapor volume fraction distribution obtained by the original (top) and the corrected (bottom) cavitation model at $\sigma = 0.8$. Reproduced from [102].

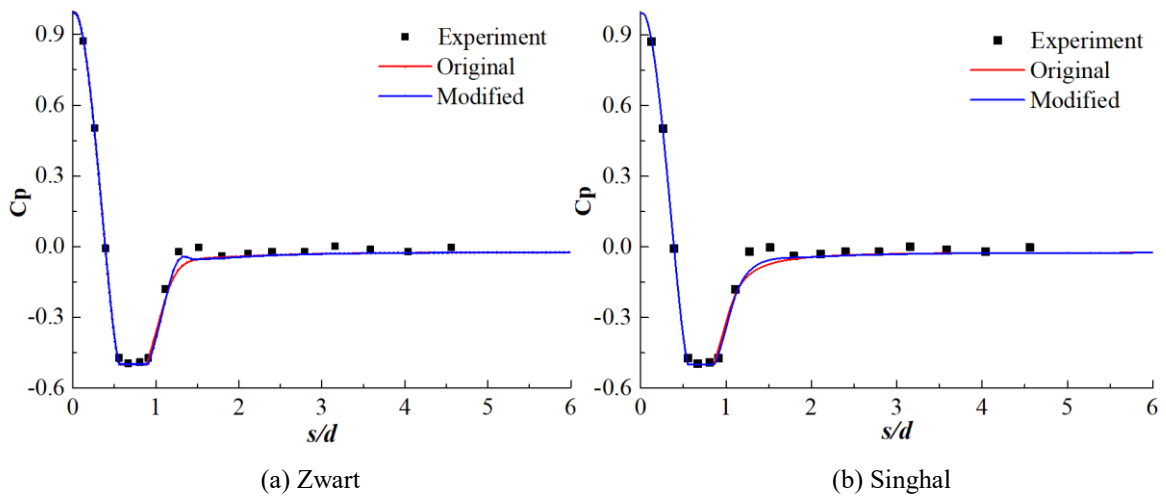


Figure 4.8: Comparison between the computed and the measured C_p values over the hemi-spherical body at $\sigma = 0.5$. Reproduced from [102].

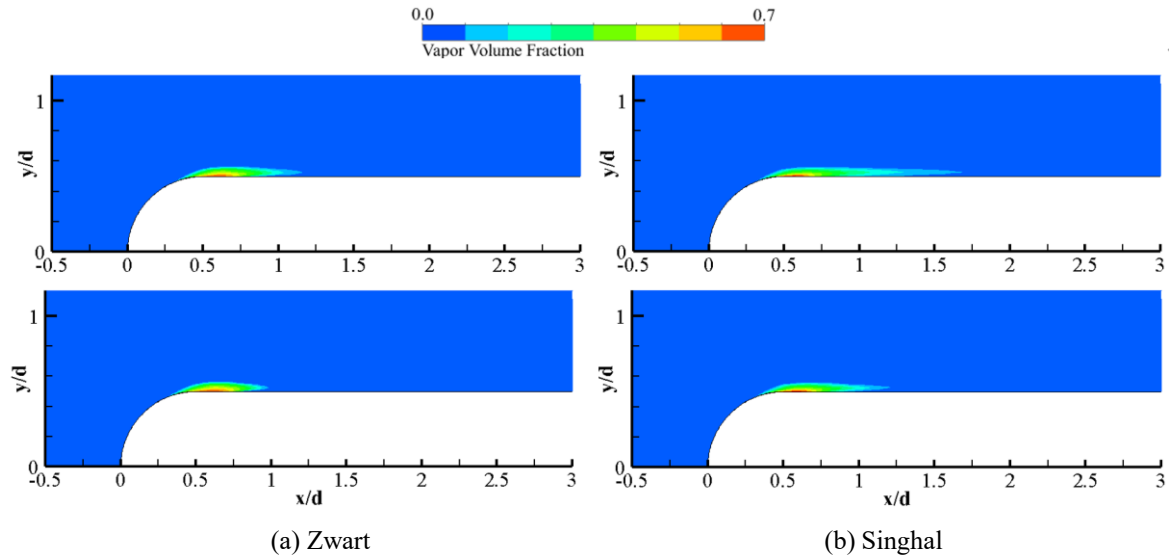


Figure 4.9: Vapor volume fraction distribution obtained by the original (top) and the corrected (bottom) cavitation model at $\sigma = 0.5$. Reproduced from [102].

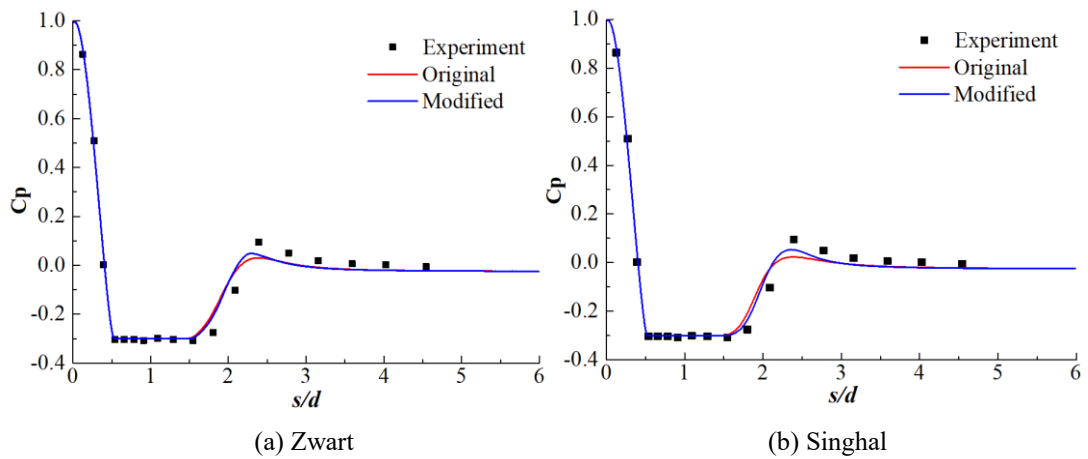


Figure 4.10: Comparison between the computed and the measured C_p values on the hemi-spherical body at $\sigma = 0.3$. Reproduced from [102].

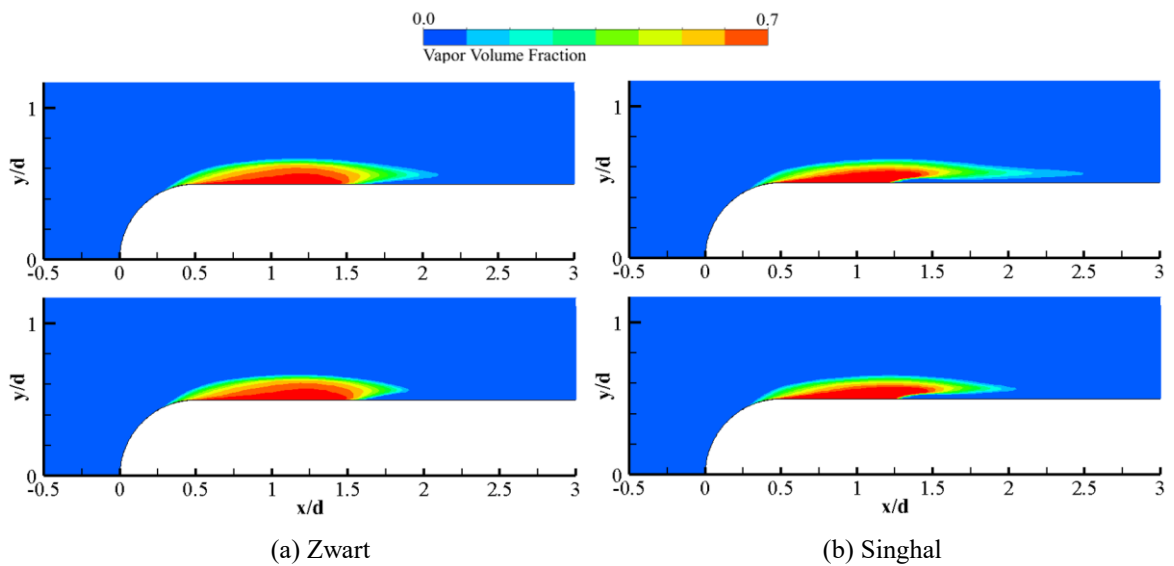
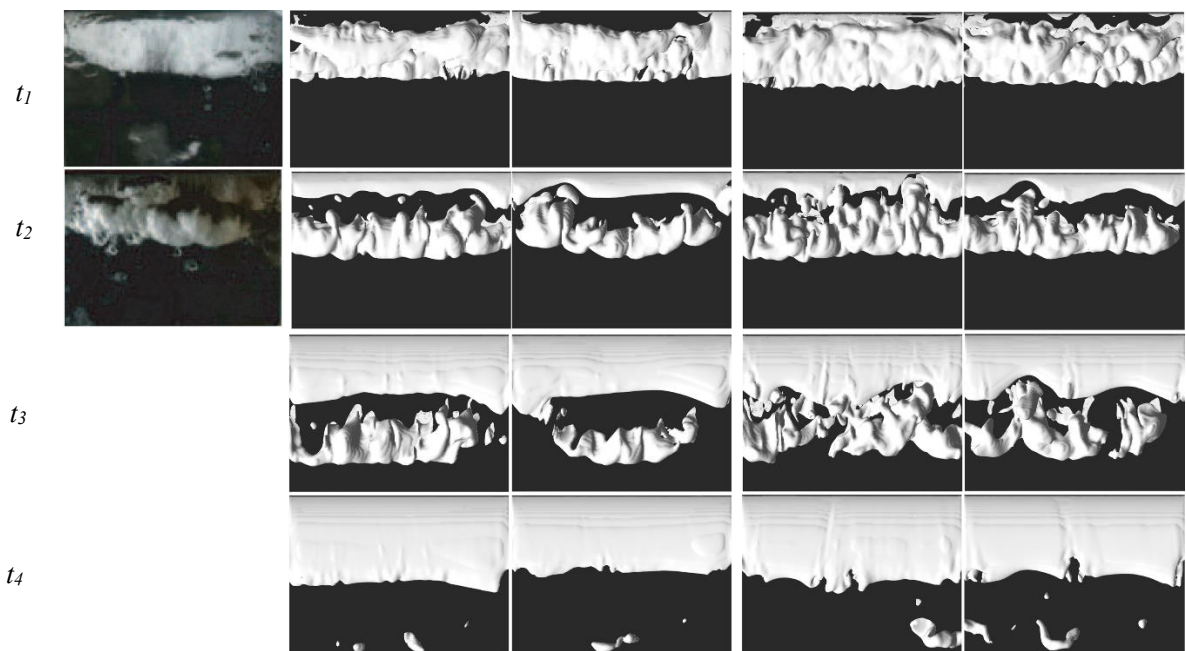


Figure 4.11: Vapor volume fraction distribution obtained by original (top) and modified (bottom) cavitation model, $\sigma = 0.3$. Reproduced from [102].

For test case of unsteady cavitation pattern, the shedding frequency and the cavity morphology predicted by the original and by the corrected model have been compared with the experimental results. Figure 4.12 compares the cloud cavitation evolutions during one shedding period, and Table 4.3 lists the predicted shedding frequency and the corresponding deviations. Generally speaking, these two corrected model improve the prediction to different extents especially for the Zwart model. In conclusion, the corrected Zwart model predicts a closer shedding frequency to the experiment, showing a significant improvement with a reduction of the deviation from 18.1% to 12.9%, and it also shows a clear reduction of the maximum cavity length and can better provide the morphology and evolution of the cavitation detachment.



(a) Experiment (b) Original Zwart (c) Modified Zwart (d) Original Singhal (e) Modified Singhal

Figure 4.12: Comparison of experimental and numerical cloud cavitation evolutions during one shedding period using the original and the modified cavitation models. The simulation results show an isosurface of $\alpha = 0.1$. Reproduced from [102].

Table 4.3. Numerical and experimental shedding frequencies, deviations and improvements of modified models. Reproduced from [102].

Cavitation Model	f_{num} [Hz]	f_{exp} [Hz]	Deviation [%]	Improvement [%]
Original Zwart	98.3	120	18.1	5.2
Modified Zwart	104.5	120	12.9	
Original Singhal	101.7	120	15.3	0.9
Modified Singhal	102.7	120	14.4	

Chapter 5 Numerical prediction of Cavitation Erosion

A numerical investigation of the erosion aggressiveness of leading edge unsteady cloud cavitation based on the energy balance approach has been carried out to ascertain the main damaging mechanisms and the influence of the free stream flow velocity. A systematic approach has permitted the determination of the influence of several parameters on the spatial and temporal distribution of the erosion results comprising the selection of the cavitation model and the collapse driving pressure. In particular, the Zwart, Sauer and Kunz cavitation models have been compared as well as the use of instantaneous versus average pressure values. The numerical results have been compared against a series of experimental results obtained from pitting tests on copper and stainless steel specimens. Several cavitation erosion indicators have been defined and their accuracy to predict the experimental observations has been assessed and confirmed when using a material-dependent damaging threshold level. In summary, the use of the average pressure levels during a sufficient number of simulated shedding cycles combined with the Sauer cavitation model are the recommended parameters to achieve reliable results that reproduce the main erosion mechanisms found in cloud cavitation. Moreover, the proposed erosion indicators follow a power law as a function of the free stream flow velocity with exponents ranging from 3 to 5 depending on their definition.

The complete content of this chapter can be found in the paper entitled “Numerical Simulation of Cavitation Erosion Aggressiveness Induced by Unsteady Cloud Cavitation” and published in 2020 in the open access journal “Applied Sciences” with an Impact Factor of 2.47 (second quartile 2) [103] which can be found in the Annex B of this thesis report.

Chapter 6 Conclusions and outlook

6.1 Conclusions

The present investigation aimed to accurately capture numerically the unsteady cavitation dynamic behavior with an economical computational cost by putting an emphasis on the cavity shedding frequency and its associated erosion intensity. Summing up all the investigations conducted in this thesis, the following conclusions have been obtained:

- Regarding the best turbulence model and configuration set-ups, three widely used eddy-viscosity models have been employed to simulate unsteady cavitation under different operating conditions, and the results show that the numerical results are more sensitive to near wall mesh resolution than to time step, number of iterations and number of mesh elements. For the SST model, an average y^+ equal to 2 must be used, meanwhile for the $k-\varepsilon$ and RNG models a coarser grid resolution is sufficient. And generally speaking, the SST model can predict more accurate results than the standard $k-\varepsilon$ and the RNG models when the Reboud's correction is used.
- Regarding the improvement of the cavitation models, the influence of the empirical constants on the cavity dynamics has been analyzed first. It has been found that increasing the vaporization coefficient F_v can predict larger amounts of vapor inside the cavities with thinner interfaces between vapor and water phases, and that increasing the condensation coefficient F_c can capture the instantaneous collapse of the shed cloud and the induced pressure pulse on the hydrofoil surface. The optimal range of empirical coefficients is from 300 to 500 for F_v , and from 0.08 to 0.1 for F_c , based on a response surface optimization method. Secondly, two cavitation models (Zwart and Singhal) were corrected by considering the second order term in the Rayleigh-Plesset equation, and the performance of corrected model was evaluated by comparing with the original version. For modelling the attached cavitation around a NACA0009 hydrofoil and a hemispherical body, the corrected models predict better the pressure gradients at the closure region of the attached cavity. Moreover, the predicted cavity length is reduced which is closer to the experimental observations. For simulating unsteady cavitation around a NACA0009 hydrofoil, the corrected model improves the experimentally observed shedding frequency as well as the morphology and evolution of the cavitation detachment, especially for corrected Zwart models. All of these demonstrated that the original models underestimate the mass transfer rate in the vapor condensation region and, therefore, the corrected models improve the performance of the simulation.
- Regarding the prediction of cavitation erosion of unsteady cloud cavitation on a 2D

hydrofoil, an erosion model based on an energy balance approach has been implemented and the influence of the driving pressure and of the cavitation model on the erosion intensity and erosion distribution has been assessed. It has been found that the selection of the driving pressure to estimate the power of the cavity collapse has a significant effect on the prediction of the erosion power and the use of the average pressure gives more similar results to the experiment than the use of the instantaneous pressure. The selection of the cavitation models influences significantly the power loaded on the hydrofoil surface both in terms of magnitude and spatial distribution along the chord. For the cases considered in the present study, the Sauer model performs better than the Kunz and Zwart ones. In addition, two main erosion mechanisms have been established. One is induced by the high frequency of low-intensity collapses taking place at the closure region of the main sheet cavity attached to the hydrofoil surface. The other one is induced by the low frequency and high intensity collapses of the shed cloud cavities. Finally, the dependency of erosion intensity on free stream velocity has been found out by taking into account the collapse efficiency and the shedding frequency and different power laws have been obtained. More specifically, the effective power load law grows with an exponent of 4, and the erosion aggressiveness per unit time grows with an exponent of 5.

6.2 Outlook

There are some further investigations needed to do in the near future as a continuation of the present work.

- Since the current investigations are only valid for cavitating hydrofoils in high speed water tunnels, the next step would be to simulate more complex cavitation phenomena in actual hydraulic machines such as turbines and pumps, and to compare the erosion simulation results with the available experiment results.
- Consider the use and validation of the second generation of the URANS model [104], which is not highly dependent on the mesh resolution but can provide more detailed and realistic flow information. For that, try to use such model to simulate a cavitation flow with similar precision than the DES or LES and confirm its lower computational cost.
- Although the erosion method employed in the present study can well predict the erosion distribution, it provides a quantification of the erosive power which is independent of the material properties. Hence, in the next step, this is necessary to find a way to build the relationship between the cavitation aggressiveness and the actual material erosion. For example, this could be addressed by using the compressible approach to predict the pressure loaded on the hydrofoil surface and relate it to actual damage.

References

- [1] Franc, J. P., & Michel, J. M. (2006). Fundamentals of cavitation (Vol. 76). Springer science & Business media.
- [2] Franc, J. P. (2006). Physics and control of cavitation. GRENOBLE UNIV (FRANCE).
- [3] Escaler, X., Egusquiza, E., Farhat, M., Avellan, F., & Coussirat, M. (2006). Detection of cavitation in hydraulic turbines. *Mechanical systems and signal processing*, 20(4), 983-1007.
- [4] Kumbhar, V.M. & Jagdale, S.S. & Shastri, Rajveer. (2015). UNDERWATER SHIP RADIATED NOISE MODEL.
- [5] Savchenko, Y. (2001). Supercavitation-problems and perspectives. <http://resolver.caltech.edu/cav2001:lecture.003>.
- [6] Avellan, F. (2004). Introduction to cavitation in hydraulic machinery (No. CONF). Politehnica University of Timișoara.
- [7] Jayaprakash, A., Hsiao, C. T., & Chahine, G. (2012). Numerical and experimental study of the interaction of a spark-generated bubble and a vertical wall. *Journal of Fluids Engineering*, 134(3).
- [8] Philipp, A., & Lauterborn, W. (1998). Cavitation erosion by single laser-produced bubbles. *Journal of Fluid Mechanics*, 361, 75-116.
- [9] Tomita, Y., & Shima, A. (1990). High-speed photographic observations of laser-induced cavitation bubbles in water. *Acta Acustica united with Acustica*, 71(3), 161-171.
- [10] Hammitt, F. G. (1979). Cavitation erosion state of art and predicting capability.
- [11] Benjamin, T. B., & Ellis, A. T. (1966). The collapse of cavitation bubbles and the pressures thereby produced against solid boundaries. *Philosophical Transactions for the Royal Society of London. Series A, Mathematical and Physical Sciences*, 221-240.
- [12] Fujikawa, S., & Akamatsu, T. (1980). Effects of the non-equilibrium condensation of vapour on the pressure wave produced by the collapse of a bubble in a liquid. *Journal of Fluid Mechanics*, 97(3), 481-512.
- [13] Fortes Patella, R., Challier, G., Reboud, J. L., & Archer, A. (2001). Cavitation Erosion Mechanism: Numerical Simulations of the Interaction Between Pressure Waves and Solid Boundaries. <http://resolver.caltech.edu/cav2001:sessionA3.006>.
- [14] Tomita, Y., & Shima, A. (1986). Mechanisms of impulsive pressure generation and damage pit formation by bubble collapse. *Journal of Fluid Mechanics*, 169, 535-564.
- [15] Kim, K. H., Chahine, G., Franc, J. P., & Karimi, A. (Eds.). (2014). Advanced experimental and numerical techniques for cavitation erosion prediction (Vol. 106). Springer.
- [16] Chahine, G. L., Annassami, R., Hsiao, C. T., & Harris, G. S. (2006). Scaling rules for the prediction on UNDEX bubble re-entering jet parameters. *SAVIAC Critical Technologies in Shock and Vibration*, 4(1), 1-12.
- [17] Franc, J. P., Riondet, M., Karimi, A., & Chahine, G. L. (2012). Material and velocity effects on cavitation erosion pitting. *Wear*, 274, 248-259.

- [18] Franc, J. P., & Michel, J. M. (1997). Cavitation erosion research in France: the state of the art. *Journal of Marine Science and Technology*, 2(4), 233-244.
- [19] Hattori, S., Hirose, T., & Sugiyama, K. (2010). Prediction method for cavitation erosion based on measurement of bubble collapse impact loads. *Wear*, 269(7-8), 507-514.
- [20] Pope, S. B. (2001). *Turbulent flows*.
- [21] Lu, T., Samulyak, R., & Glimm, J. (2007). Direct numerical simulation of bubbly flows and application to cavitation mitigation.
- [22] Seo, J. H., Moon, Y. J., & Shin, B. R. (2008). Prediction of cavitating flow noise by direct numerical simulation. *Journal of Computational Physics*, 227(13), 6511-6531.
- [23] Smagorinsky, J. (1963). General circulation experiments with the primitive equations: I. The basic experiment. *Monthly weather review*, 91(3), 99-164.
- [24] Germano, M., Piomelli, U., Moin, P., & Cabot, W. H. (1991). A dynamic subgrid-scale eddy viscosity model. *Physics of Fluids A: Fluid Dynamics*, 3(7), 1760-1765.
- [25] Lilly, D. K. (1992). A proposed modification of the Germano subgrid-scale closure method. *Physics of Fluids A: Fluid Dynamics*, 4(3), 633-635.
- [26] Nicoud, F., & Ducros, F. (1999). Subgrid-scale stress modelling based on the square of the velocity gradient tensor. *Flow, turbulence and Combustion*, 62(3), 183-200.
- [27] Menter, F. R. (2012). *Best practice: scale-resolving simulations in ANSYS CFD*. ANSYS Germany GmbH, 1.
- [28] Gopalan, H., Heinz, S., & Stöllinger, M. K. (2013). A unified RANS–LES model: Computational development, accuracy and cost. *Journal of Computational Physics*, 249, 249-274.
- [29] Spalart, P. R. (1997). Comments on the feasibility of LES for wings, and on a hybrid RANS/LES approach. In *Proceedings of first AFOSR international conference on DNS/LES*. Greyden Press.
- [30] Spalart, P., & Allmaras, S. (1992, January). A one-equation turbulence model for aerodynamic flows. In *30th aerospace sciences meeting and exhibit* (p. 439).
- [31] Menter, F., Kuntz, M., & Bender, R. (2003, January). A scale-adaptive simulation model for turbulent flow predictions. In *41st aerospace sciences meeting and exhibit* (p. 767).
- [32] Yakubov, S., Cankurt, B., Maquil, T., Schiller, P., Abdel-Maksoud, M., & Rung, T. (2013). Advanced lagrangian approaches to cavitation modelling in marine applications. In *MARINE 2011, IV International Conference on Computational Methods in Marine Engineering* (pp. 217-234). Springer, Dordrecht.
- [33] Abdel-Maksoud, M., Hänel, D., & Lantermann, U. (2010). Modeling and computation of cavitation in vortical flow. *International Journal of Heat and Fluid Flow*, 31(6), 1065-1074.
- [34] Oweis, G. F., Van der Hout, I. E., Iyer, C., Tryggvason, G., & Ceccio, S. L. (2005). Capture and inception of bubbles near line vortices. *Physics of Fluids*, 17(2), 022105.
- [35] Giannadakis, E., Gavaises, M., Roth, H., & Arcoumanis, C. (2004, September). Cavitation modelling in single-hole diesel injector based on Eulerian-Lagrangian approach. In *Proc. THIESEL International Conference on Thermo-and Fluid Dynamic Processes in Diesel Engines*.

- [36] Shams, E., Finn, J., & Apte, S. V. (2011). A numerical scheme for Euler–Lagrange simulation of bubbly flows in complex systems. *International Journal for Numerical Methods in Fluids*, 67(12), 1865-1898.
- [37] Ghahramani, E., Arabnejad, M. H., & Bensow, R. E. (2018). Realizability improvements to a hybrid mixture-bubble model for simulation of cavitating flows. *Computers & Fluids*, 174, 135-143.
- [38] Hänsch, S., Lucas, D., Krepper, E., & Höhne, T. (2012). A multi-field two-fluid concept for transitions between different scales of interfacial structures. *International Journal of Multiphase Flow*, 47, 171-182.
- [39] Ma, J., Hsiao, C. T., & Chahine, G. L. (2017). A physics based multiscale modeling of cavitating flows. *Computers & fluids*, 145, 68-84.
- [40] Hsiao, C. T., Ma, J., & Chahine, G. L. (2017). Multiscale tow-phase flow modeling of sheet and cloud cavitation. *International Journal of Multiphase Flow*, 90, 102-117.
- [41] Chen, L., Zhang, L., Peng, X., & Shao, X. (2019). Influence of water quality on the tip vortex cavitation inception. *Physics of Fluids*, 31(2), 023303.
- [42] Farrell, K. J. (2003). Eulerian/Lagrangian analysis for the prediction of cavitation inception. *J. Fluids Eng.*, 125(1), 46-52.
- [43] Eskilsson, C., Bensow, R. E., & Kinnas, S. (2015). Estimation of cavitation erosion intensity using CFD: numerical comparison of three different methods. In *Proceedings of the 4th International Symposium on Marine Propulsors*, Austin, TX, USA.
- [44] Ochiai, N., Iga, Y., Nohmi, M., & Ikohagi, T. (2010). Numerical prediction of cavitation erosion intensity in cavitating flows around a Clark Y 11.7% hydrofoil. *Journal of Fluid Science and Technology*, 5(3), 416-431.
- [45] Hsiao, C. T., & Chahine, G. L. (2005). Scaling of tip vortex cavitation inception noise with a bubble dynamics model accounting for nuclei size distribution. *J. Fluids Eng.*, 127(1), 55-65.
- [46] Saurel, R., Petitpas, F., & Abgrall, R. (2008). Modelling phase transition in metastable liquids: application to cavitating and flashing flows. *Journal of Fluid Mechanics*, 607, 313.
- [47] Baer, M. R., & Nunziato, J. W. (1986). A two-phase mixture theory for the deflagration-to-detonation transition (DDT) in reactive granular materials. *International journal of multiphase flow*, 12(6), 861-889.
- [48] Le Métayer, O., Massoni, J., & Saurel, R. (2005). Modelling evaporation fronts with reactive Riemann solvers. *Journal of Computational Physics*, 205(2), 567-610.
- [49] Saurel, R., & Lemetayer, O. (2001). A multiphase model for compressible flows with interfaces, shocks, detonation waves and cavitation. *Journal of Fluid Mechanics*, 431, 239.
- [50] Ha, C. T., Park, W. G., & Jung, C. M. (2015). Numerical simulations of compressible flows using multi-fluid models. *International Journal of Multiphase Flow*, 74, 5-18.
- [51] Saurel, R., Petitpas, F., & Berry, R. A. (2009). Simple and efficient relaxation methods for interfaces separating compressible fluids, cavitating flows and shocks in multiphase mixtures. *journal of Computational Physics*, 228(5), 1678-1712.

- [52] Kapila, A. K., Menikoff, R., Bdzil, J. B., Son, S. F., & Stewart, D. S. (2001). Two-phase modeling of deflagration-to-detonation transition in granular materials: Reduced equations. *Physics of fluids*, 13(10), 3002-3024.
- [53] Ait Bouziad, Y. (2005). Physical modelling of leading edge cavitation (No. THESIS). EPFL.
- [54] Chen, Y., & Heister, S. D. (1994). A numerical treatment for attached cavitation. *Journal of Fluids Engineering*; (United States), 116(3).
- [55] Deshpande, M., Feng, J., & Merkle, C. (1997). Numerical modeling of the thermodynamic effects of cavitation. *Journal of fluids engineering*, 119(2), 420-427.
- [56] Wang, G., Senocak, I., Shyy, W., Ikohagi, T., & Cao, S. (2001). Dynamics of attached turbulent cavitating flows. *Progress in Aerospace sciences*, 37(6), 551-581.
- [57] Huang, C. K. (2017). Turbulence and cavitation: applications in the NSMB and OpenFOAM solvers (Doctoral dissertation).
- [58] Decaix, J., & Goncalves, E. (2013). Compressible effects modeling in turbulent cavitating flows. *European Journal of Mechanics-B/Fluids*, 39, 11-31.
- [59] Delannoy, Y. and Kueny, J. (1990). Two phase flow approach in unsteady cavitation modelling. In *Cavitation and Multiphase Flow Forum, ASME-FED*, vol. 98, pp153-158.
- [60] Schmidt, D. (1997). Cavitation in Diesel fuel injector nozzles. PhD thesis, University of Wisconsin-Madison.
- [61] Eça, L., Toxopeus, S., & Terwisga Tv, S. H. (2009). Best Practice Guidelines for the application of Computational Fluid Dynamics in Marine Hydrodynamics. Tech. rep., VIRTUE-The Virtuel Tank Utility in Europe, Affiliation: VIRTUE Project.
- [62] Mani, K. V., Cervone, A., & Hickey, J. P. (2017). Turbulence modeling of cavitating flows in liquid rocket turbopumps. *Journal of Fluids Engineering*, 139(1), 011301.
- [63] Niedźwiedzka, A., Schnerr, G. H., & Sobieski, W. (2016). Review of numerical models of cavitating flows with the use of the homogeneous approach. *Archives of Thermodynamics*, 37.
- [64] Zwart, P. J., Gerber, A. G., & Belamri, T. (2004, May). A twophase flow model for predicting cavitation dynamics. In *Fifth international conference on multiphase flow* (Vol. 152), Yokohama, Japan.
- [65] Kunz, R. F., Boger, D. A., Stinebring, D. R., Chyczewski, T. S., Lindau, J. W., Gibeling, H. J., ... & Govindan, T. R. (2000). A preconditioned Navier–Stokes method for two-phase flows with application to cavitation prediction. *Computers & Fluids*, 29(8), 849-875.
- [66] Singhal, A. K., Athavale, M. M., Li, H., & Jiang, Y. (2002). Mathematical basis and validation of the full cavitation model. *Journal of Fluids Engineering*, 124(3), 617–624.
- [67] Schnerr, G. H., & Sauer, J. (2001, May). Physical and numerical modeling of unsteady cavitation dynamics. In *Fourth international conference on multiphase flow* (Vol. 1). ICMF New Orleans.
- [68] Geng, L., Chen, J., Torre, O. D. L., & Escaler, X. (2020). Numerical Simulation of Cavitation Erosion Aggressiveness Induced by Unsteady Cloud Cavitation. *Applied Sciences*, 10(15), 5184.
- [69] Hsiao, C. T., Jayaprakash, A., Kapahi, A., Choi, J. K., & Chahine, G. L. (2014). Modelling of

- material pitting from cavitation bubble collapse. *J. Fluid Mech*, 755(9), 142-175.
- [70] Paquette, Y. (2017). *Interaction Fluide-Structure et Érosion de Cavitation* (Doctoral dissertation).
- [71] Fivel, M., Franc, J. P., & Chandra Roy, S. (2015). Towards numerical prediction of cavitation erosion. *Interface Focus*, 5(5), 20150013.
- [72] Roy, S. C., Franc, J. P., Pellone, C., & Fivel, M. (2015). Determination of cavitation load spectra—Part 1: Static finite element approach. *Wear*, 344, 110-119.
- [73] Roy, S. C., Franc, J. P., Ranc, N., & Fivel, M. (2015). Determination of cavitation load spectra—Part 2: Dynamic finite element approach. *Wear*, 344, 120-129.
- [74] Patella, R. F., Choffat, T., Reboud, J. L., & Archer, A. (2013). Mass loss simulation in cavitation erosion: Fatigue criterion approach. *Wear*, 300(1-2), 205-215.
- [75] Ochiai, N., Iga, Y., Nohmi, M., & Ikohagi, T. (2010). Numerical prediction of cavitation erosion intensity in cavitating flows around a Clark Y 11.7% hydrofoil. *Journal of Fluid Science and Technology*, 5(3), 416-431.
- [76] Wang, H., & Zhu, B. (2010). Numerical prediction of impact force in cavitating flows. *Journal of fluids engineering*, 132(10).
- [77] Schnerr, G. H., Sezal, I. H., & Schmidt, S. J. (2008). Numerical investigation of three-dimensional cloud cavitation with special emphasis on collapse induced shock dynamics. *Physics of Fluids*, 20(4), 040703.
- [78] Mihatsch, M. S., Schmidt, S. J., & Adams, N. A. (2015). Cavitation erosion prediction based on analysis of flow dynamics and impact load spectra. *Physics of Fluids*, 27(10), 103302.
- [79] Blume, M., & Skoda, R. (2019). 3D flow simulation of a circular leading edge hydrofoil and assessment of cavitation erosion by the statistical evaluation of void collapses and cavitation structures. *Wear*, 428, 457-469.
- [80] Fortes-Patella, R.; Reboud, J.L.; Briancon-Marjollet, L. (2004, May). A phenomenological and numerical model for scaling the flow aggressiveness in cavitation erosion. In *Proceedings of the EROCAV Workshop*, Val de Reuil, France.
- [81] Patella, R.F.; Archer, A.; Flageul, C. (2012, August). Numerical and experimental investigations on cavitation erosion. In *Proceeding of the 26th IAHR Symposium on Hydraulic Machinery and Systems*, Beijing, China.
- [82] Nohmi, M.; Ikohagi, T.; Iga, Y. (2008, August). Numerical Prediction Method of Cavitation Erosion. In *Proceedings of the ASME 2008 Fluids Engineering Division Summer*, Jacksonville, FL, USA.
- [83] Li, Z.R.; Pourquie, M.; van Terwisga, T. (2014). Assessment of cavitation erosion with a URANS method. *Trans. ASME J. Fluids Eng.* 136, 041101.
- [84] Koukouvini, P.; Bergeles, G.; Gavaises, M. (2015). A cavitation aggressiveness index within the Reynolds averaged Navier Stokes methodology for cavitating flows. *J. Hydrodyn.* 27, 579–586.
- [85] Ponkratov, D.; Caldas, A. (2015, June). Prediction of Cavitation Erosion by Detached Eddy Simulation (DES) and its Validation against Model and Ship Scale Results. In *Proceeding of the 4th International Symposium on Marine Propulsors*, Austin, TX, USA.

- [86] Dular, M.; Coutier-Delgosha, O. (2009). Numerical modelling of cavitation erosion. *Int. J. Numer. Methods Fluids*. 61, 1388–1410.
- [87] Peters, A.; Sagar, H.; Lantermann, U.; el Moctar, O. (2015). Numerical modelling and prediction of cavitation erosion. *Wear*, 338, 189–201.
- [88] Davoudabadi, P. (2012). The Most Accurate and Advanced Turbulence Capabilities. In *Confidence by Design Workshop Chicago, IL, June (Vol. 14)*.
- [89] Coutier-Delgosha, O., Fortes-Patella, R., & Reboud, J. L. (2003). Evaluation of the turbulence model influence on the numerical simulations of unsteady cavitation. *J. Fluids Eng.*, 125(1), 38-45.
- [90] Melissaris, T.; Bulten, N.; van Terwisga, T.J.C. (2018, May). On Cavitation Aggressiveness and Cavitation Erosion on Marine Propellers using a URANS Method. In *Proceeding of the 10th International Symposium on Cavitation, Baltimore, MD, USA*.
- [91] Carrat, J.B.; Fortes-Patella, R.; Franc, J.P. (2017, August). Assessment of cavitating flow aggressiveness on a hydrofoil: Experimental and numerical approaches. In *Proceedings of the ASME 2017 Fluids Engineering Division Summer Meeting, Waikoloa, HI, USA*.
- [92] Leclercq, C.; Archer, A.; Fortes-Patella, R.; Cerru, F. (2017). Numerical cavitation intensity on a hydrofoil for 3D homogeneous unsteady viscous flows. *Int. J. Fluid Mach. Syst.* 10, 254–263.
- [93] Schenke, S.; van Terwisga, T.J. (2019). An energy conservative method to predict the erosive aggressiveness of collapsing cavitating structures and cavitating flows from numerical simulations. *Int. J. Multiph. Flow*, 111, 200–218.
- [94] Boussinesq, J. (1877). *Essai sur la theorie des eaux courantes*. *Mem. Presents divers savants Acad. Sci. Inst. Fr.*, 23, 1-680.
- [95] Launder, B. E., & Spalding, D. B. (1972). The numerical computation of turbulent flows. In *Numerical prediction of flow, heat transfer, turbulence and combustion (pp. 96-116)*. Pergamon.
- [96] ANSYS. (2015). Release 16.2, help system, CFX theory guide. Pittsburgh: ANSYS, Inc.
- [97] Yakhot, V., & Orszag, S. A. (1986). Renormalization group analysis of turbulence. I. Basic theory. *Journal of scientific computing*, 1(1), 3-51.
- [98] Wilcox, D. C. (1988). Multiscale model for turbulent flows. *AIAA journal*, 26(11), 1311-1320.
- [99] Menter, F. R. (1993, July). Multiscale model for turbulent flows. In *24th fluid dynamics conference*. American Institute of Aeronautics and Astronautics (Vol. 30, No. 4, pp. 198-214).
- [100] Leclercq, C.; Archer, A.; Fortes-Patella, R. (2016, July) Numerical investigations on cavitation intensity for 3d homogeneous unsteady viscous flows. In *Proceeding of the 28th IAHR Symposium on Hydraulic Machinery and Systems, Grenoble, France*.
- [101] Geng, L., & Escaler, X. (2020). Assessment of RANS turbulence models and Zwart cavitation model empirical coefficients for the simulation of unsteady cloud cavitation. *Engineering Applications of Computational Fluid Mechanics*, 14(1), 151-167.
- [102] Geng, L., Chen, J., & Escaler, X. (2020). Improvement of cavitation mass transfer modeling by including Rayleigh-Plesset equation second order term. *European Journal of Mechanics-B/Fluids*. 84, 313-324.

References

- [103] Geng, L., Chen, J., Torre, O. D. L., & Escaler, X. (2020). Numerical Simulation of Cavitation Erosion Aggressiveness Induced by Unsteady Cloud Cavitation. *Applied Sciences*, 10(15), 5184.
- [104] Fröhlich, J., & Von Terzi, D. (2008). Hybrid LES/RANS methods for the simulation of turbulent flows. *Progress in Aerospace Sciences*, 44(5), 349-377.

Annexes

Annex A

Assessment of RANS turbulence models and Zwart cavitation model empirical coefficients for the simulation of unsteady cloud cavitation


Authors:

Linlin Geng & Xavier Escaler*

Article published in:

Engineering Applications of Computational Fluid Mechanics, 2019

Assessment of RANS turbulence models and Zwart cavitation model empirical coefficients for the simulation of unsteady cloud cavitation

Linlin Geng and Xavier Escaler 

Center for Industrial Diagnostics and Fluid Dynamics (CDIF), Universitat Politècnica de Catalunya-BarcelonaTech (UPC), Barcelona, Spain

ABSTRACT

The numerical simulation of unsteady cavitation flows is sensitive to the selected models and associated parameters. Consequently, three Reynolds Average Navier-Stokes (RANS) turbulence models and the Zwart cavitation model were selected to assess their performance for the simulation of cloud cavitation on 2D hydrofoils. The experimental cavitation tests from a NACA65012 hydrofoil at different hydrodynamic conditions were used as a reference to tune the modeling parameters and the experimental tests from a NACA0015 were finally used to validate them. The effects of near wall grid refinement, time step, iterations and mesh elements were also investigated. The results indicate that the Shear Stress Transport (SST) model is sensitive to near wall grid resolution which should be fine enough. Moreover, the cavitation morphology and dynamic behavior are sensitive to the selection of the Zwart empirical vaporization, F_v , and condensation, F_c , coefficients. Therefore, a multiple linear regression approach with the single objective of predicting the shedding frequency was carried out that permitted to find the range of coefficient values giving the most accurate results. In addition, it was observed that they provided a better prediction of the vapor volume fraction and of the instantaneous pressure pulse generated by the main cloud cavity collapse.

ARTICLE HISTORY

Received 29 May 2019
Accepted 12 November 2019

KEYWORDS

Cloud cavitation; turbulence model; Zwart model; near wall grid; shedding process; 2D hydrofoil

1. Introduction

Cavitation is a topic of concern in the design and operation of a wide variety of hydraulic machinery and systems due to its negative effects like erosion, noise, vibrations and performance drop. Many research has been focused on the numerical simulation of the steady properties of the cavitation forms appearing for example in water jet nozzles (Chen, Hu, & Zhang, 2019), hydraulic turbines (Ayli, Celebioglu, & Aradag, 2016) and valves (Yuan, Song, & Liu, 2019). Broadly speaking, Computational Fluid Dynamic (CFD) models are becoming an indispensable tool to generate precise flow prediction and optimum design in many practical problems as demonstrated by recent works in very diverse disciplines such as architectural fields (Mou, He, Zhao & Chau, 2017), diesel engines (Akbarian, et al. 2018), heat exchangers (Ramezanizadeh, Nazari, Ahmadi & Chau, 2019), nanofluids (Ghalandari, Koohshahi, Mohamadian, Shamshirband & Chau, 2019), and in combination with machine learning methods (Mosavi, Shamshirband, Salwana, Chau & Tah, 2019).

More specifically, cavitation flows are turbulent and unsteady which make them complex fluid mechanics problems. For example, one of the most aggressive forms

of cavitation is the cloud cavitation that forms on hydrofoils. This powerful and unstable type of cavitation generates strong vibrations on the hydrofoil that are prone to excite the structure and to erode the solid surface. Therefore, the unstable behavior of cavitation must be predicted during the design stage to guarantee a safe operation of many hydraulic machinery such as turbines and pumps. For that, accurate numerical simulations with CFD are needed which depend both on the turbulence and the cavitation models being used.

Many works have addressed the significant influence of the turbulence model on the simulation of cavitation flows. For example, Bensow (2011) simulated unsteady cavitation on the Delft Twist11 foil with Large Eddy Simulation (LES), Detached Eddy Simulation (DES), and Reynolds-Averaged Navier-Stokes (RANS) turbulence models. He showed that the RANS models failed to capture the unsteady behavior unless the Reboud's correction (Reboud, Stutz, & Coutier, 1998) was used. This correction reduces the turbulent viscosity in the mixture of water and vapor by taking into account the compressibility effects. He also demonstrated that LES and DES can predict details of the cavitation dynamic behavior like the shedding frequency. Kim

CONTACT Xavier Escaler  xavier.escaler@upc.edu

(2009) obtained a similar conclusion by simulating partial cavitation on a NACA0015 hydrofoil. Similarly, Pendar and Roohi (2016) and Roohi, Pendar and Rahimi (2016) compared the RANS Shear Stress Transport (SST) and the LES models for cavitating and supercavitating flows, and they stated that LES provided the most accurate solutions. Kinzel, Lindau, Peltier, Kunz and Sankaran (2007) applied the DES and the RANS standard $k-\varepsilon$ models to simulate the flow around a ventilated body and an ogive. They pointed out that DES can capture a much broader spectrum of the turbulent scales and the cavity dynamics, as well as predict better a range of cavitating flows. Sedlar, Ji, Kratky, Rebok and Huzlik (2016) employed LES, DES and Scale-Adaptive Simulation (SAS) to simulate the unsteady cavitating flow around a NACA2412 hydrofoil. They found that SAS and DES can predict better the dominant frequency of the cavity oscillation, which is overestimated by LES. Nevertheless, LES appeared to provide the best description of the vortex structures.

In spite of the superiority that the scale-resolving approaches (LES and DES) have demonstrated, it has been stated that these approaches become impractical in a fast-paced industrial context due to the significant requirements in computational capacity. Therefore, RANS models still remain the most widely used approach in industrial CFD for hydraulic machinery and systems. However, conclusive results regarding the influence of different RANS models on the cavitation simulation is quite limited. For instance, Goncalves (2011) used four different RANS models to simulate the cavitating flow in a Venturi test section. The numerical results showed that the SST model provided the best agreement with the experimental data.

Regarding the influence of the cavitation models, there are various computational approaches to simulate cavitation flows with different levels of complexity. The two-phase flow is often treated as a homogeneous phase mixture of vapor and water consisting of a single fluid with varying density. Two strategies can be used to compute the density field which are based on either an equation of state (EOS) or on a volume fraction transport equation.

For example, Goncalves (2011) used a barotropic equation of state (EOS) that couples density directly with pressure to close the system. However, this model cannot take into account mass exchange and thermal transfer in the cavitation. Furthermore, it cannot capture all the vorticity production that is a fundamental mechanism at the cavity closure region (Gopalan and Katz, 2000; Senocak and Shyy 2002). Mani, Cervone and Hickey (2017) also demonstrated that this strategy is very sensitive to the turbulent closure model. Similarly, several

authors have found that the morphology of the cavity is highly affected by the value of the minimum speed of sound (Pascarella, Salvatore & Ciucci, 2003; Gonçalves & Patella, 2009; Hejranfar, Ezzatneshan & Fattah-Hesari, 2015).

The approach based on the transport equation models (TEM) for the volume fraction including a cavitation source term permits to calculate the mass transfer between the vapor and water phases (Utturkar, Wu, Wang & Shyy, 2005). Several TEMs have been proposed which have been set as the default option in popular CFD software. For instance, the Zwart model (Zwart, Gerber, & Belamri, 2004) and the Kunz model (Kunz et al., 2000) are the native cavitation models in CFX[®] and OPENFOAM[®], respectively. Meanwhile, Fluent[®] has adopted the Singhal cavitation model (Singhal, Athavale, Li & Jiang, 2002). However, the main drawback of these TEMs is that they are based on different source terms along with empirical constants. Besides, some ill-posed formulations have been detected in the works of several authors. For example, Pendar and Roohi (2016), Roohi, Pendar and Rahimi (2016), Senocak and Shyy (2002) and Utturkar, Wu, Wang and Shyy (2005) define the Kunz model mass transfer rate with inconsistent dimensions. Moreover, Senocak and Shyy (2002) and Utturkar, Wu, Wang and Shyy (2005) also propose a different expression for the condensation term of the Singhal model using the product of water and vapor densities instead of the square value of the water density. Therefore, attention should be paid to carefully check the mathematical definitions of the cavitation models implemented by the researchers into their CFD codes in comparison with the original models being used as reference.

The TEMs' empirical constants are necessary to tune the evaporation and condensation rates between the two phases which are not symmetric. Actually, the values for such empirical coefficients are in some way arbitrary and generally based on the studies carried out by the model's authors. Consequently, the use of the assumed default values could result in uncertain results for some cases. Therefore, it is crucial to assess the validity and the influence of these coefficients on the numerical results. In this sense, Vaidyanathan, Senocak, Wu and Shyy (2003) optimized the coefficients of the Kunz model based on the response surface method, and identified the best combination for attached cavities around a hemispherical projectile (Rouse & McNown, 1948) and the modified NACA66(MOD) hydrofoil (Shen & Dimotakis, 1989) at different cavitation numbers. Morgut, Nobile and Biluš (2011) and Bilus, Morgut and Nobile (2013) tuned the empirical coefficients of three different cavitation models (Zwart, Kunz and Singhal) with an optimization strategy based on sheet cavitation experiments carried out around

Table 1. Summary of some of the recommended empirical coefficients for different cavitation models.

Authors	Cavitation pattern	Tested geometry	Cavitation model	Recommended values	
				Vaporization	Condensation
Vaidyanathan et al. (2003)	Sheet	Projectile & NACA66(MOD)	Kunz	800,000	40,000
Morgut et al. (2011) and Bilus et al. (2013)	Sheet	NACA66(MOD) & NACA0009	Kunz	4100	455
			Zwart	300	0.03
			Singhal	0.4	$2.3E^{-4}$
			Zwart	22–288	0.0013–0.0248
Tseng and Wang (2014)	Sheet and cloud	Projectile		2–29	0.00013–0.0025
		NACA66(MOD)		8–104	0.00047–0.0090
		Clark Y			

a NACA0009 hydrofoil by Dupont (1993) and around a NACA66(MOD) hydrofoil by Shen and Dimotakis (1989). The results demonstrated that the three cavitation models could provide similar levels of accuracy if optimized empirical coefficients were used. However, for the case of unsteady partial cavitation (sheet or cloud type), they also noted that further work was required to find out the adequate coefficients. Tseng and Wang (2014) modified the coefficients of the Zwart model into a dimensionless form, and determined a coefficient range also based on the experiments of a hemispherical projectile (Rouse & McNown, 1948) and of the NACA66(MOD) hydrofoil (Shen & Dimotakis, 1989), as well as the Clark Y hydrofoil (Wang, Senocak, Shyy, Ikohagi & Cao, 2001). They stated that their proposed range of values improved the generality and reduced the sensitivity of the numerical results to the cavitation model. As an example, Table 1 summarizes some research works with their recommended values for different cavitation models. Note here that the coefficients recommended by Tseng and Wang (2014) were obtained based on particular dimensionless coefficients.

The recommended coefficients in Table 1 show that completely different values were proposed for the Kunz and Zwart models by different authors, although similar cavitation patterns were investigated by all of them. One possible reason for such discrepancies are that the turbulence models, which have a significant effect on the numerical results, are not aligned between them.

Based on the current state of art, the present work has been devoted firstly to investigate systematically and with detail the performance of different RANS models by comparing the simulated unsteady cavitation flows with the experimental results available under different operation conditions. Moreover, the sensitivity of each turbulence model to various numerical parameters has also been evaluated. Next, the influence of the empirical coefficients of the Zwart cavitation model on the simulation results of cloud cavitation dimensions, morphology, dynamic behavior and collapse process have been analyzed in detail to determine a range of optimal values to be used. It has to be noted that,

unlike the previous works summarized in Table 1 in which most of the investigations have been based on steady state simulations, in our study we have focused on the shedding process of the cloud cavitation around hydrofoils.

2. Experiments and numerical methods

2.1. Experimental results

The experimental investigations taken as a reference for validation purposes of our numerical results were carried out by Escaler, Farhat, Egusquiza and Avellan (2007) and Couty (2002) to determine the dynamic behavior and the intensity of erosive partial cavitation on hydrofoils. In particular, unstable cloud cavitation was tested in the High Speed Cavitation Tunnel at EPFL for various free stream velocities, U_{inf} , on a NACA65012 hydrofoil. The tunnel test section was rectangular with dimensions $150 \times 150 \times 750 \text{ mm}^3$. The hydrofoil had a chord length, c , of 100 mm and it was fixed with an incidence angle, α , of 6° .

Unsteady cloud cavitation on the hydrofoil suction side was generated by adjusting the inlet pressure, P_{in} . The values of the corresponding cavitation numbers, σ , defined by Eq. 1 are indicated in Table 2 for 8 testing conditions that comprised free stream velocities, U_{inf} , ranging from 15 to 30 m/s and two maximum cavity lengths, l , of 20% and 40% of the chord. The shedding frequency, f , was obtained by amplitude demodulation of the

Table 2. Experimental conditions, relative maximum cavity lengths and shedding frequencies (Escaler et al, 2007).

Case	α [°]	l/c [–]	U_{inf} [m/s]	σ [–]	f [Hz]	St [–]
1	6	20	15	1.83	189.2	0.25
2	6	20	20	1.85	250.2	0.25
3	6	20	25	1.87	387.6	0.31
4	6	20	30	1.90	419.6	0.28
5	6	40	15	1.55	96.1	0.26
6	6	40	20	1.58	132.8	0.27
7	6	40	25	1.60	175.5	0.28
8	6	40	30	1.62	225.8	0.30

measured cavitation induced vibration. Then, the corresponding Strouhal number was determined according to Eq. 2.

$$\sigma = \frac{P_{in} - P_v}{0.5\rho_l U_{inf}^2} \quad (1)$$

$$St = \frac{fl}{U_{inf}} \quad (2)$$

2.2. Numerical model

Based on the homogeneous mixture flow assumption, the two phases of a turbulent cavitation flow, vapor and water, are assumed to have velocity and pressure equilibrium between them. Thus, the governing equations for the mixture quantities are the mass conservation equation (Eq. 3) and the momentum conservation equation (Eq. 4):

$$\frac{\partial \rho_m}{\partial t} + \nabla \cdot (\rho_m u) = 0 \quad (3)$$

$$\begin{aligned} \frac{\partial (\rho_m u)}{\partial t} + \nabla \cdot (\rho_m uu) = -\nabla p \\ + \nabla \cdot \left[(\mu_m + \mu_t)(\nabla u + u\nabla - \frac{2}{3}\nabla \cdot u) \right] \end{aligned} \quad (4)$$

where u and p are the mixture flow velocity and pressure, t is the time and μ_t is the turbulent eddy viscosity. The mixture flow dynamic viscosity, μ_m , and density, ρ_m , are defined as by Eqs. 5 and 6:

$$\mu_m = \alpha_v \mu_v + (1 - \alpha_v) \mu_l \quad (5)$$

$$\rho_m = \alpha_v \rho_v + (1 - \alpha_v) \rho_l \quad (6)$$

where ρ_v and μ_v are the vapor density and dynamic viscosity, respectively, ρ_l and μ_l are the water density and dynamic viscosity, respectively, and α_v is the vapor volume fraction that is defined as the ratio of the vapor volume to the cell volume and obtained from an additional vapor mass conservation equation (Eq. 7):

$$\frac{\partial (\alpha_v \rho_v)}{\partial t} + \nabla \cdot (\alpha_v \rho_v u) = R_e - R_c \quad (7)$$

where R_e and R_c are the evaporation and condensation source terms, respectively, that account for the mass transfer rate between the water and vapor phases.

The mass transfer rate calculation can be developed based on the dynamics of a spherical bubble in an infinite body of incompressible fluid governed by the Rayleigh-Plesset equation (Brennen, 1995) which is defined

as Eq. 8:

$$\begin{aligned} \frac{p_v(T_\infty) - p_\infty(t)}{\rho_l} + \frac{p_v(T_B) - p_\infty(T_\infty)}{\rho_l} \\ + \frac{P_{G0}}{\rho_l} \left(\frac{T_B}{T_\infty} \right) \left(\frac{R_0}{R} \right)^3 \\ = R \frac{d^2 R}{dt^2} + \frac{3}{2} \left(\frac{dR}{dt} \right)^2 + \frac{4\mu_l}{R\rho_l} \frac{dR}{dt} + \frac{2S}{R\rho_l} \end{aligned} \quad (8)$$

where R is the bubble radius, R_0 is the initial bubble radius, S is the liquid surface tension, P_{G0} is the pressure of non-condensable gas, P_v is the saturated pressure, T_∞ and P_∞ are the temperature and the pressure at infinity, respectively, and T_B is the temperature within the bubble. On the left hand side of Eq. 8, the first term is the driving force determined by the conditions far from the bubble, the second term refers to the thermal effects which will play an important role when the temperature difference is large enough, and the third term refers to the non-condensable gas effect. On the right hand side of Eq. 8, the last two terms consider the influence of viscosity and surface tension, respectively. Since the bubble's growth and collapse are generally considered to be isothermal processes, thus Eq. 8 can be simplified to:

$$\begin{aligned} R \frac{d^2 R}{dt^2} + \frac{3}{2} \left(\frac{dR}{dt} \right)^2 = \frac{p_v - p_\infty}{\rho_l} + \frac{P_{G0}}{\rho_l} \left(\frac{R_0}{R} \right)^3 \\ - \frac{4\mu_l}{R\rho_l} \frac{dR}{dt} - \frac{2S}{R\rho_l} \end{aligned} \quad (9)$$

Since in most cases the inertial forces are dominant, viscosity and surface tension do not play a significant role and the effects of non-condensable gas are neglected, Eq. 9 is further simplified to:

$$\frac{dR}{dt} = \sqrt{\frac{2}{3} \frac{p_v - p_\infty}{\rho_l}} \quad (10)$$

This simplified form of the Rayleigh-Plesset equation has been used to develop the cavitation models by Singhal (Singhal et al., 2002), Sauer (Schnerr and Sauer, 2001) and Zwart (Zwart et al., 2004) based on the relation between the bubble diameter and the vapor volume or mass fractions. Nevertheless, its use may affect the model accuracy if, for example, the second temporal derivative of bubble radius is ignored because then the initial bubble growth rate and the bubble collapse rate will be affected. In a similar way, the thermodynamic effect should also be taken into account because it will modify the pressure and temperature distribution between the bubble and the outer liquid and thus the mass transfer rate. Therefore, in order to predict the cavitation phenomenon more accurately, some empirical constants and other parameters such as

the vapor bubble radius in the Zwart model, the non-condensable gas fraction in the Singhal model and the number of nuclei per liquid volume in the Sauer model need to be determined and tuned for each flow condition. More specifically, these cavitation models must also be significantly improved for some applications like cavitation in cryogenic liquids, in strongly viscous liquids and in flows with high gas content.

In particular, for the Zwart model, the vaporization and condensation mass transfer rates are expressed as:

$$R_e = F_v \frac{3\alpha_{nuc}(1 - \alpha_v)\rho_v}{R_B} \sqrt{\frac{2}{3} \frac{P_v - P}{\rho_l}} \quad (P \leq P_v) \quad (11)$$

$$R_c = F_c \frac{3\alpha_v\rho_v}{R_B} \sqrt{\frac{2}{3} \frac{P - P_v}{\rho_l}} \quad (P \geq P_v) \quad (12)$$

where R_B is the vapor bubble radius, α_{nuc} is the nucleation site volume fraction, P_v is the saturated water vapor pressure, p is the local fluid pressure, and F_v and F_c are the empirical coefficients for vaporization and condensation, respectively. The default model constants in ANSYS CFX[®] v16.2 software are $R_B = 10^{-6}$ m, $\alpha_{nuc} = 0.0005$, $F_v = 50$ and $F_c = 0.01$.

The RANS models used to calculate μ_t are able to reproduce the unsteady cavitation behavior if the compressibility effect of the mixture is taken into account using the method proposed by Reboud et al. (1998). This correction has been proved to reproduce the cloud cavitation shedding process because it is able to reduce the turbulent eddy viscosity in the mixture. Thus, it has been implemented in our simulations by introducing the function $f(\rho)$ defined with Eq. 13:

$$f(\rho) = \rho_v + \left(\frac{\rho_v - \rho_m}{\rho_v - \rho_l} \right)^n (\rho_l - \rho_v) \quad (13)$$

where the exponent n is recommended to have a value higher than 1. In our study, we have selected $n = 10$ after performing a sensitivity analysis.

A brief mathematical description of the RANS two-equation models used in our simulations is given as follows, but more detailed formulation can be found in the CFX help manual (ANSYS, 2015). The k - ε model calculates μ_t from the turbulent kinetic energy, k , and its dissipation rate, ε , with Eq. 14:

$$\mu_t = f(\rho)c_\mu \frac{k^2}{\varepsilon} \quad (14)$$

where $c_\mu = 0.09$. The RNG model is based on renormalization group analysis of the Navier-Stokes equations. The transport equations for turbulence generation and dissipation are the same as those for the k - ε model

(Eq. 10), but the model constant $c_\mu = 0.085$. Finally, the SST model, which improves the accuracy of prediction of the onset and the amount of flow separation under adverse pressure gradients, assumes that μ_t is linked to k and to the turbulent frequency, ω , via Eq. 15:

$$\mu_t = \frac{f(\rho)a_1k}{\max(a_1\omega, SF_2)} \quad (15)$$

where F_2 is a function that equals 1 for boundary layer flows and 0 for free shear layers, S is an invariant measure of the strain rate and $a_1 = 0.31$.

2.3. Solution strategy

The computational domain and the selected coordinate system have been implemented in ANSYS CFX[®] version 16.2 based on the tunnel geometry and they are schematically plotted in Figure 1. The whole computational domain extends 2 chords upstream the hydrofoil leading edge and 4.5 chords downstream the trailing edge, and the thickness of the computational domain is 1 mm.

The inlet boundary setup was defined with the corresponding normal velocity equal to U_{inf} , a turbulent intensity of 1% and a water and vapor volume fractions equal to 1 and 0, respectively. The average static pressure was specified at the outlet boundary. The corresponding pressure value was obtained from preliminary simulations without the cavitation model activated. For that, the inlet boundary condition was defined as total pressure, with the static pressure being calculated according to the cavitation number, and the outlet boundary was defined as total mass flow rate. After convergence, the average pressure at outlet boundary was calculated. The obtained values for each case were then used as the outlet boundary condition to simulate cavitation. A no-slip wall condition was set for the top, bottom and hydrofoil surfaces. On the two lateral faces of the fluid domain, a symmetry condition was setup to simulate a 2D flow. Moreover, the vapor saturation pressure, the density and the dynamic viscosity of water and vapor were adjusted based on the experiment temperature of 17°C ($P_v = 2000$ Pa, $\rho_v = 0.01389$ kg/m³, $\mu_v = 9.6 \text{ E}^{-3}$ kg/m·s, $\rho_l = 998.7$ kg/m³, $\mu_l = 0.0011$ kg/m·s).

The pressure-velocity direct coupling method was used to solve the governing equations. The high resolution scheme was used for the convection terms. The second order implicit time scheme was used for the transient term. Several successive iterations were set within each physical time step. A very small residual criterion of 10^{-8} and a large iterative number were set to march the solution towards convergence in every time step. To

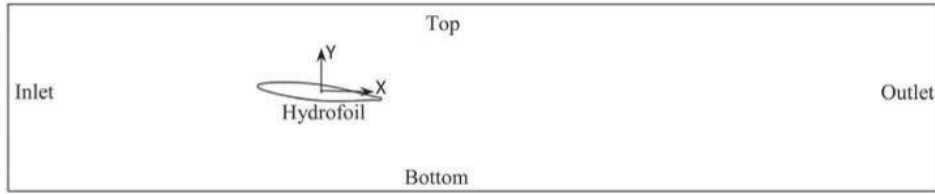


Figure 1. 2D computational domain with named boundaries and coordinate system.

accelerate convergence, the transient simulations were run from previous steady state simulation results.

3. Numerical verification and validation

Some CFD uncertainties might be due to numerical and modeling errors caused by time and space discretization and by incomplete iterative and grid convergences. The y^+ has been defined with Eq. 16.

$$y^+ = \frac{\sqrt{\tau_w/\rho}\Delta y}{\nu} \quad (16)$$

where τ_w is the wall shear stress, ν is kinematic viscosity, Δy denotes is the distance between the first and second grid points off the wall. The effects of y^+ , time step, number of iterations and number of mesh elements have been evaluated only for the cavitation conditions corresponding to case 8 in Table 2. The hydrodynamic conditions of case 8 generate the most aggressive form of cloud cavitation in terms of erosion and vibrations. On the other hand, the modeling errors coming from the assumptions and approximations of the RANS turbulence model and the Zwart cavitation model have been assessed for all the cases in Table 2.

3.1. Mesh convergence study

A mesh convergence study was performed according to the Grid Convergence Method (GCI) provided by Fluids Engineering Division of ASME (Ismail et al., 2008) and taking into account that in CFX different turbulence models use different wall treatments. The SST model uses the so-called Automatic Wall Function that switches automatically from a typical wall function approach to a low-Re-number model by blending the wall value for ω between the logarithmic and the near wall formulation as the mesh is refined. Meanwhile, the $k-\varepsilon$ and the RNG $k-\varepsilon$ models use the so-called Scalable Wall Function in which y^+ is calculated as $y^+ = \max(y^+, 11.06)$. Therefore, these two turbulence models do not resolve the viscous sublayer and they directly use the logarithmic relation to compute the near wall velocity.

Several mesh resolutions were tested with the three turbulence models. For that, the meshing tool ANSYS

Table 3. Features of the three refinement levels for the two grids.

Grid 1	elements	y^+ max	y^+ mean	Grid 2	elements	y^+ max	y^+ mean
G1.1	60323	4.03	1.85	G2.1	53731	42.53	17.2
G1.2	29749	4.03	2.13	G2.2	26849	42.9	20.6
G1.3	14587	4.25	2.26	G2.3	13024	57.5	23.8

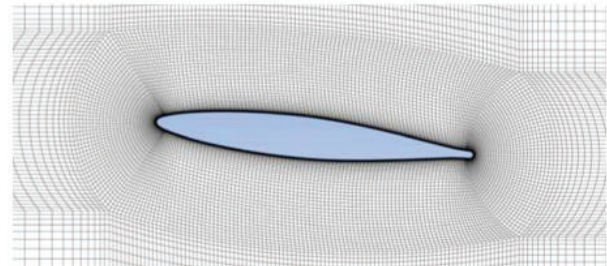


Figure 2. Mesh arrangement of grid G2.2.

ICEM[®] was used to create two structured meshes, named Grid1 and Grid2, with three different degrees of refinement as indicated in Table 3. All the meshes were built with similar topology and with the same recommended grid refinement factor $r = \sqrt{2}$. For Grid 1 meshes, the height of first layer was small enough so that the boundary layer could be solved with the low-Re-Number model. For Grid 2 meshes, the first layer of elements lied in the log-law region. As an example, Figure 2 shows the topology of G2.2 mesh with an O-grid around the hydrofoil embedded inside an H-grid.

The three turbulence models were applied to each grid to simulate case 8 from Table 2 corresponding to $U_{inf} = 30$ m/s without considering cavitation. The lift coefficient, C_L , defined by Eq. 17, where F_L represents the lift force, c is the chord length and s is the span length, was computed to obtain the value of the fine-grid convergence indexes (GCI_{21} and GCI_{32}) indicating whether calculations with additional grid refinement should be performed. Table 4 presents these indexes for each turbulence model and each mesh.

$$C_L = \frac{F_L}{0.5\rho_l U_{inf}^2 cs} \quad (17)$$

As shown in Table 4, the maximum GCI values for Grid 1 are 0.6% and 1.8% for the three turbulence models,

Table 4. Features of the different grids and numerical uncertainty evaluation based on the GCI indexes.

Turbulence model	Grid 1	C_L	GCI	Grid 2	C_L	GCI
SST	G1.1	0.845	$GCI_{21} = 0.6\%$	G2.1	0.809	$GCI_{21} = 9.7\%$
	G1.2	0.839	$GCI_{32} = 1.5\%$	G2.2	0.781	$GCI_{32} = 7\%$
	G1.3	0.826		G2.3	0.762	
$k-\varepsilon$	G1.1	0.802	$GCI_{21} = 0.5\%$	G2.1	0.818	$GCI_{21} = 0.002\%$
	G1.2	0.793	$GCI_{32} = 1.8\%$	G2.2	0.818	$GCI_{32} = 0.03\%$
	G1.3	0.763		G2.3	0.799	
RNG	G1.1	0.803	$GCI_{21} = 0.4\%$	G2.1	0.824	$GCI_{21} = 0.08\%$
	G1.2	0.795	$GCI_{32} = 1.7\%$	G2.2	0.821	$GCI_{32} = 0.5\%$
	G1.3	0.765		G2.3	0.803	

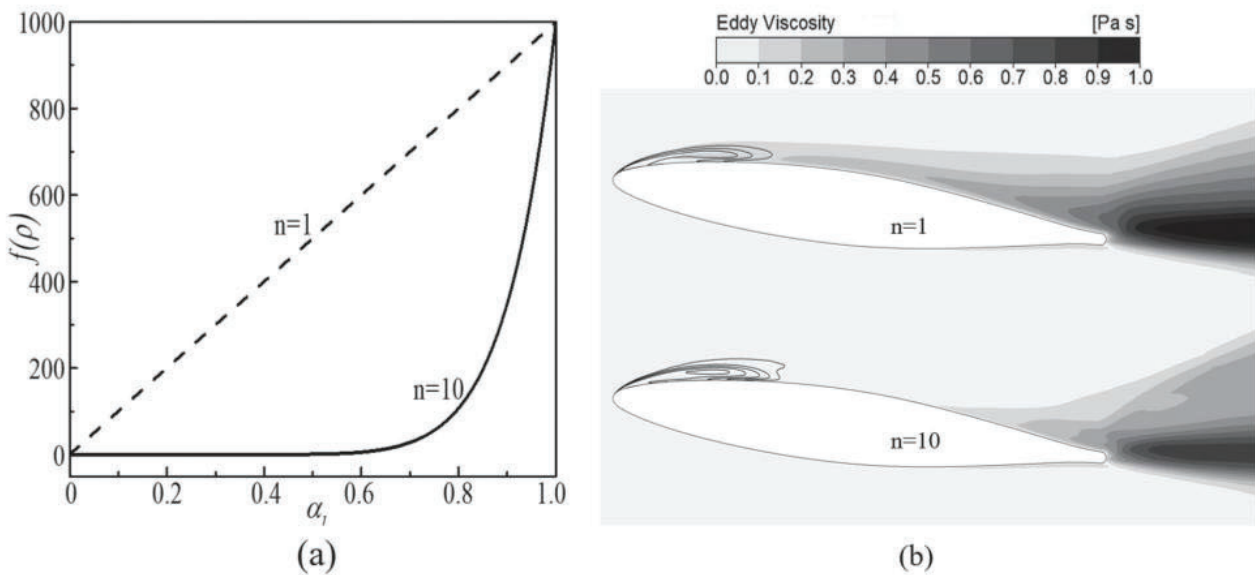
indicating that the solution is well within the asymptotic range. For Grid 2, the GCI values are smaller for the $k-\varepsilon$ and RNG models, while they are larger for the SST model reaching 9.7%. This is because the mesh resolution in Grid 2 is more consistent with the requirement of a scalable wall function. Based on these results, it was concluded that the medium grids G1.2 and G2.2 provided the necessary resolutions within the asymptotic range, and, considering the cost of simulation time, they were chosen for all the final simulations.

3.2. Reboud's correction for the turbulence models

To emphasize the importance of the Reboud's correction and the influence of its exponent value n , the SST turbulence model was selected to conduct the unsteady simulation for case 8 conditions with $n = 1$ (not recommended) and $n = 10$ (recommended). The value of n determines the rate of change of the modified effective density, $f(\rho)$,

with the water volume fraction, α_l , as shown in Figure 3a. For $n = 1$, the unstable behavior of the attached cavity is not correctly simulated and a quasi-steady behavior is predicted. However, a typical cloud cavitation behavior with a good shedding frequency and maximum cavity length is obtained with $n = 10$ as expected. The reason for this is the induced reduction of the eddy viscosity that is clearly overpredicted by the original turbulence model. In Figure 3b, the simulated mean vapor volume fraction and turbulent eddy viscosity obtained with $n = 1$ and $n = 10$ are plotted for comparison. It can be seen that, taking $n = 1$, very high eddy viscosity values are obtained in the cavity closure region which prevents the formation of the re-entrant jet. Whereas with $n = 10$, the eddy viscosity is almost zero on the hydrofoil extrados except the area close to the trailing edge thus allowing the formation of the re-entrant jet and reproducing the cavitation shedding process.

The evaluation of the turbulence models for cavitation simulation is necessary in the particular field of hydraulic machinery because the Reynolds numbers are very high and the losses induced by viscosity are not negligible. Nevertheless, it must be noted that in some cases the unsteady cloud cavitation behavior is mainly controlled by the inertial forces instead of the viscous forces. Consequently, inviscid solvers could also be used as demonstrated by the works of Budich, Neuner, Schmidt and Adams (2015) and Schenke and van Terwisga (2019) who modeled with good success the cavitation unsteady behavior over a sharp wedge and around a NACA0015 hydrofoil, respectively. They were able to predict the frequency of the shedding process, the re-entrant jet and

**Figure 3.** (a) Local modification of the mixture density with different values of the Reboud's correction exponent n ; (b) Averaged eddy viscosity contours predicted with $n = 1$ and $n = 10$.

the horse-shoe vortices. Thus, the application of inviscid solvers must be considered as a feasible alternative methodology in particular for inertia driven cavitating flows.

3.3. Sensitivity of the numerical parameters

In this section, a sensitivity analysis of the main parameters to simulate unsteady cavitation is presented based on case 8. In particular, attention has been given to y^+ ,

time step, number of iterations and number of mesh elements. For each computation, both the lift coefficient, C_L , and the total vapor volume within the computational domain, V_{cav} , during several cavitation cycles have been considered to assess the results. V_{cav} has been defined with Eq. 18:

$$V_{cav} = \sum_{i=1}^n \alpha_i V_i \tag{18}$$

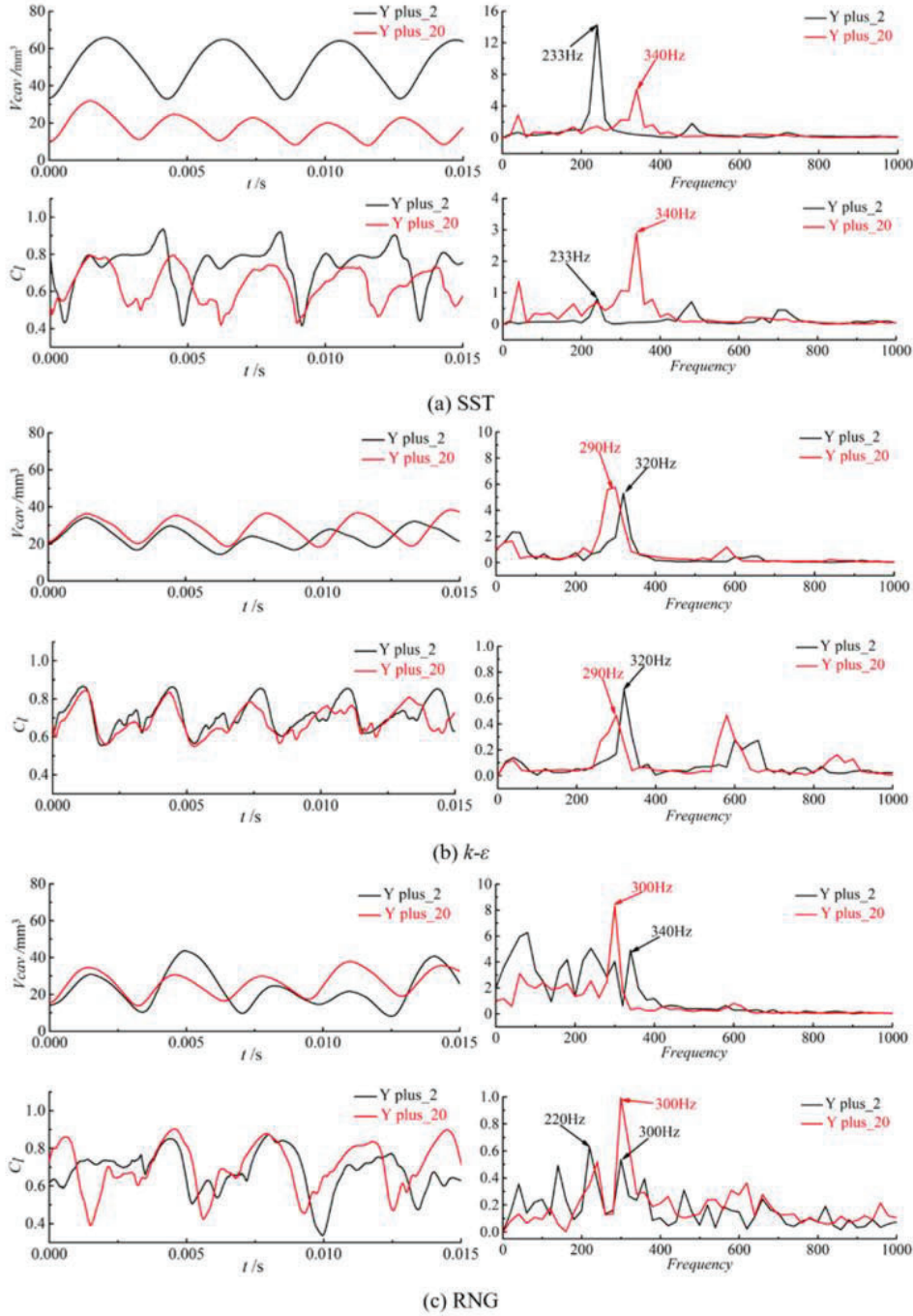


Figure 4. V_{cav} and C_L time evolution (left) and corresponding frequency content (right) as a function of y^+ for STT (a), $k-\epsilon$ (b) and RNG (c) turbulence models.

where n denotes the number of mesh elements, α_i is the vapor volume fraction within the element and V_i is the element volume. The simulated transient values of these two physical quantities have been compared between different model setups in the time and the frequency domains.

Mesh G1.2 with an average $y^+ = 2$ and mesh G2.2 with an average $y^+ = 20$ have been used to evaluate the influence of the near wall grid refinement on the numerical results for each turbulence model, as it can be seen on the shape of the time signals and their spectra plotted in Figure 4.

In Figure 4a, the results with the SST model show that V_{cav} is significantly higher with the finer mesh. The evolution of C_L over time also changes significantly depending on y^+ . The periodic frequency of the shedding process is of about 233 Hz for the finer mesh and of about 340 Hz for the coarser one, the former estimate being closer to the experimental one. Then, the influence of y^+ on the results predicted by the $k-\epsilon$ is not as significant as for those with the SST model as demonstrated by the similar results and frequency peaks with only a small difference of 30 Hz shown in Figure 4b. And finally for the RNG model, the shedding process is not well captured with the finer mesh as no clear frequency peak can be distinguished in the spectra in Figure 4c. Meanwhile, a dominant fluctuation is obtained around 300 Hz with the coarser mesh. In conclusion, the SST model appears to work well for smaller y^+ values. Meanwhile, the $k-\epsilon$ and the RNG models can only capture the cavitation periodic dynamic behavior for larger values of y^+ . Hence, mesh G1.2 was finally used with the SST model and mesh G2.2 was used with $k-\epsilon$ and RNG models.

Next, the numerical sensitivity to the rest of parameters -time step duration, number of iterations and number of mesh elements- was evaluated based on the calculated dominant frequency peak, f , for both C_L and V_{cav} results as indicated in Table 5. The last column represents the percent deviation of the frequency result obtained with the higher value of the sensitivity parameter relative to the result obtained with the lower value of the sensitivity parameter.

Two different time step durations were investigated with an approximate value of 1/100 and 1/200 times the measured shedding period in the experiment, respectively. As it can be seen, the influence on f is weak for all the turbulence models since the maximum error found is only around 3.4%. Based on this result, the time step for the rest of simulations was fixed to 0.00005 s. The influence of the number of iterations in every time step loop appears to be negligible for all the three turbulence models. The change of f is less than 2%. Therefore, a number of 20 iterations was considered sufficient in any case.

Table 5. Influence of time step, number of iterations and number of mesh elements on calculated f for each turbulence model.

Turbulence model	y^+ mean [-]	Time step [s]	number of iterations [-]	number of elements [-]	f [Hz]	f deviation [%]
Time step duration						
SST	2	0.00005	20	29749	233	-3.0
	2	0.00002	20	29749	240	
k-ε	20	0.00005	20	26849	290	3.4
	20	0.00002	20	26849	280	
RNG	20	0.00005	20	26849	300	0.0
	20	0.00002	20	26849	300	
Number of iterations						
SST	2	0.00005	20	29749	233	-0.9
	2	0.00005	50	29749	235	
k-ε	20	0.00005	20	26849	290	1.7
	20	0.00005	50	26849	285	
RNG	20	0.00005	20	26849	300	0.0
	20	0.00005	50	26849	300	
Number of mesh elements						
SST	2	0.00005	20	29749	233	2.6
	2	0.00005	20	101596	227	
k-ε	20	0.00005	20	26849	290	1.7
	20	0.00005	20	101596	285	
RNG	20	0.00005	20	26849	300	-1.7
	20	0.00005	20	101596	305	

To test the influence of the number of mesh elements, a new mesh with four times the original number of elements was built but with the same mesh topology and the same average y^+ . Based on the results presented in Table 5, the obtained f only suffers a slight change with less than 3% deviation. Thus, it was confirmed that the coarser meshes with less than 30,000 elements were suitable to carry out accurate predictions of the cavity dynamic behavior. In summary, and according to the slight effect of the checked numerical parameters, the finally selected values corresponded to those providing accurate numerical results and saving computational time and effort

3.4. Sensitivity of the dimension space

To investigate the effect of the number of computational domain dimensions, a 3D model was created according to the experimental configuration with a thickness of 150 mm corresponding to the tunnel test section and hydrofoil span wise size. A 3D mesh was created by extruding the 2D mesh G1.2 with 150 uniformly distributed elements in the cross direction Z, and hence nearly 4.5 million elements were needed to solve the problem. The same boundary conditions and numerical settings were fixed between 2D and 3D simulations, and no-slip wall conditions were used at the two sidewalls of the 3D domain instead of the symmetry conditions used for the 2D domain. The 3D cavitation simulation was only conducted with the SST turbulence model.

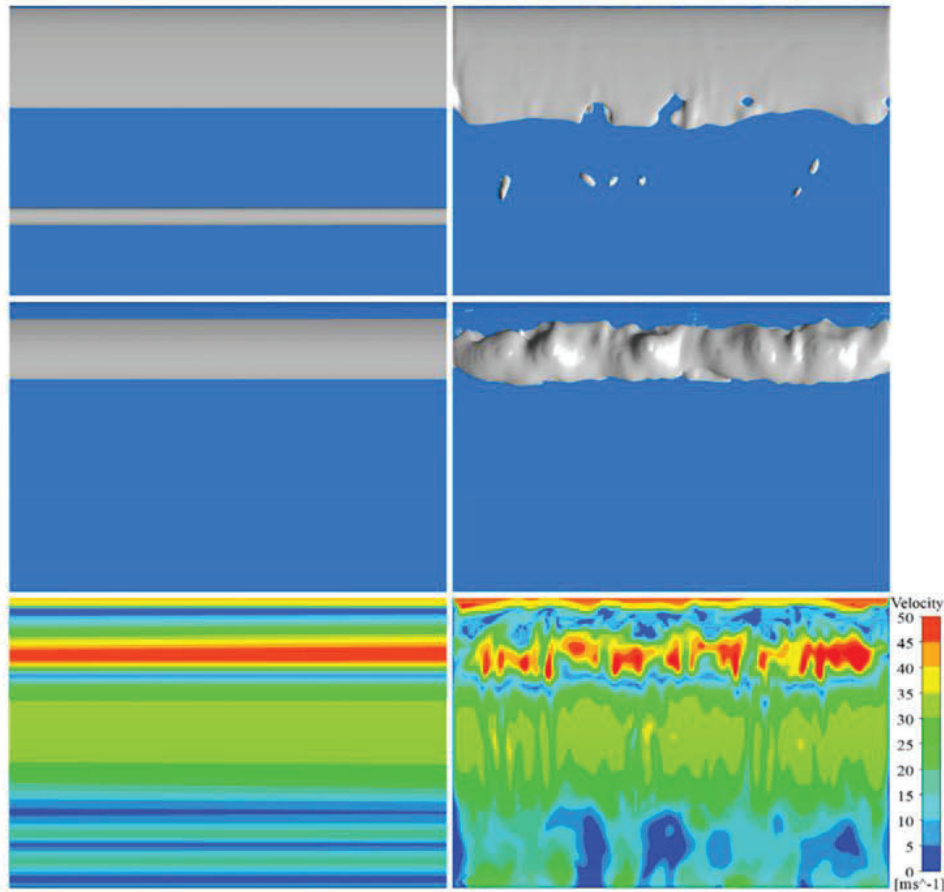


Figure 5. Comparison of 2D (left column) and 3D (right column) simulation results on the hydrofoil extrados. Isosurfaces of vapor volume fraction 0.2 at the instants of maximum cavity length (top) and of cavity break off (middle) and corresponding velocity distributions on a surface located at a distance 0.5 mm above the hydrofoil extrados at the break off instant (bottom).

Regarding the results for case 8, the 3D simulation with the SST model predicts a shedding frequency of 208 Hz meanwhile the 2D simulation predicts 233 Hz and the experiments indicates 226 Hz. Therefore, there is a difference of about 12% between the 3D and the 2D results, and the 3D simulation predicts a lower frequency than the 2D simulation. An explanation for such frequency reduction can be obtained from the comparison between the 2D and 3D numerical results shown in Figure 5. The top graphs show the maximum cavity length of a isosurface with vapor volume fraction $\alpha_v = 0.2$, the middle graphs show the instant of cavity break off and the bottom graphs show the velocity distribution at the cavity break off instant on a surface located 0.5 mm above the hydrofoil extrados. Note that for visualization convenience, the 2D results have been enlarged 150 times in span wise direction to be compared with the 3D results. It can be observed that the maximum cavity length predicted by the 3D simulation is slightly longer than that predicted by the 2D simulation. Moreover, the re-entrant jet structure in the 3D results is not uniform in span wise direction, as observed with the

velocity distribution close to the hydrofoil extrados, and such irregularities reduce the average upstream velocity of the re-entrant jet. Therefore, both results explain why a longer time is needed by the re-entrant jet to break up the attached cavity and consequently the shedding frequency is reduced.

In spite of the differences observed between the 3D and the 2D simulation results, a significant similarity is found between them in general terms regarding the shedding process and the average pressure and velocity fields. In conclusion, given the objectives and the scope of the present study it has been decided to base our investigation on 2D simulation results and avoid the extremely high computational cost required for a full study with 3D models.

3.5. Sensitivity of the turbulence model

In Table 6, the f predicted by the three different RANS models has been compared with the shedding frequency measured experimentally for all the cavitation conditions described in Table 2, and the corresponding percent

Table 6. Influence of RANS models on calculated f .

Case	f calculated with SST			f calculated with $k-\varepsilon$			f calculated with RNG		
	f measured [Hz]	f calculated with SST [Hz]	Error [%]	f calculated with $k-\varepsilon$ [Hz]	Error (%)	f calculated with RNG [Hz]	Error (%)		
1	189.2	197	4.1	242	27.9	230	21.6		
2	250.2	266	6.3	300	19.9	260	3.9		
3	387.6	350	-9.7	400	3.2	400	3.2		
4	419.6	433	3.2	478	13.9	500	19.2		
5	96.1	100	4.0	120	24.8	-	-		
6	132.8	140	5.5	186	40.1	200	50.7		
7	175.5	186	6.0	233	32.8	260	48.2		
8	225.8	233	3.2	300	32.8	300	32.8		

errors are also indicated. Note that the value of f was obtained from the time duration of at least ten periodic cycles or from the Fourier analysis of the simulated signals.

The obtained results show that f is always over predicted by all the RANS models with the only exception of the SST model for case 3. In general, the SST model provides more accurate results with maximum errors below 10% for all the cases. Instead, the $k-\varepsilon$ and RNG models present larger errors for almost all cases. Further, the RNG model is not able to predict f for case 5. In conclusion, the SST model is the best one to simulate the unsteady periodic behavior of cloud cavitation with the current numerical parameters and a good boundary layer resolution. Therefore, all the final results presented in the following sections were obtained using the SST model and the previously stated model setup parameters.

4. Simulation of unsteady cavitation with empirical coefficients $F_v = 300$ and $F_c = 0.03$

The results presented in the previous section were calculated with the Zwart default empirical coefficients $F_v = 50$ and $F_c = 0.01$. For comparison, the numerical simulations with the SST model of all the cases listed in Table 2 were computed again using the Morgut et al. (2011) recommended empirical coefficients $F_v = 300$ and $F_c = 0.03$. Tables 7 and 8 show the calculated frequencies and maximum cavity lengths, respectively, simulated by both the default and the tuned coefficients, and the corresponding percent errors. Following the same criteria than for the experimental measurements, the predicted and measured cavity length, l , corresponds to its maximum size in chord wise direction during a shedding period before it detaches the hydrofoil surface.

These results indicate that the default coefficients provide more accurate values of f and l than the ones recommended by Morgut et al. (2011). For the default coefficients, the frequency error is less than 10% for all the cases, and the cavity length error is a little larger just for case 5 reaching around 17%. However, with Morgut's

Table 7. Comparison between measured and predicted shedding frequencies with Zwart cavitation coefficients, $F_v = 300$ and $F_c = 0.03$, proposed by Morgut et al. (2011).

Case	f measured [Hz]	f calculated (Morgut) [Hz]	Error (%)
1	189.21	134	-29.2
2	250.24	190	-24.1
3	387.57	240	-38.0
4	419.62	300	-28.5
5	96.13	91	-5.3
6	132.75	140	5.5
7	175.48	177	0.9
8	225.83	225	-0.4

Table 8. Comparison between measured and predicted maximum cavity length with both default, $F_v = 50$ and $F_c = 0.01$, and Morgut et al. (2011), $F_v = 300$ and $F_c = 0.03$, Zwart model coefficients.

Case	l calculated (default)		l calculated (Morgut)	
	l measured [mm]	Error (%)	l calculated [mm]	Error (%)
1	20	10.0	37.5	87.5
2	20	9.5	33.1	65.5
3	20	10.5	35.4	77.0
4	20	6.0	34.0	70.0
5	40	16.8	51.5	28.8
6	40	4.5	44.3	10.8
7	40	-2.0	45.3	13.3
8	40	-6.8	42.8	7.0

coefficients the model predicts values far from the experimental ones, especially for cases 1–4 with deviations from -24% to -38% in frequency estimates. This is due to an over prediction of l that, as indicated in Table 8, can reach a deviation of about +87.5%. On the contrary, for cases 5–8 the results with Morgut's coefficients are very accurate with errors below 6% in frequency estimation.

To show more details about the differences between the numerical results obtained with default and the Morgut's coefficients, the time history of V_{cav} , C_L and the local pressure at location $x/c = 0.5$ on the suction side of the hydrofoil calculated for each time step (0.00005 s) have been plotted in Figure 6 for case 8. In these plots, the horizontal axis corresponds to the dimensionless time, T^* , which has been normalized relative to the characteristic cavitation shedding period $T = 1/f$ and calculated as $T^* = t/T$. The evolution of these values is only shown during two shedding cycles although a total of 10 cycles were simulated to achieve a stable and repetitive solution in all the cases. Then, Figure 7 shows the contour plots of vapor volume fraction at corresponding instants of time during one complete shedding cycle simulated with both sets of coefficients.

From Figure 7, it can be observed that the amount of vapor inside the attached cavity and the shed cloud increases significantly when the value of F_v is increased

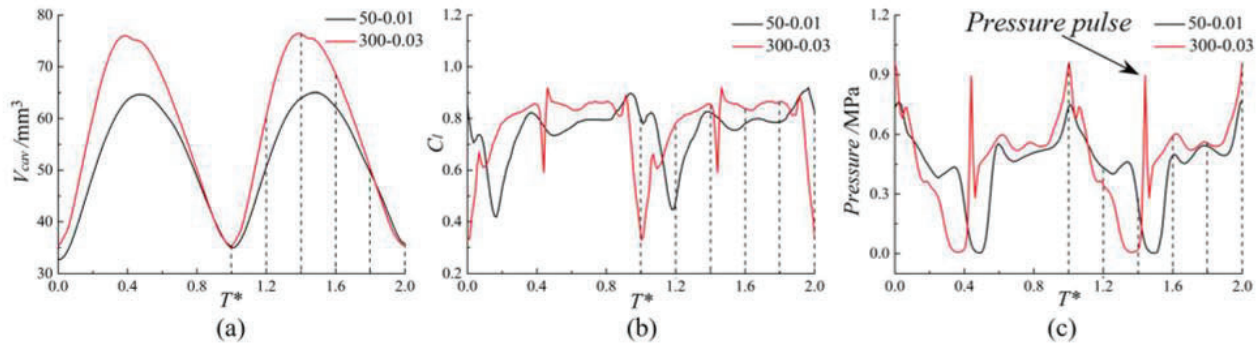


Figure 6. Values of V_{cav} (a), C_L (b) and local pressure at $x/c = 0.5$ (c) during two cavitation shedding cycles for case 8 using the default (50, 0.01) and the Morgut's (300, 0.03) empirical coefficients as a function of T^* .

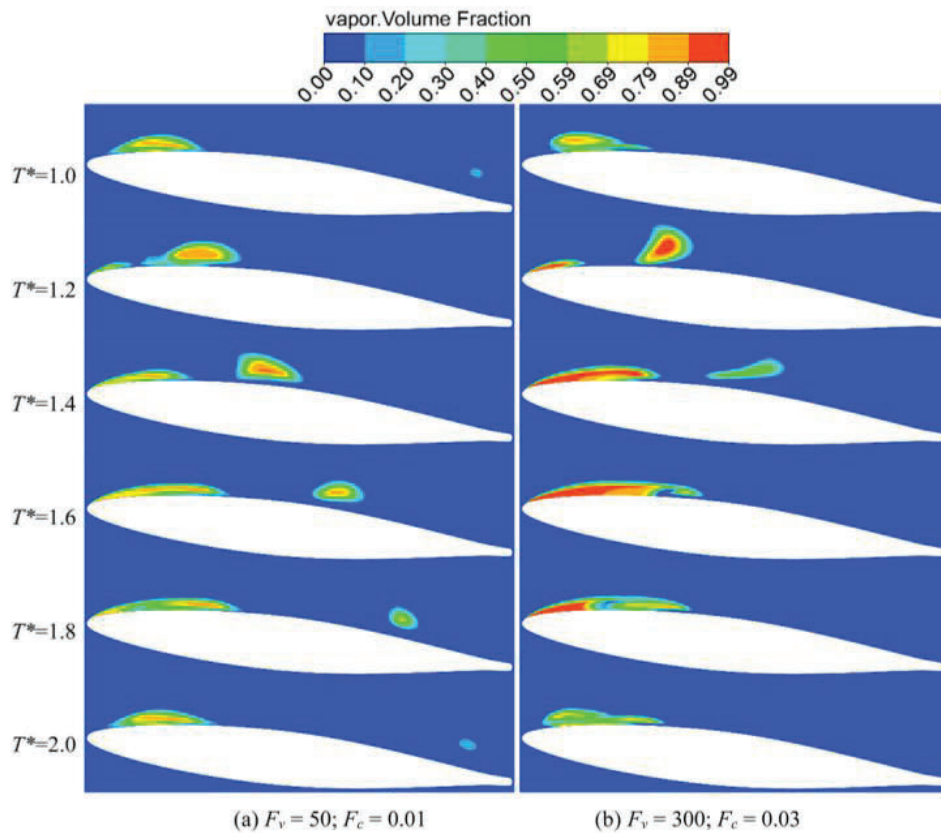


Figure 7. Instantaneous contour plots of vapor volume fraction predicted by default (a) and Morgut's (b) empirical coefficients at selected time instants during one cavity shedding cycles for case 8 (T^* values correspond to the instants marked in Figure 6 with vertical dotted lines).

from 50 to 300. As a result, a large vapor volume fraction gradient is observed at the interface between the cavitation structures and the surrounding water. Moreover, the thickness of the cavitation interface is significantly reduced. In conclusion, the obtained results with $F_v = 300$ appear to be closer to the observed cavitation morphology in the experiments by Escaler et al. (2007) and Couty (2002). These results also present similar vapor volume fractions to those measured with high-speed visualization and time-resolved X-ray

densitometry measurements by Ganesh, Mäkiharju and Ceccio (2016) in a periodically shedding cavity forming from a wedge at the end of its growth.

On the other hand, the increase of F_c from 0.01 to 0.03 permits to capture the instantaneous collapse of the shed cloud and the resulting pressure pulse on the hydrofoil surface, as it can be observed in Figure 6c. Simultaneously to the pressure peak, the C_L suffers a sudden decrease. This pressure pulse could be the cause of the experimentally observed formation and propagation of a

bubbly shock within the high void-fraction bubbly mixture in the separated cavity flow by Ganesh et al. (2016). They propose that the periodic cloud shedding could be induced by both a re-entrant jet and a shock-wave traveling upstream. Our simulations predict the re-entrant jet that pinches off the attached sheet of vapor and creates the cloud cavity that is convected downstream by the main flow. Unfortunately, our numerical model is based on an incompressible solver and thus it cannot capture the shock-wave formation.

Moreover, the final cloud collapse takes place behind the closure region of the main cavity using Morgut's coefficients, as it can be seen at instant $1.4T^*$ in Figure 7b, which is in accordance with the region where the material erosion was measured in the experiments (Couty, 2002). It has to be noted that with the default coefficient $F_c = 0.01$, the collapse takes place close to the trailing edge of the hydrofoil which is too far from the expected eroded region, as it can be observed at instant $2.0T^*$ in Figure 7a.

In conclusion, the use of the Morgut's coefficients provided a more realistic simulation of the cavitation morphology and of the collapse process. Nevertheless, for some of the cases they failed to obtain the shedding frequency mainly because the length of the attached cavity was not the correct one. Therefore, it was decided to carry out a parametric study of the empirical coefficients so that the best combination of values predicting the dynamic behavior, the vapor content of the cavities and the pressure pulse on the hydrofoil surface due to the cloud collapse could be found for all the cases indicated in Table 2.

5. Parametric analysis of Zwart empirical coefficients

For the parametric analysis, the following range of values has been taken into account:

- F_v from 100 to 500.
- F_c from 0.02 to 0.10.

For each case indicated in Table 2, a series of transient simulations were carried out using different combinations of values for F_v and F_c , which comprised a total of 200 computational runs. As a result, a full factorial design space was obtained with 25 design points evenly spaced. Then, a response surface method was applied taking as the response variable the error between the simulated shedding frequency, f , and the measured one in the experiments, and as the independent variables the dimensionless values $F_v^* = F_v/50$ and $F_c^* = F_c/0.01$. To better fit the numerical results, a polynomial

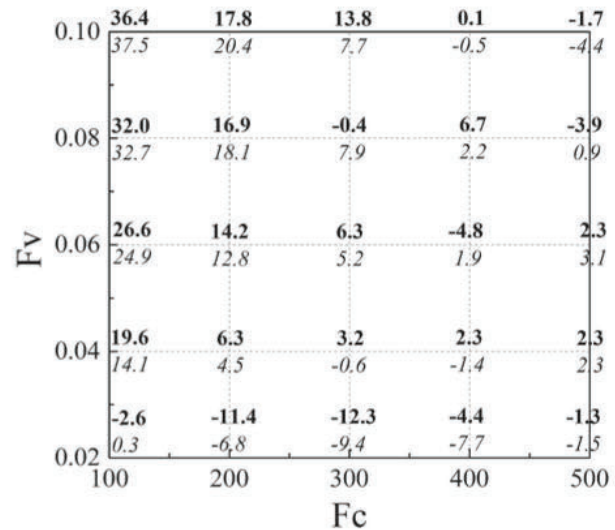


Figure 8. Comparison between CFD (**bold**) and response surface (*cursive*) frequency error predictions for case 8.

linear regression including the second order term and the interaction effects between the independent variables was obtained for each case. For example, the regression function obtained for case 8 is given as follows in Eq. 15:

$$\begin{aligned} \text{frequency error} = & -7.60 - 5.59F_v^* + 10.42F_c^* \\ & + 0.55F_v^{*2} - 0.38F_c^{*2} - 0.63F_v^*F_c^* \end{aligned} \quad (19)$$

To show the accuracy of this function, Figure 8 permits to compare the frequency error of the CFD numerical results (**bold**) with those obtained with the function (*cursive*). It can be seen that the corresponding values are generally in good agreement. The maximum residual is found for the design point (300, 0.08) for which the frequency error predicted by CFD is -0.4% meanwhile it is 7.9% when predicted by the regression function. Hence, a total maximum residual of about 8.4% is found for this particular combination of values.

Table 9 shows the statistical quality indicators of the regressions obtained for all cases. For all of them, the value of R^2 is close to 1, which indicates an accurate data fitting. The value of significance F is always less than 0.001, indicating that the model and dependent variable are statistically significant, and that the regression equation does have validity within the fitted data. Finally, it is noted that the maximum residual between the CFD and the regression model is less than 10% for all cases.

The obtained response surfaces are shown in Figure 9 for each cavitation case presented in Table 2 with their corresponding contour plots. It can be seen that for cases 1–4, the frequency error varies within a large range from -40% to 30% . On the other hand, the error range is significantly reduced for cases from 5 to 8 within the same

Table 9. Statistical quality indicators of the regressions on the frequency error obtained for every case.

Case	1	2	3	4	5	6	7	8
R-squared [-]	0.97	0.94	0.96	0.94	0.88	0.93	0.96	0.91
Significance F [-]	3E-13	5E-11	4E-13	3E-11	4E-08	3E-10	1E-12	1E-09
Maximum residual [%]	5.0	9.6	5.6	9.5	7.6	4.7	5.4	8.4

design space. This observation suggests that the simulation of the dynamic behavior is more sensitive to the values of the empirical coefficients when the cavity length is shorter. Here it must be recalled that the first 4 cases correspond to a maximum length of 20% of the chord and the last 4 cases correspond to a maximum length of 40% of the chord.

In order to find a range of values that could predict with acceptable accuracy the shedding frequency for each cavitation condition including short and long attached cavity lengths, the frequency errors from cases 1 to 8 were averaged according to Eq. 20 and the average contour plot obtained has been plotted in Figure 10a.

$$error_{ave} = \sum_{i=1}^8 |error_{i,Fc,Fv}| \quad (20)$$

In Figure 10b, the variance of the averaged frequency error for all cases has also been plotted. From these graphs, a blue region with the smallest error range can be clearly identified at the upper right of the design space, that also presents the smallest variance. This region spans

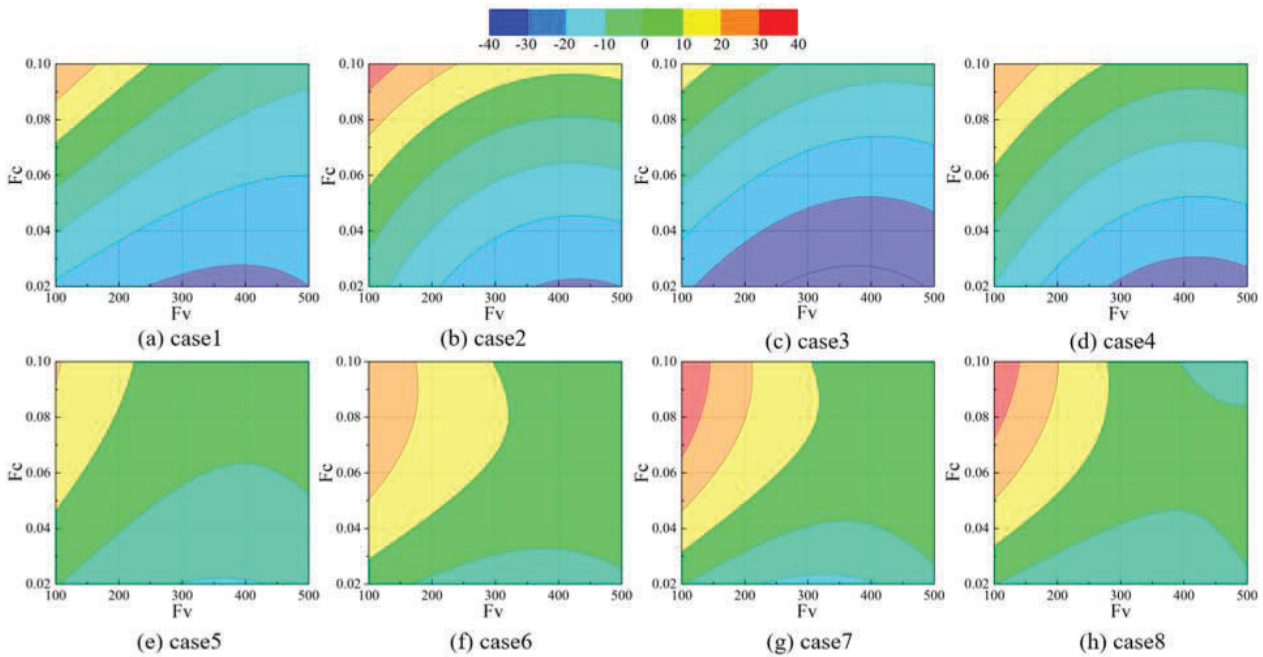


Figure 9. Contours plots of the response surfaces in terms of frequency error for all the cases.

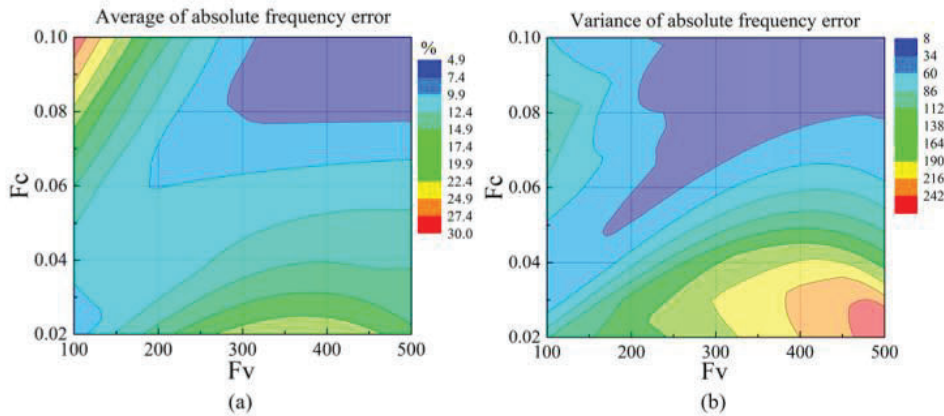


Figure 10. Average value of absolute frequency error (a) and variance of absolute frequency error (b) for cases 1–8.

Table 10. CFD frequency errors obtained with some of the optimal empirical coefficients.

Coefficients	300–0.08	400–0.08	400–0.1	500–0.08	500–0.1
case1	–1.7	–9.6	2.5	–12.3	–10.7
case2	9.5	7.1	10.7	5.9	9.5
case3	–10.3	–11.4	–6.5	–11.6	–5.9
case4	1.0	1.8	7.0	0.8	6.1
case5	8.2	–1.2	4.0	5.1	6.1
case6	13.0	2.5	2.5	7.7	8.5
case7	10.0	4.9	7.1	6.0	6.0
case8	–2.6	6.7	0.1	–3.9	–1.7
Average absolute error	7.0	5.6	5.1	6.7	6.8

from $F_V = 300$ to 500 and from $F_C = 0.08$ to 0.1. Therefore, any combination of empirical coefficients within these values should provide good estimates of the cavitation dynamic behavior independently of the cavitation size and hydrodynamic condition.

To validate the range of optimal empirical coefficients, Table 10 shows the frequency errors of the CFD results calculated with couples of coefficients within this region. The maximum frequency error found is of about 13% for case 6 and coefficients (300, 0.08). Moreover, the average value of the absolute frequency errors for each combination of coefficients spans from 5.1% to 7.0% as indicated in the bottom row, which correlates with the error range of the blue region in Figure 10a (4.9% to 7.4%). In conclusion, the feasibility and the accuracy of the results obtained by the response surface are demonstrated.

In addition, it can be observed that the optimal coefficients in Table 10 are significantly higher than the default empirical coefficients (50, 0.01) which underestimate the cavity vapor content and the intensity of the collapse process as discussed before. These results are in accordance with the recent works by Ghahramani, Arabnejad and Bensow (2019) and Schenke, Melissaris and van Terwisga (2019). Using different cavitation models, they found that the speed of the bubble collapse is significantly underestimated with low mass transfer coefficients. Moreover, they provide novel approaches which could be a future line of research for the current work.

6. Validation of the optimal empirical coefficients on a NACA0015 airfoil

To confirm the validity of the optimal range of coefficients found with the present study, the cloud cavitation behavior visualized and measured around a NACA0015 hydrofoil by Van Rijsbergen, Foeth, Fitzsimmons and Boorsma (2012) was simulated with the default coefficients (50, 0.01) and with two optimal combinations: (300, 0.08) and (500, 0.1). The SST model was used and a mesh with an average y^+ value less than 2 was created. The boundary conditions were set according to the

Table 11. Shedding frequency measured and predicted with default and the optimal coefficients found in the current study for cloud cavitation on a NACA0015 hydrofoil.

	Experiment	(50, 0.01)	(300, 0.08)	(500, 0.1)
f [Hz]	188	280	170	150
Error [%]	–	48.9	9.6	20.2

experiment description, and the same resolution strategy was followed as for the current NACA65012 model.

Table 11 shows the measured and the predicted shedding frequency of the cloud cavitation around the NACA0015 airfoil. As it can be seen, the default coefficients overestimate the frequency by around 48.9%. Meanwhile, the shedding frequency is better predicted and the error is reduced to around 9.6% for the tuned couple of values $F_V = 300$ and $F_C = 0.08$.

7. Conclusion

In the present work, transient simulations of unsteady cloud cavitation on a 2D NACA65012 hydrofoil have been carried out systematically to assess the influence of the setup parameters, RANS turbulence models and Zwart cavitation model empirical coefficients on the numerical results. In summary, it has been concluded that:

- The results are more sensitive to near wall mesh resolution than to time step, number of iterations and number of mesh elements. For the SST model, an average $y^+ = 2$ must be used, meanwhile for the $k-\varepsilon$ and RNG models a coarser grid resolution is sufficient.
- The SST model performs better than the $k-\varepsilon$ and the RNG models when the Reboud's correction is used.
- Increasing F_V , larger amounts of vapor inside the cavities are obtained with thinner interfaces between vapor and water phases, which resembles more precisely the experimental observations.
- Increasing F_C , the instantaneous collapse of the shed cloud is captured and the induced pressure pulse on the hydrofoil surface at the main cavity closure region where erosion takes place is well simulated.
- With a parametric study based on a response surface method and multiple linear regression, the optimal range of empirical coefficients to simulate the dynamic behavior of a wide range of cavitation conditions with different attached cavity lengths on 2D hydrofoils has been found. The recommended values are from 300 to 500 for F_V , and from 0.08 to 0.1 for F_C .

The present parametric study has been limited to a single objective corresponding to predict the cloud

cavitation shedding frequency on 2D hydrofoils. Further research should incorporate multiple targets such as velocity and vapor volume fraction distributions, induced pressures and vibrations, that would be considered simultaneously in a multi-objective approach. However, this work will require advanced experimental measurements with more detailed results. In this sense, the compressible approach should be used to try to capture the bubbly shock propagation as a mechanism for sheet-to-cloud transition of partial cavities.

Since the current recommendations are only valid for cavitating 2D hydrofoils in high speed water tunnels, the next step would be to simulate the 3D unsteady cavitation phenomena in hydrofoils and other simple geometries to verify the validity of the present results. And finally, the models should be validated for cavitation in actual hydraulic machines such as turbines and pumps.

Acknowledgements

Professor Desheng Zhang from Jiangsu University in China is thanked for his collaboration.

Disclosure statement

No potential conflict of interest was reported by the authors.

Funding

The present research work was financially supported by China Scholarship Council.

ORCID

Xavier Escaler  <http://orcid.org/0000-0002-9374-7749>

References

- Akbarian, E., Najafi, B., Jafari, M., Ardabili, S. F., Shamshirband, S., & Chau, K.-W. (2018). Experimental and computational fluid dynamics-based numerical simulation of using natural gas in a dual-fueled diesel engine. *Engineering Applications of Computational Fluid Mechanics*, 12(1), 517–534. doi:10.1080/19942060.2018.1472670
- ANSYS. (2015). *Release 16.2, help system, CFX theory guide*. Pittsburgh: ANSYS, Inc.
- Ayli, E., Celebioglu, K., & Aradag, S. (2016). Determination and generalization of the effects of design parameters on Francis turbine runner performance. *Engineering Applications of Computational Fluid Mechanics*, 10(1), 545–564.
- Bensow, R. E. (2011, June). Simulation of the unsteady cavitation on the Delft Twist11 foil using RANS, DES and LES. In *Second international symposium on marine propulsors*, Hamburg, Germany.
- Bilus, I., Morgut, M., & Nobile, E. (2013). Simulation of sheet and cloud cavitation with homogenous transport models. *International Journal of Simulation Modelling*, 12(2), 94–106.
- Brennen, C. E. (1995). *Cavitation and bubble dynamics*. Oxford: Cambridge University Press.
- Budich, B., Neuner, S., Schmidt, S. J., & Adams, N. A. (2015). Numerical investigation of shedding partial cavities over a sharp wedge. In *Journal of physics: Conference series* (Vol. 656, No. 1, p. 012122). IOP Publishing.
- Chen, Y., Hu, Y., & Zhang, S. (2019). Structure optimization of submerged water jet cavitating nozzle with a hybrid algorithm. *Engineering Applications of Computational Fluid Mechanics*, 13(1), 591–608.
- Couty, P. (2002). *Physical investigation of cavitation vortex collapse* (No. THESIS). EPFL.
- Dupont, P. (1993). *Etude de la dynamique d'une poche de cavitation partielle en vue de la prédiction de l'érosion dans les turbomachines hydrauliques* (No. THESIS). EPFL.
- Escaler, X., Farhat, M., Egusquiza, E., & Avellan, F. (2007). Dynamics and intensity of erosive partial cavitation. *Journal of Fluids Engineering*, 129(7), 886–893.
- Ganesh, H., Mäkiharju, S., & Ceccio, S. (2016). Bubbly shock propagation as a mechanism for sheet-to-cloud transition of partial cavities. *Journal of Fluid Mechanics*, 802, 37–78. doi:10.1017/jfm.2016.425
- Ghahramani, E., Arabnejad, M. H., & Bensow, R. E. (2019). A comparative study between numerical methods in simulation of cavitating bubbles. *International Journal of Multiphase Flow*, 111, 339–359.
- Ghalandari, M., Koohshahi, E. M., Mohamadian, F., Shamshirband, S., & Chau, K.-W. (2019). Numerical simulation of nanofluid flow inside a root canal. *Engineering Applications of Computational Fluid Mechanics*, 13(1), 254–264. doi:10.1080/19942060.2019.1578696
- Goncalves, E. (2011). Numerical study of unsteady turbulent cavitating flows. *European Journal of Mechanics - B/Fluids*, 30(1), 26–40.
- Gonçalves, E., & Patella, R. F. (2009). Numerical simulation of cavitating flows with homogeneous models. *Computers & Fluids*, 38(9), 1682–1696.
- Gopalan, S., & Katz, J. (2000). Flow structure and modeling issues in the closure region of attached cavitation. *Physics of Fluids*, 12(4), 895–911.
- Hejranfar, K., Ezzatneshan, E., & Fattah-Hesari, K. (2015). A comparative study of two cavitation modeling strategies for simulation of inviscid cavitating flows. *Ocean Engineering*, 108, 257–275.
- Ismail, B. C., Ghia, U., Roache, P. J., Freitas, C. J., & Coloman, H. (2008). Procedure for estimation and reporting of uncertainty due to discretization in CFD applications. *Journal of Fluids Engineering*, 130, 078001-1–078001-4.
- Kim, S.-e. (2009). A numerical study of unsteady cavitation on a hydrofoil. In *Proceedings of the 7th international symposium on cavitation CAV2009 August 17–22, 2009*, Ann Arbor, Michigan, USA.
- Kinzel, M., Lindau, J., Peltier, L., Kunz, R., & Sankaran, V. (2007, November). Detached-eddy simulations for cavitating flows. In *18th AIAA computational fluid dynamics conference*, p. 4098.
- Kunz, R. F., Boger, D. A., Stinebring, D. R., Chyczewski, T. S., Lindau, J. W., Gibeling, H. J., ... Govindan, T. R. (2000). A preconditioned Navier–Stokes method for two-phase flows with application to cavitation prediction. *Computers & Fluids*, 29(8), 849–875.
- Mani, K. V., Cervone, A., & Hickey, J. P. (2017). Turbulence modeling of cavitating flows in liquid rocket turbopumps. *Journal of Fluids Engineering*, 139(1), 011301.

- Morgut, M., Nobile, E., & Biluš, I. (2011). Comparison of mass transfer models for the numerical prediction of sheet cavitation around a hydrofoil. *International Journal of Multiphase Flow*, 37(6), 620–626.
- Mosavi, A., Shamshirband, S., Salwana, E., Chau, K.-W., & Tah, J. (2019). Prediction of multi-inputs bubble column reactor using a novel hybrid model of computational fluid dynamics and machine learning. *Engineering Applications of Computational Fluid Mechanics*, 13(1), 482–492. doi:10.1080/19942060.2019.1613448
- Mou, B., Bao-Jie He, B.-J., Zhao, D.-X., & Chau, K.-W. (2017). Numerical simulation of the effects of building dimensional variation on wind pressure distribution. *Engineering Applications of Computational Fluid Mechanics*, 11(1), 293–309. doi:10.1080/19942060.2017.1281845
- Pascarella, C., Salvatore, V., & Ciucci, A. (2003, November). Effects of speed of sound variation on unsteady cavitating flows by using a barotropic model. In *5th international symposium on cavitation CAV2003*, Osaka, Japan.
- Pendar, M. R., & Roohi, E. (2016). Investigation of cavitation around 3D hemispherical head-form body and conical cavitators using different turbulence and cavitation models. *Ocean Engineering*, 112, 287–306.
- Ramezanizadeh, M., Nazari, M. A., Ahmadi, M. H., & Chau, K.-W. (2019). Experimental and numerical analysis of a nanofluidic thermosyphon heat exchanger. *Engineering Applications of Computational Fluid Mechanics*, 13(1), 40–47. doi:10.1080/19942060.2018.1518272
- Reboud, J. L., Stutz, B., & Coutier, O. (1998, April). Two phase flow structure of cavitation: Experiment and modeling of unsteady effects. In *3rd international symposium on cavitation CAV1998*, Grenoble, France (Vol. 26).
- Roohi, E., Pendar, M. R., & Rahimi, A. (2016). Simulation of three-dimensional cavitation behind a disk using various turbulence and mass transfer models. *Applied Mathematical Modelling*, 40(1), 542–564.
- Rouse, H., & McNown, J. S. (1948). Cavitation and pressure distribution, head forms at zero angle of yaw, studies in engineering. *Bulletin*, 32.
- Schenke, S., Melissaris, T., & van Terwisga, T. J. C. (2019). On the relevance of kinematics for cavitation implosion loads. *Physics of Fluids*, 31(5), 052102.
- Schenke, S., & van Terwisga, T. J. (2019). An energy conservative method to predict the erosive aggressiveness of collapsing cavitating structures and cavitating flows from numerical simulations. *International Journal of Multiphase Flow*, 111, 200–218.
- Schnerr, G. H., & Sauer, J. (2001, May). Physical and numerical modeling of unsteady cavitation dynamics. In *Fourth international conference on multiphase flow* (Vol. 1). ICMF New Orleans.
- Sedlar, M., Ji, B., Kratky, T., Rebok, T., & Huzlik, R. (2016). Numerical and experimental investigation of three-dimensional cavitating flow around the straight NACA2412 hydrofoil. *Ocean Engineering*, 123, 357–382.
- Senocak, I., & Shyy, W. (2002, January). Evaluations of cavitation models for Navier-Stokes computations. In *ASME 2002 joint US-European fluids engineering division conference* (pp. 395–401). American Society of Mechanical Engineers.
- Shen, Y., & Dimotakis, P. E. (1989, August). The influence of surface cavitation on hydrodynamic forces. In *American towing tank conference*, 22nd.
- Singhal, A. K., Athavale, M. M., Li, H., & Jiang, Y. (2002). Mathematical basis and validation of the full cavitation model. *Journal of Fluids Engineering*, 124(3), 617–624.
- Tseng, C. C., & Wang, L. J. (2014). Investigations of empirical coefficients of cavitation and turbulence model through steady and unsteady turbulent cavitating flows. *Computers & Fluids*, 103, 262–274.
- Utturkar, Y., Wu, J., Wang, G., & Shyy, W. (2005). Recent progress in modeling of cryogenic cavitation for liquid rocket propulsion. *Progress in Aerospace Sciences*, 41(7), 558–608.
- Vaidyanathan, R., Senocak, I., Wu, J., & Shyy, W. (2003). Sensitivity evaluation of a transport-based turbulent cavitation model. *Journal of Fluids Engineering*, 125(3), 447–458.
- Van Rijsbergen, M., Foeth, E. J., Fitzsimmons, P., & Boorsma, A. (2012). High-speed video observations and acoustic-impact measurements on a NACA0015 Foil. In *Proceedings of the 8th international symposium on cavitation, CAV2012*, Singapore.
- Wang, G., Senocak, I., Shyy, W., Ikohagi, T., & Cao, S. (2001). Dynamics of attached turbulent cavitating flows. *Progress in Aerospace Sciences*, 37(6), 551–581.
- Yuan, C., Song, J., & Liu, M. (2019). Comparison of compressible and incompressible numerical methods in simulation of a cavitating jet through a poppet valve. *Engineering Applications of Computational Fluid Mechanics*, 13(1), 67–90.
- Zwart, P. J., Gerber, A. G., & Belamri, T. (2004, May). A two-phase flow model for predicting cavitation dynamics. In *Fifth international conference on multiphase flow* (Vol. 152), Yokohama, Japan.

Annex B

Numerical Simulation of Cavitation Erosion Aggressiveness Induced by Unsteady Cloud Cavitation

Authors:

Linlin Geng, Jian Chen, Oscar De La Torre and Xavier Escaler *

Article published in:

Applied Sciences, 2020

Article

Numerical Simulation of Cavitation Erosion Aggressiveness Induced by Unsteady Cloud Cavitation

Linlin Geng, Jian Chen, Oscar De La Torre  and Xavier Escaler * 

Departament de Mecànica de Fluids, Universitat Politècnica de Catalunya BarcelonaTech (UPC), Av. Diagonal 647, 08028 Barcelona, Spain; linlin.geng@upc.edu (L.G.); jian.chen@upc.edu (J.C.); oscar.de.la.torre@upc.edu (O.D.L.T.)

* Correspondence: xavier.escaler@upc.edu

Received: 29 June 2020; Accepted: 24 July 2020; Published: 28 July 2020



Abstract: A numerical investigation of the erosion aggressiveness of leading edge unsteady cloud cavitation based on the energy balance approach has been carried out to ascertain the main damaging mechanisms and the influence of the free stream flow velocity. A systematic approach has permitted the determination of the influence of several parameters on the spatial and temporal distribution of the erosion results comprising the selection of the cavitation model and the collapse driving pressure. In particular, the Zwart, Sauer and Kunz cavitation models have been compared as well as the use of instantaneous versus average pressure values. The numerical results have been compared against a series of experimental results obtained from pitting tests on copper and stainless steel specimens. Several cavitation erosion indicators have been defined and their accuracy to predict the experimental observations has been assessed and confirmed when using a material-dependent damaging threshold level. In summary, the use of the average pressure levels during a sufficient number of simulated shedding cycles combined with the Sauer cavitation model are the recommended parameters to achieve reliable results that reproduce the main erosion mechanisms found in cloud cavitation. Moreover, the proposed erosion indicators follow a power law as a function of the free stream flow velocity with exponents ranging from 3 to 5 depending on their definition.

Keywords: cavitation erosion; average pressure; cavitation model; velocity effect

1. Introduction

Cavitation is an unique phenomenon in the field of hydrodynamics that occurs when the local pressure in a liquid drops below a critical value, usually close to the vapor pressure, and results in the development of various types of vapor structures such as attached cavities, travelling bubbles, vortical cavities and bubble clouds [1]. Cavitation can typically take place in some widely-used hydraulic machines like pumps, turbines and naval propellers. As a matter of fact, cavitation is often associated with some unwanted consequences like machine performance deterioration, cavitation noise, cavitation-induced vibration and cavitation erosion of solid surfaces [2].

Among the problems caused by cavitation, erosion is the one of the most complex ones since it involves the interaction between fluids and structures. Actually, cavitation erosion is caused by the collapse of the cavities. It has been observed that the collapse of a bubble is a condensation process that ends with the compression of the vapor and the subsequent emission of a shock wave creating a pressure pulse with a very strong amplitude. If the collapse takes place close to a solid wall, a high-speed liquid microjet forms, crosses the bubble and impacts the wall resulting in a very high impulsive pressure. If the impulsive forces resulting either from the impact of the microjet or the

shockwave exceed the material threshold, such as its yield stress or its ultimate strength, local damage will be induced [1].

Advanced cavitation erosion may cause severe damage to components of hydraulic machines causing higher maintenance costs and deterioration of machine performance together with aggravated vibrations and noise. For example, turbine runners, fluid bearings and pump impellers among others may need replacement after several weeks/months of operation or require regular repair [2]. Therefore, from an industrial point of view concerning both design and maintenance, the evaluation of the erosive power of cavitating flows and the prediction of the material damage remains a major concern to manufacturers and operators. In this sense, several methodologies have been developed to predict cavitation erosion using Computational Fluid Dynamics (CFD) and Structural Mechanics.

A first approach focuses on the Fluid–Structure Interaction (FSI) between the cavitation phenomenon and the response of the solid boundary. Hsiao et al., [3] developed an in-house code based on FSI to study the material deformation due to the impact pressure caused by the collapse of a single bubble under different configurations, which provides a good resolution between flow field and material surface. Fivel et al., [4–6] proposed a one-way simulation method to compute the cavitation erosion based on the histogram of repetitive impact loads obtained experimentally from pitting tests and the analysis of the response of the material to them. However, the authors acknowledged that this approach to predict cavitation erosion needed further development. In addition, Joshi et al., [7,8] investigated the effect of some bubble and material properties (e.g., stand-off ratio, bubble size, driving pressure, strain rate, etc.) on the induced cavitation erosion by employing a meshless Smooth Particle Hydrodynamic (SPH) solver. More specifically, they found that the stand-off ratio has a significant effect on the erosion that permits to explain that an attached cavity has more potential to accelerate the initial damage, i.e., it requires a smaller incubation time, whereas a detached cavity leads to a higher erosion rate. Moreover, they pointed out that the strain rate effect should not be neglected in the constitutive model of the solid and that the peak pressure on the solid does not coincide with the region of maximum erosion. In summary, the SPH modelling approach represents an accurate theoretical background and, therefore, it allows exploring the FSI mechanism of cavitation erosion and establishing the relationship between the erosion intensity and the material properties. Nonetheless, its practical application to predict the erosion in hydraulic machinery is still limited since cavitation can take different patterns and the erosion is mainly caused by large-scale unsteady cavitation forms.

A second approach consists of using the Eulerian–Lagrangian method, which treats the macroscopic flow field using Eulerian mechanics and the individual microscopic bubbles using Lagrangian mechanics. Ochiai et al. [9] obtained the macroscopic flow field by solving the continuity, momentum and energy equations of a compressible two-phase flow. For the simulation of the microscopic bubbles, they considered that they follow the equation of motion driven by the pressure gradient, the drag and the virtual mass force, and they used the equation of bubble oscillation to evaluate the evolution of bubble radius. Finally, the cavitation erosion characteristics were predicted using the impact pressures on the wall surface induced by the propagating pressure waves induced by the bubble collapses. Similarly, Wang and Zhu [10] applied Large Eddy Simulation (LES) to obtain the unsteady ambient pressures and velocity profiles around the bubbles and employed the Rayleigh–Plesset equation to determine the bubble radius. They predicted the cavitation erosion following the evolution of several representative bubbles in the averaged unsteady flow with cavitation. Although this method has the best theoretical background as it considers the bubble rebounds during the collapse and the macroscopic flow, it is uninfluenced by the bubble dynamics. Another problem lies in the choice of the bubbles' injection points because they play a major role in the predicted erosion intensity [11].

The third approach, developed by Schmidt et al., [12,13], consists of predicting the impact load spectra of a cavitating flow. This method, considers the two-phase flow as homogeneous, compressible and inviscid, and it resolves the collapse-induced pressure waves to determine the spectrum of collapse events in the fluid domain. Blume and Skoda [14] used this method to assess the erosive cavitation flow

around a hydrofoil with circular leading edge and obtained a good agreement with the experimental results. However, they indicated that this approach requires a very fine computational mesh in order to capture all scales of cavitation events. Moreover, a very short time step was required because shock waves, which propagate at the speed of sound in water, needed to be resolved near the solid wall. Consequently, the practical implementation of this method is very limited. For instance, this would require a very high computational cost and take too much time to simulate any full scale components, e.g., marine propellers.

The last approach, which is the most widely applied one, only resolves the macroscopic cavitating flow field and predicts the cavitation aggressiveness by using different erosion models based on the flow properties. For example, Nohmi et al., [15] developed four erosion indices which were based on pressure and volume fraction time derivatives as well as on absolute pressure differences. Li et al., [16] stated a numerical erosion model where the rapid increase of the local static pressure needed to exceed a certain threshold level for erosion to occur. Fortes-Patella et al., [17,18] suggested an energy balance approach where the potential energy of the macroscopic cavitation structures was regarded as the main factor that generates erosion. Thus, the potential energy of a cavitation cloud is supposed to be converted into acoustic energy in the form of pressure waves. These pressure waves travel through the fluid and are able to damage the solid wall. Koukouvini et al., [19] defined a Cavitation Aggressiveness Index (CAI) based on the total derivative of pressure on the surface with values from zero that indicates the level of the hydrodynamic cavitation aggressiveness. Lloyd's Register Technical Investigation Department [20] applied Detached Eddy Simulation (DES) to simulate the cavitating flow and obtained good predictions of the eroded regions based on its own functions, but few details about them can be found in the open literature. Unlike the above mentioned erosion models in which the pressure wave is considered to be responsible for the cavitation erosion, some researchers assumed that the high-speed microjet was the main mechanism provoking the cavitation erosion. Dular et al., [21] proposed an erosion model where the velocity of the microjet needed to exceed a certain threshold to be erosive for a given material. Following this work, Peters et al. [22] calculated the erosion potential of a cavitating flow based the accumulation of the dimensionless intensity coefficient, defined by the ratio of the jet velocity to a threshold velocity value, on every element face along the total calculation time. The advantage of these approaches is that there are no critical requirements regarding the cell size and the time step and consequently the calculation time becomes more reasonable than for instance the methods included in the third approach. Nevertheless, they need to be further validated with experiments because they involve the use of some empirical coefficients.

Among the erosion models discussed above, the model proposed by Fortes-Patella et al. [17,18] has been widely used because it has been validated by various researchers and it provides a good agreement with the experiments [23–27]. Another reason for its popularity is that it has also been applied to industrial and engineering cases such as marine propellers [25] and pumps [28]. In spite of that, some uncertainties still need to be investigated and discussed to improve its performance and applicability. Therefore, the present work has been devoted to simulate systematically the erosion induced by unsteady cloud cavitation on the surface of a 2D hydrofoil and to investigate the factors influencing the erosion results including the selection of the cavitation model and of the driving pressure in the erosion model. Moreover, the main mechanisms of cavitation erosion have also been discussed by comparing the numerical results with the experimental observations. Finally, the influence of the free stream velocity and the dynamic behavior of the cavitation on the estimated erosion power has also been estimated based on the collapse efficiency.

2. Experiment Description and Numerical Model

2.1. Experiment Description

The experimental conditions and results used to validate the numerical models are listed in Table 1, comprising the hydrofoil incidence angle, α , the chord length, c , the free stream velocity, U_{inf} , the cavity

length, l , the cavitation number, σ , the shedding frequency, f , and the Strouhal number, St . σ and St have been calculated with Equations (1) and (2), respectively, where P_{in} and P_v are the inlet and the vapor saturation pressures, respectively. The computational fluid domain corresponding to the cavitation tunnel test section is shown in Figure 1 and a more detailed description of experiment can be found in Escaler et al. [29] and Couty [30].

$$\sigma = \frac{P_{in} - P_v}{0.5\rho_l U_{inf}^2} \tag{1}$$

$$St = \frac{fl}{U_{inf}} \tag{2}$$

Table 1. Flow conditions and results for the validation experiment [29].

α [°]	l/c [-]	U_{inf} [m/s]	σ [-]	f [Hz]	St [-]
6	40	15	1.55	96.1	0.26
6	40	20	1.58	132.8	0.27
6	40	25	1.60	175.5	0.28
6	40	30	1.62	225.8	0.30

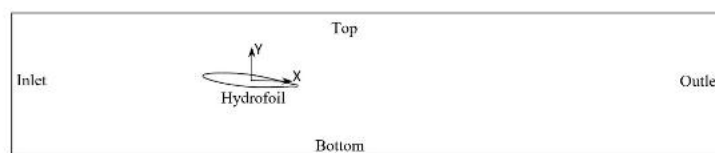


Figure 1. 2D computational domain with named boundaries and frame of reference.

In the experiment, material specimens 30 mm in width made of standard copper and stainless steel polished down to mirror were mounted along the hydrofoil suction side at different chord positions. The specimens were obtained by an accurate electroerosion machining, glued with cyanoacrylate adhesive and removed after the tests by heating to 400 °C. The erosion intensity was assessed with a statistical analysis of the pitting data measured on the specimens during the incubating period. The pitting results were quantified with the mean pitting rate at the specimen location k , $\tau_n(k)$, and the mean volume deformation rate at location k , $\tau_v(k)$, which were respectively defined as:

$$\tau_n(k) = \frac{N_k}{T_{pit} \times L_x \times L_y} \tag{3}$$

$$\tau_v(k) = \frac{\sum Vd(x_i, y_i)}{T_{pit} \times L_x \times L_y} \tag{4}$$

where N_k is the number of cavitation impacts on location k , L_x and L_y are the side lengths of the tested specimen and T_{pit} is the time duration of the pitting test. $Vd(x_i, y_i)$ represents the volume of the indentations on the surface at position (x_i, y_i) , which was measured with a 3D profilometer.

Figure 2 presents the cavitation erosion results obtained for a U_{inf} of 20 m/s for two different materials: copper and stainless steel. Firstly, the influence of the material strength can be seen by comparing the amplitudes of the erosion indicators for copper in Figure 2a with those for stainless steel in Figure 2b. For copper, the maximum values of $\tau_n(k)$ are of about $0.03 \text{ mm}^{-2}\text{s}^{-1}$ at 40% of the chord and the maximum values of $\tau_v(k)$ are of about $160 \text{ }\mu\text{m}^3\text{mm}^{-2}\text{s}^{-1}$ at 50% of the chord. Meanwhile, the maximum $\tau_n(k)$ and $\tau_v(k)$ values are of about $0.0004 \text{ mm}^{-2}\text{s}^{-1}$ and $1.9 \text{ }\mu\text{m}^3\text{mm}^{-2}\text{s}^{-1}$, respectively, at 50% of the chord for stainless steel. Therefore, the pitting rate suffered by the copper is almost two orders of magnitude higher than that for stainless steel. Regarding the location of the damages, the most eroded areas for both materials are found approximately in the range from 40 to 50% of the chord, as expected, because they have been submitted to the same cavitation conditions and the cavity

closure region was located at 40% of the chord ($l/c = 0.4$) as indicated in Table 1. For copper, $\tau_n(k)$ shows the maximum at 40% of the chord but $\tau_v(k)$ shows the maximum at 50% of the chord. This seems to indicate that the hydrofoil surface suffers a large amount of impacts with small intensity at 40% and a lower number of impacts with a stronger intensity at 50%. A slightly different erosion pattern is found for stainless steel since it presents the maximum $\tau_n(k)$ in the range from 40% to 50% but the $\tau_v(k)$ shows a minimum value at 40% and a maximum value only at 50%. Likewise, the pitting results under other operating conditions show a similar trend as for this condition. Therefore, the erosion results presented on Figure 2 will be used as the reference to validate the numerical predictions.

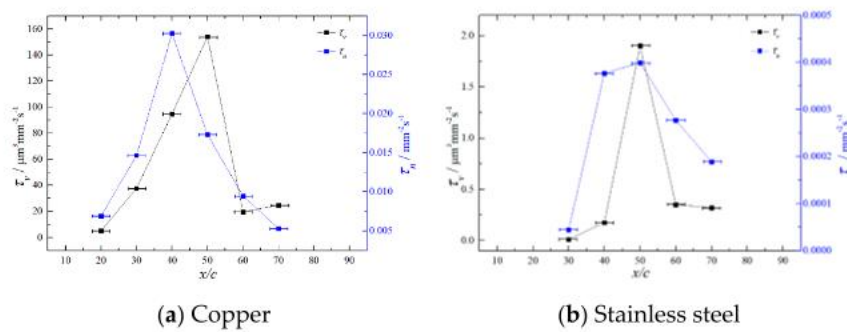


Figure 2. Experimentally measured mean volume deformation rate (black left axis) and mean pitting rate (blue right axis).

2.2. Numerical Model

The homogeneous mixture assumption has been used to model the two-phase flow. Thus, velocity and pressures are shared by water and vapor phases and the governing Navier–Stokes equations for the mixture are:

$$\frac{\partial \rho_m}{\partial t} + \frac{\partial}{\partial x_i}(\rho_m u_i) = 0 \tag{5}$$

$$\frac{\partial}{\partial t}(\rho_m u_i) + \frac{\partial}{\partial x_j}(\rho_m u_i u_j) = -\frac{\partial p}{\partial x_i} + \frac{\partial}{\partial x_j} \left[\mu_m \left(\frac{\partial u_i}{\partial x_j} + \frac{\partial u_j}{\partial x_i} - \frac{2}{3} \delta_{ij} \frac{\partial u_k}{\partial x_k} \right) \right] \tag{6}$$

where u is the velocity, p is the pressure, t is the time, μ_m is the mixture dynamic viscosity defined by $\mu_m = \mu_v \alpha_v + \mu_l (1 - \alpha_v)$ and ρ_m is mixture density calculated by $\rho_m = \rho_v \alpha_v + \rho_l (1 - \alpha_v)$.

In the present simulation, the Reynolds Averaged Navier–Stokes (RANS) approach was used, in which the instantaneous quantities are decomposed into the mean and the fluctuating components, i.e., the instantaneous velocity u_i is equal to:

$$u_i = \overline{u_i} + u_i' \tag{7}$$

Using Equation (7) to replace the instantaneous quantities of all the variables in Equations (5) and (6), the RANS equations are obtained:

$$\frac{\partial \overline{\rho_m}}{\partial t} + \frac{\partial}{\partial x_i}(\overline{\rho_m u_i}) = 0 \tag{8}$$

$$\frac{\partial}{\partial t}(\overline{\rho_m u_i}) + \frac{\partial}{\partial x_j}(\overline{\rho_m u_i u_j}) = -\frac{\partial \overline{p}}{\partial x_i} + \frac{\partial}{\partial x_j} \left[\overline{\mu_m} \left(\frac{\partial \overline{u_i}}{\partial x_j} + \frac{\partial \overline{u_j}}{\partial x_i} - \frac{2}{3} \delta_{ij} \frac{\partial \overline{u_k}}{\partial x_k} \right) \right] + \frac{\partial}{\partial x_j}(-\overline{\rho_m u_i' u_j'}) \tag{9}$$

Equations (8) and (9) have the same general form as the instantaneous Navier–Stokes equations, with the velocities and other solution variables now representing time-averaged values, and a series of new additional terms such as, $\overline{\rho u_i' u_j'}$, which are known as the Reynolds stresses induced by the turbulence. In order to close this system of equations, there are two approaches: the first one is based on the eddy-viscosity hypothesis, which relates the Reynolds stresses to the mean flow; the second one

is based on solving the transport equation for all the components of the Reynolds stress tensor. In our case, the former method has been used, so a turbulent eddy viscosity, μ_t , has been introduced to model the effect of the Reynolds stresses, and the final momentum equation to be solved becomes:

$$\frac{\partial}{\partial t}(\overline{\rho_m u_i}) + \frac{\partial}{\partial x_j}(\overline{\rho_m u_i u_j}) = -\frac{\partial \bar{p}}{\partial x_i} + \frac{\partial}{\partial x_j} \left[(\mu_m + \mu_t) \left(\frac{\partial \bar{u}_i}{\partial x_j} + \frac{\partial \bar{u}_j}{\partial x_i} - \frac{2}{3} \delta_{ij} \frac{\partial \bar{u}_k}{\partial x_k} \right) \right] \tag{10}$$

In addition, a vapor volume fraction transport equation (Equation (11)) is used to consider the mass transfer between vapor and water:

$$\frac{\partial \alpha_v}{\partial t} + \nabla \cdot (\alpha_v u) = \frac{\dot{m}}{\rho_v} \tag{11}$$

where the term \dot{m} represents the mass transfer rate between the two phases.

For the current simulation, the turbulent viscosity, μ_t , in Equation (10) has been calculated with the SST $k-\omega$ model according our previous investigation [31], and μ_t has been defined as:

$$\mu_t = \frac{f(\rho) a_1 k^2}{\max(a_1 \omega, SF_2)} \tag{12}$$

where $a_1 = 0.31$, F_2 is a blending function which restricts the limiter to the wall boundary layer, S is an invariant measure of the strain rate and k and ω are the turbulence kinetic energy and frequency, respectively. In addition, $f(\rho)$ is the density correction to reduce the over-predicted turbulent viscosity as proposed by Reboud et al. [32]:

$$f(\rho) = \rho_v + (1 - \alpha_v)^n (\rho_l - \rho_v) \tag{13}$$

where n is the exponential coefficient which should be specified with a value of 10.

Besides, the effects of the cavitation models developed by Zwart [33], Sauer [34] and Kunz [35] on the prediction of erosion were investigated. Table 2 lists the mathematical equations describing each of these cavitation models where R_B in the Zwart model is the vapor bubble radius with a constant value of 10^{-6} m. Meanwhile, in the Sauer model, it is a variable value that is function of the local vapor volume fraction. α_{nuc} is the nucleation site volume fraction with a default value of 0.0005. Then, $t_\infty = C/U_{inf}$ is the mean time scale and C_{prod} and C_{dest} are the empirical coefficients for vaporization and condensation, respectively, which were taken as 50 and 0.01 for the Zwart model, and 100 and 100 for the Kunz model.

Table 2. Mathematical expressions of the cavitation models.

Model	$\dot{m} (P < P_v)$	$\dot{m} (P > P_v)$
Zwart	$C_{prod} \frac{3\alpha_{nuc}(1-\alpha_v)\rho_v}{R_B} \sqrt{\frac{2}{3}} \frac{(p_v-p)}{\rho_l}$	$-C_{dest} \frac{3\alpha_v\rho_v}{R_B} \sqrt{\frac{2}{3}} \frac{(p-p_v)}{\rho_l}$
Sauer	$\frac{\rho_v\rho_l}{\rho} \alpha_v(1-\alpha_v) \frac{3}{R_B} \sqrt{\frac{2}{3}} \frac{(p_v-p)}{\rho_l}$	$-\frac{\rho_v\rho_l}{\rho} \alpha_v(1-\alpha_v) \frac{3}{R_B} \sqrt{\frac{2}{3}} \frac{(p-p_v)}{\rho_l}$
Kunz	$\frac{C_{dest}\rho_v\alpha_v(1-\alpha_v)^2}{t_\infty} + \frac{C_{prod}\rho_v(1-\alpha_v)\min[0,p-p_v]}{(0.5\rho_l U_{inf}^2)t_\infty}$	$-\frac{C_{dest}\rho_v\alpha_v(1-\alpha_v)^2}{t_\infty}$

The solution strategy adopted for the current simulations was based on our previous work [31] where the influence of the numerical setting was investigated in detail. Consequently, a medium-sized mesh of 29,749 elements with $y+$ values in the boundary layers ranging from 0.1 to 3 with a mean value of 1.2 was used. A time step of $3 \cdot 10^{-5}$ s corresponding to a Root Mean Square (RMS) Courant number of 1.6 was set as well as several successive iterations within each physical time step. A very small residual criterion of 10^{-8} and a large iterative number were set to march the solution towards convergence in every time step. The pressure-velocity direct coupling method was used to solve the

governing equations. The high-resolution scheme was used for the convection terms. The second-order implicit time scheme was used for the transient term. To accelerate convergence, a series of transient simulations were run from previous steady state models. The simulations were carried out in parallel using twelve cores of an Intel®Core™ i7-8700 K CPU equipped with 32 GB of RAM. Every unsteady simulation was stopped after at least ten cavity shedding cycles were captured, which took around 12 h for each case. In addition, much effort was taken on building the relationship between the cavity structures and their corresponding erosion intensities during the postprocessing of the obtained results. To achieve a very precise prediction of the position of cavity closure region, which is needed to simulate cavitation erosion [24,36], the cavitation number had to be adjusted to match exactly the same cavity length than in the experiment. Therefore, a cavitation number of 1.55 was used in the simulation, which was based on cavitation tunnel inlet pressure, as compared to the cavitation number of 1.58 set in the experiment.

2.3. Cavitation Erosion Model

The cavitation erosion model used in the calculations was developed by Fortes-Patella et al. [17,18]. In this model, the pressure waves emitted during the cavitation collapses that reach the solid wall are the main mechanism responsible for erosion damage. The potential energy of a vapor structure in the fluid domain is defined as:

$$E_{pot} = \Delta p V_{vap} = (p_d - p_{vap}) V_{vap} \tag{14}$$

where V_{vap} is the volume of the vapor structure and p_d is the driving pressure which forces its collapse. Then an instantaneous potential power, P_{pot} , can be defined with Lagrangian time derivatives as expressed with Equation (15):

$$P_{pot} = \frac{DE_{pot}}{Dt} = (p_d - p_{vap}) \frac{DV_{vap}}{Dt} + \frac{Dp}{Dt} V_{vap} \tag{15}$$

Because the vapor volume is related to the vapor volume fraction, $\alpha_v = V_{vap}/V_{cell}$, the potential power in each cell or the potential power density, P_{den} , can be written as:

$$P_{den} = \frac{P_{pot}}{V_{cell}} = (p_d - p_{vap}) \frac{D\alpha_v}{Dt} + \frac{Dp}{Dt} \alpha_v \tag{16}$$

Leclerc et al., [36] found that the second term on the right-hand side of Equation (16) is negligible compared to the first term and they assumed that P_{pot} is released instantaneously only when condensation takes place. This implies that only the first term on the right-hand side of Equation (16) contributes to the radiated power and only if the time derivative of α_v is positive. Therefore, P_{den} can be simplified to Equation (17):

$$P_{den} = \frac{P_{pot}}{V_{cell}} = (p_d - p_{vap}) \frac{D\alpha_v}{Dt} \tag{17}$$

Note that P_{pot} is defined with Lagrangian time derivatives, which can be obtained substituting the sum of the first and second terms in the right-hand side of Equation (11) with the following relation:

$$\frac{D\alpha_v}{Dt} = \frac{\partial\alpha_v}{\partial t} + \nabla \cdot (\alpha_v u) - \alpha_v \nabla \cdot u \tag{18}$$

Besides, the divergence term, $\nabla \cdot u$, is actually another form of continuity equation (Equation (5)) defined as $\nabla \cdot u = \dot{m} \left(\frac{1}{\rho_v} - \frac{1}{\rho_l} \right)$ [26]. Hence, Equation (18) can be rewritten as:

$$\frac{D\alpha_v}{Dt} = \frac{\dot{m}}{\rho_v} - \alpha_v \dot{m} \left(\frac{1}{\rho_v} - \frac{1}{\rho_l} \right) = \dot{m} \frac{\rho}{\rho_v \rho_l} \tag{19}$$

Assuming that the positive time derivative contributes to erosion and combining Equations (17) and (19), P_{den} can be finally defined for a given cell as:

$$P_{den} = \frac{p_{pot}}{V_{cell}} = (p_d - p_{vap}) \max\left(\dot{m} \frac{\rho}{\rho_v \rho_l}, 0\right) \tag{20}$$

Equation (20) shows that P_{den} is determined by the driving pressure, p_d , which can be defined as the pressure in a cell or the averaged pressure according to the references [18,23] and [26,27], respectively, and by the source term, \dot{m} , which depends on the cavitation model being used. Therefore, the definition of p_d and the selection of the cavitation model should have an influence on the predicted values of P_{den} .

In order to calculate the potential power reaching a certain position j on the surface of the hydrofoil that has been induced by a collapse occurring at a given point source i on the fluid domain at instant t , the method proposed by Sören and van Terwisga [26] has been applied. For that, it has been assumed that $P_{den}(i,t)$ propagates circumferentially with an infinite wave speed in radial direction without energy losses and that it reaches position j at the same time t , as outlined in Figure 3.

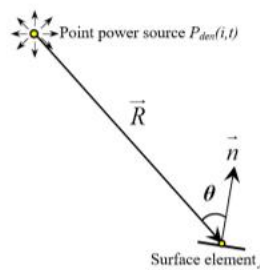


Figure 3. Schematic of the point power source where the cavity collapse takes place and its path to the point on the hydrofoil surface that will be loaded by the emitted power.

Then, the power reaching position j on the surface of the hydrofoil at instant t , $P_{imp}(j,t)$, can be calculated as:

$$P_{imp}(j,t)|_i = P_{den}(i,t) \frac{1}{2\pi} \frac{\vec{R} \cdot \vec{n}}{|\vec{R}|} \tag{21}$$

where \vec{R} is the position vector of the center j of the surface element from the point source i and \vec{n} is the normal vector of this surface element. The contribution of all source points to the loaded power on point j at instant t , $P_{load}(j,t)$, can be calculated integrating Equation (21) over the area (*surf*) of the whole computational domain as:

$$P_{load}(j,t) = \int_{surf} p_{imp}(j,t)|_i dA \text{ expressed in W/m}^2 \tag{22}$$

Finally, to estimate the cavitation erosion risk on the surface element, the total power received at a given element j due to the accumulation of all the collapses occurred during the period of a complete shedding cycle, P_{tot_load} , can be calculated as:

$$P_{tot_load} = \sum_1^{N_{ref}} \max((P_{load}(j,t) - P_{threshold}), 0) \tag{23}$$

where N_{ref} is the number of time steps simulated during a complete shedding cycle and $P_{threshold}$ is the power threshold above which the material is actually eroded by cavitation. Obviously, $P_{threshold}$ could be assumed to be analogous to a particular material resistance property like the yield stress and it must be validated through experimental tests.

More specifically, P_{tot_load} has been calculated for the first layer of elements on the hydrofoil extrados wall along the chord comprising 50 elements with a width of 2 mm each. Consequently, it has been assumed that P_{tot_load} represents the total cavitation erosion power received on the hydrofoil surface during one characteristic shedding cycle.

3. Results

In the previous section it has been mentioned that the choice of the cavitation model and the definition of p_d in Equation (20) might bring some uncertainty to the calculation of P_{den} and that this can lead to different estimates of P_{load} on the hydrofoil wall. Thus, these possible effects have been investigated in detail based on the transient results obtained during a sufficiently long period of time.

Figure 4 shows the numerically predicted time evolution of the total vapor volume within the fluid domain over ten shedding cycles obtained with the three different cavitation models. It can be observed that for the Sauer model the total vapor volume fluctuations are repeatable while for the Zwart and the Kunz models their periods and amplitudes are not so constant from cycle to cycle. Nonetheless, the unsteady cavity behavior is actually quite regular for all the models. In addition, the averaged shedding frequencies calculated in the entire period are 140, 139 and 130 Hz for the Zwart, Sauer and Kunz models, respectively. Thus, it is confirmed that all the results are in good agreement with the expected experimental frequency of 132.8 Hz. Consequently, all the models demonstrate a good performance in capturing the cloud cavitation dynamic behavior.

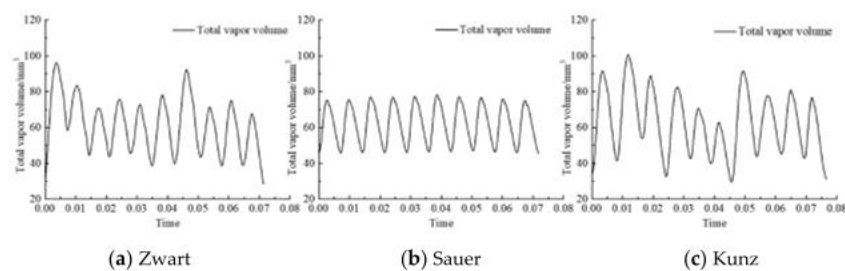


Figure 4. Numerically predicted time evolution of the total vapor volume in the fluid domain with the different cavitation models.

3.1. Influence of Driving Pressure Definition

The numerical results from two consecutive shedding cycles have been selected to calculate P_{load} on the hydrofoil surface with the different cavitation models and the obtained results have been plotted in Figure 5.

The top graphs in Figure 5 have been obtained considering p_d as the flow field instantaneous pressure, $p(t)$. Conversely, the bottom graphs have been obtained considering p_d as the averaged pressure over ten cycles, \bar{p} . It can be observed that the space-time distributions of P_{load} on the suction side are different depending on which value has been used. For example, when taking the results obtained with the Sauer model, a region with high P_{load} has been predicted from 20% to 65% of the chord using \bar{p} in the initial time ranges of each cycle from 0.2 to 0.45 T/T_{ref} and from 1.2 to 1.45 T/T_{ref} . It is observed that using $p(t)$ the calculations can only capture a high P_{load} during a very short instant around 1.45 T/T_{ref} . Moreover, the amplitude of P_{load} is also different even though the attack occurs in a similar time-space region. Another large amplitude of P_{load} has been found with the use of both $p(t)$ and \bar{p} on a location around 40% of the chord from 0.45 to 1.0 T/T_{ref} for the first cycle and from 1.45 to 2.0 T/T_{ref} for the second cycle. However, this amplitude was higher when taking \bar{p} as the driving pressure. To finish, similar differences have also been found when comparing the results of the other two cavitation models.

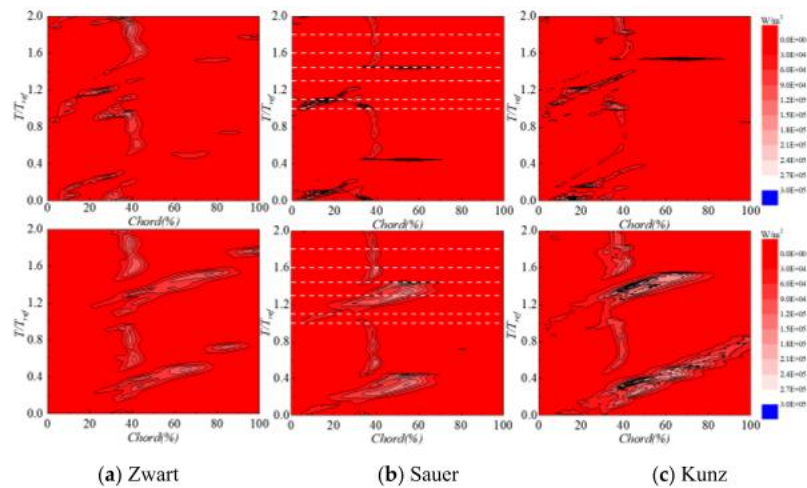


Figure 5. Comparison of calculated power load per unit area, P_{load} , on the hydrofoil surface based on instantaneous pressure, $p(t)$ (top) and on average pressure, \bar{p} (bottom).

To understand such differences, the obtained \dot{m} from vapor to water has been presented in Figure 6 for the second cycle at various relative instants, T/T_{ref} , marked with dotted lines in Figure 5b. Three stages of the cavity shedding process can be roughly identified. Firstly, the formation of the sheet cavity and its detachment occurs from 1.0 to 1.2 at the initial stage of the shedding process. Figure 6a,b at instants 1.0 and 1.1, respectively, show how the main sheet cavity detaches due to the re-entrant jet and then how a cloud cavity forms and begins to be convected downstream. The second stage ranges from 1.2 to 1.45 and corresponds to the collapse of the cloud cavity. In Figure 6c,d, it can be seen at instant 1.3 how the cloud cavity flows downstream and starts to collapse. Afterwards, the final collapse occurs at instant 1.44. Finally, the stage from 1.45 to 2.0 corresponds to the new growth and formation of the attached sheet cavity. As shown in Figure 6e,f, the sheet cavity reaches its maximum length and then a stagnation point at its closure region forms because the flow over the cavity turns towards the surface. This stagnation point creates a high pressure region which drives the upstream re-entrant jet below the attached cavity and triggers the collapse of the small vapor structures detached at the rear part of the sheet.

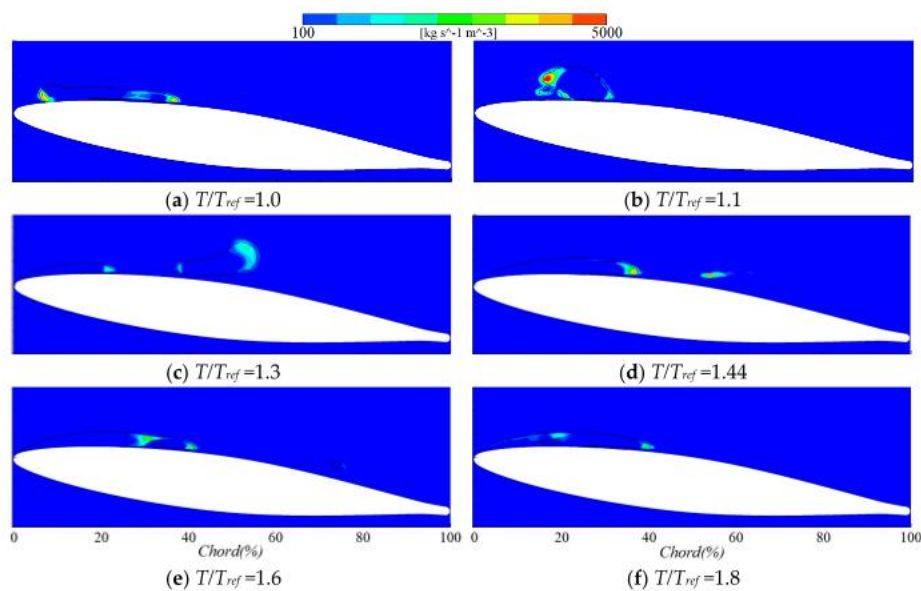


Figure 6. Contours of \dot{m} from vapor to water at different instants of the shedding cycle. Black isolines of $\alpha_v = 0.1$ show the locations of the main vapor cavities at each instant.

The results obtained using both $p(t)$ and \bar{p} have been plotted on the left- and right-hand sides of Figure 7 for comparison. In particular, the corresponding distributions of $p(t)$ and \bar{p} , the distribution of P_{den} as well as the evolution of P_{load} on the hydrofoil surface along chord (red line) have been plotted at different instants. Moreover, the isolines of $\alpha_v = 0.1$ (black lines) have been superimposed to those graphs to show the location of the main vapor cavities. From a general overview, it can be confirmed that the value of p_d has a significant influence on the results.

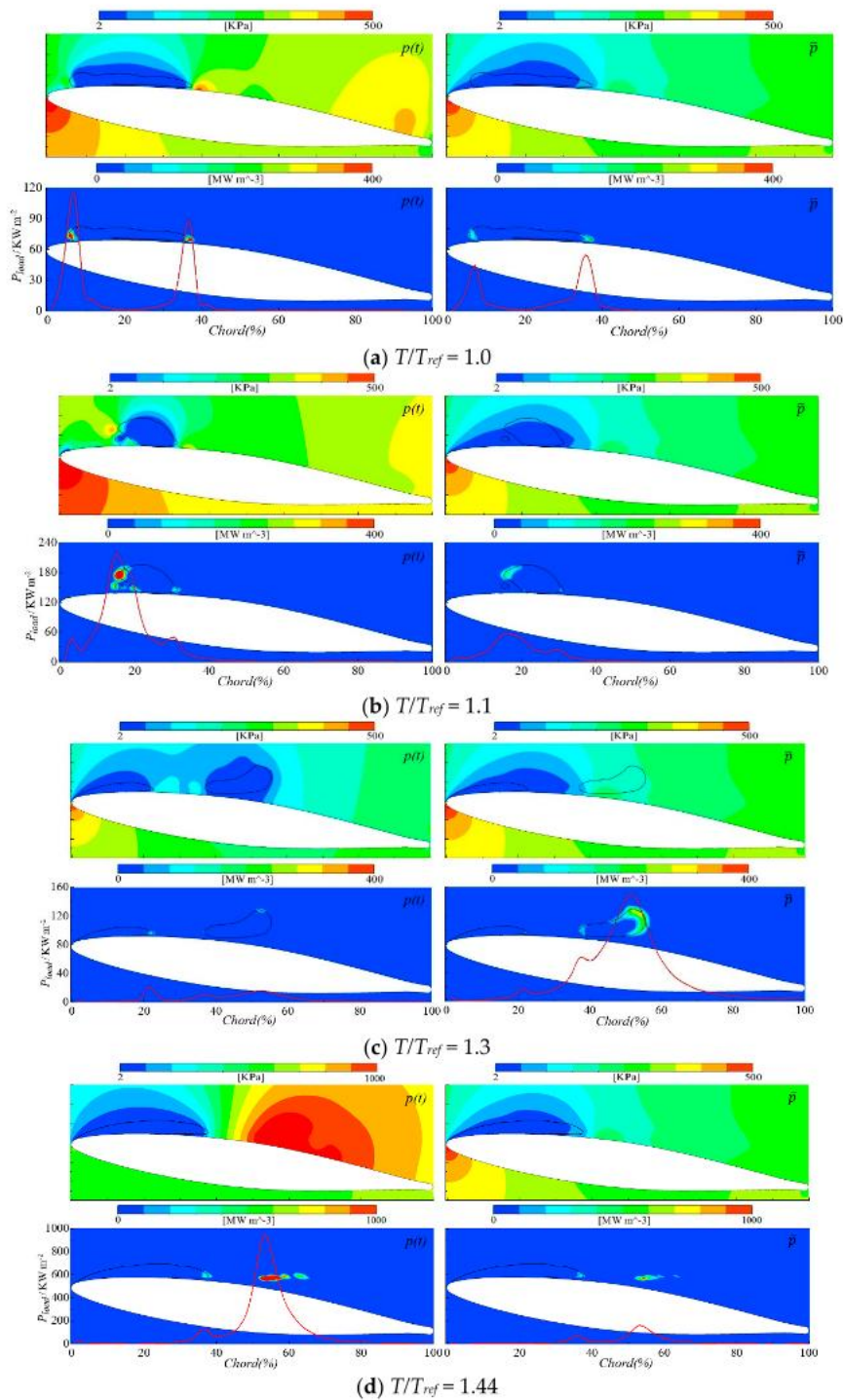


Figure 7. Cont.

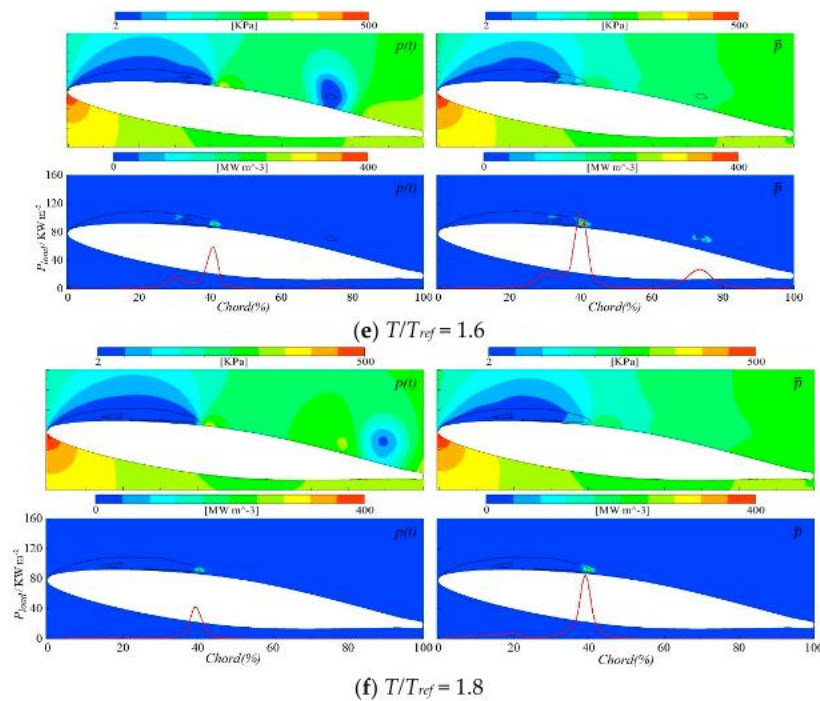


Figure 7. Contours of $p(t)$ (top left), \bar{p} (top right), P_{den} and amplitude of P_{load} along the chord (bottom left and right) obtained using $p(t)$ (left) and \bar{p} (right). Red lines showing the value of the power load on the surface along the chord. Black isolines of $\alpha_v = 0.1$ show the locations of the main vapor cavities at each instant.

The results presented in Figure 6a at instant 1.0 show that the highest condensation processes take place at both ends of the attached cavity. In Figure 7, it is also confirmed that the values of $p(t)$ in the condensation regions at this instant are higher than the corresponding values of \bar{p} . It can be seen that a higher P_{den} is predicted on the fluid using $p(t)$, and correspondingly it results in a higher P_{load} on the hydrofoil surface. Likewise, at instant 1.1, the $p(t)$ in the condensation region is also higher than \bar{p} , leading to a locally higher P_{load} . However, this is not a reliable result because, at this stage, when the sheet cavity is transformed into a cloud cavity, no strong collapses are expected to occur.

The results presented in Figure 6c at instant 1.3 show condensation regions located on the margin of the cloud cavity because the pressure in its outer region is definitely higher than that within its interior as shown in Figure 7c. Moreover, $p(t)$ is very low and even almost equal to the vapor pressure inside the cloud cavity region marked by the isoline, which implies that the pressure difference between the driving pressure and vapor pressure is close to zero. As a result, a very low aggressiveness on the hydrofoil surface is predicted. On the other hand, the use of \bar{p} determines a higher P_{den} and P_{load} at the condensation region.

The final cloud collapse takes place at instant 1.44, as shown in Figures 6d and 7d, when a local value of $p(t)$ over 1 MPa is predicted inducing the maximum values of P_{den} and P_{load} . However, this instantaneous pressure peak is the consequence of the final collapse but it is not the pressure source driving the cavity collapse. Moreover, the appearance of this local pressure peak is considered by Bensow et al., [37] to be a spurious effect of the numerical calculation. In contrast, the P_{den} and P_{load} predicted using \bar{p} are much lower because the \bar{p} levels are significantly smaller than the $p(t)$ ones.

Finally, the area with the highest erosion power is mainly concentrated on the closure region of the sheet cavity as shown in Figure 7e at instant 1.6. In addition, a small cavity also appears after the final collapse of the cloud cavity due to the vortex rebound [38]. Comparing the results predicted using $p(t)$ or \bar{p} , the latter gives higher P_{den} and P_{load} because its level on the condensation area is higher than for the former. Similarly, the results at instant 1.8 allow us to verify the previous observations.

Figure 8 shows the accumulated P_{tot_load} levels along the hydrofoil chord during one shedding cycle from instant 1 to 2 using Equation (23) with $P_{threshold}$ equal to zero. It is observed that P_{tot_load} along the chord is much lower when using $p(t)$ than \bar{p} , with the exception of a small region near the leading edge when using the Zwart and the Sauer models. Another observation is that the P_{tot_load} levels near the leading edge are even higher than those on the region where the cloud cavity collapses when using $p(t)$. As already discussed before, this is because $p(t)$ gives a higher P_{den} and P_{load} during the transition from sheet to cloud cavity but underestimates P_{den} during the cloud cavity collapse because the pressure difference between $p(t)$ and vapor pressure is close to zero. Therefore, the results given by $p(t)$ are not reasonable because they are in contradiction with the experimental results presented in Figure 2 proving that no significant erosion occurs along the chord in the range from 0 to 20%. Meanwhile, strong erosion is found downstream of the cavity closure region. In summary, it is confirmed that the cavitation erosion prediction results are sensitive to the definition of the driving pressure, and that the results obtained with \bar{p} seem to be more in agreement with the experiments. Consequently, they will be taken into account in the following sections.

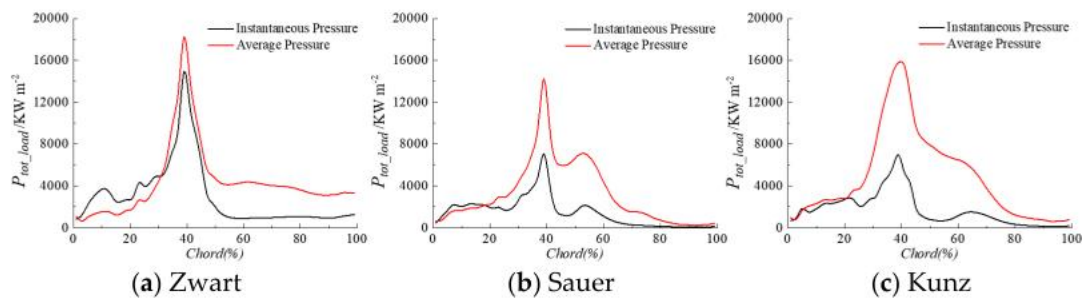


Figure 8. The accumulated total power load during the second shedding cycle predicted using $p(t)$ or \bar{p} with different cavitation models.

3.2. Influence of Cavitation Model

Figure 9 demonstrates that the contours of \bar{p} obtained with the different cavitation models are similar, which reinforces the assumption that the study of the influence of the cavitation model on P_{den} and P_{load} can be done using \bar{p} as driving pressure.

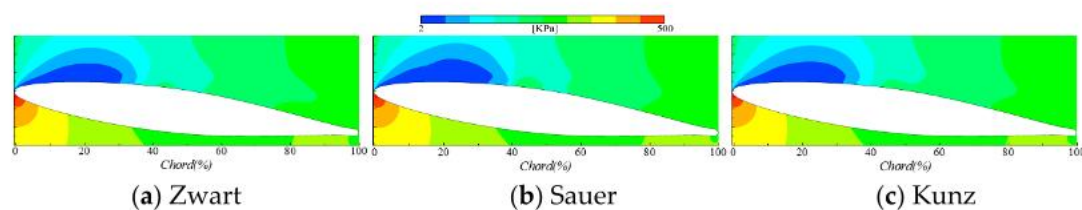


Figure 9. Contours of \bar{p} predicted with the different cavitation models.

Figure 10 presents the contours of condensation \dot{m} and P_{den} at different instants of the shedding process obtained with the Zwart, Sauer and Kunz cavitation models, as well as the evolution of P_{load} on the hydrofoil surface along the chord.

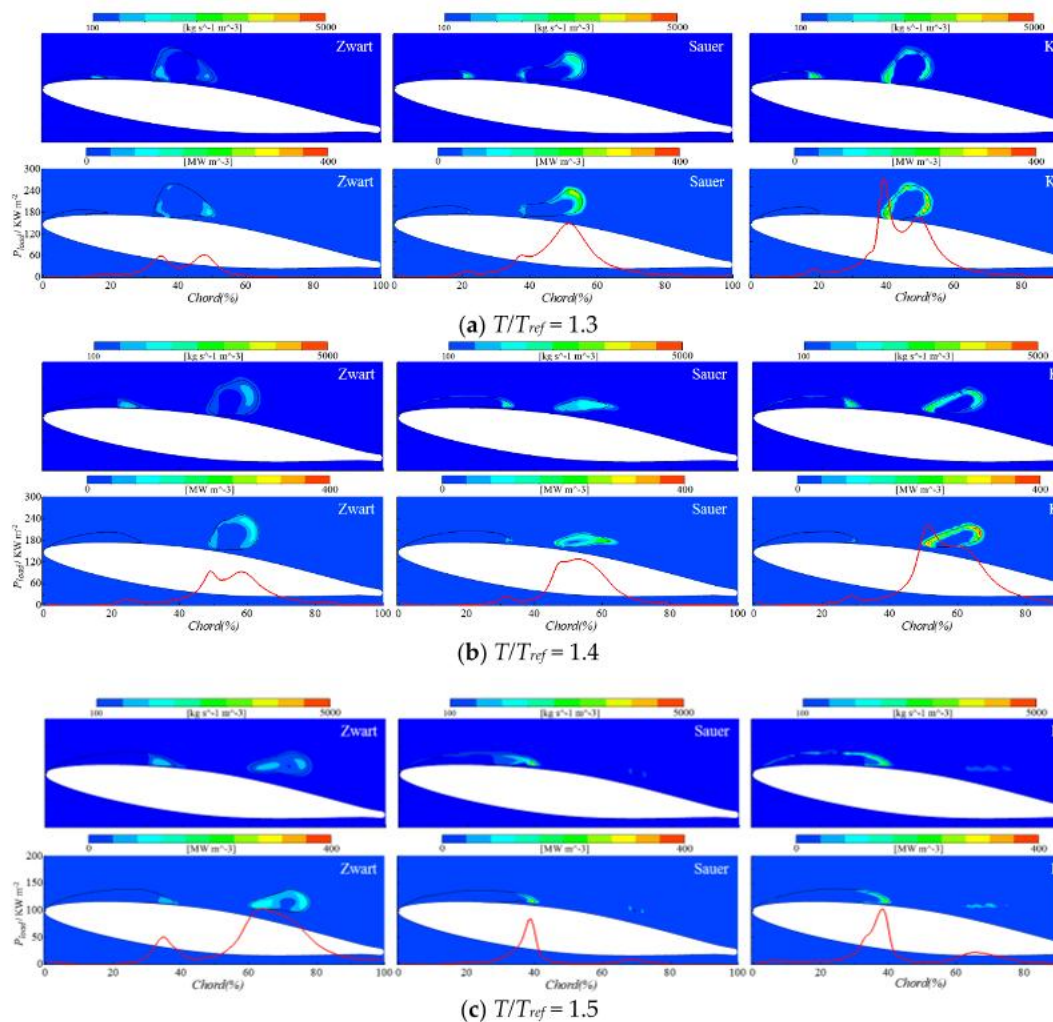


Figure 10. Results obtained with the Zwart (**left**), Sauer (**middle**) and Kunz (**right**) models at different instants comprising contours of m from vapor to water (**top**) and of P_{den} , and value of P_{load} on the surface along the chord (red line in bottom graphs). Black isolines of $\alpha_v = 0.1$ show the location of the main vapor cavities at each instant.

In Figure 10a, the Zwart model predicts a cloud cavity at instant 1.3 with low condensation rate on its outer region and a maximum P_{load} of about 60 kWm^{-2} which is the lowest figure compared to the other models. On the contrary, the Sauer and the Kunz models predict a smaller cavity volume and a higher P_{load} induced by the higher condensation rate on the outer region of the cloud. More specifically, the Kunz model predicts the highest P_{load} of about 240 kW m^{-2} at 40% of the chord because a part of the condensation region of the cloud cavity is much closer to the hydrofoil surface than in the rest of results. Similarly, the Zwart model predicts again the smallest condensation rate and P_{load} at instant 1.4. The other two models predict a relatively higher intensity especially for the Kunz one. At instant 1.5, the cloud cavity still presents a large volume with the Zwart model, meanwhile with the Sauer model the cavity already vanishes at instant 1.44, as shown in Figure 6d, and it reappears with a very small volume due to the collapse rebound. With the Kunz model, the cloud cavity finishes its final collapse at this particular instant. This indicates that the final collapse occurs at different instants and at different chord locations depending on the cavitation model. Furthermore, the collapse process predicted with the Zwart model creates a lower P_{load} than the rest. Comparing Figures 6d and 10c, it can be seen that the Sauer model predicts a much higher condensation rate than with the Kunz model when the final collapse occurs, which leads to a higher P_{den} and P_{load} , as shown in Figure 7d.

Figure 11 shows the results at instant 0.5 corresponding to an analogous situation to the one observed at instant 1.5 presented in Figure 10c. By comparing these results, it can be seen that the cavity behavior differs between the two consequent cycles depending on the cavitation model being used. The cavity topologies at these two instants are very similar with the Sauer model, showing that the sheet cavity has reached its maximum length with a high P_{load} at its closure region and that a very small cloud cavity appears at 70% of the chord inducing a small P_{load} . Likewise, the cavity behavior and the P_{load} provided by the Zwart model at these two instants are also similar. However, the results for the Kunz model are different since there is a cloud with a larger volume of vapor that induces the maximum P_{load} at 75% of the chord at instant 0.5, which cannot be observed at instant 1.5 in Figure 10c. Similarly, the space-time distributions of P_{load} in Figure 5 are significantly different between the time span from 0 to 1 and from 1 to 2 for the Kunz model, meanwhile they are quite similar for the other two models. Consequently, it can be concluded that the Zwart and Sauer models provide similar predictions of the erosion power in terms of erosion aggressiveness and location from cycle to cycle, while the Kunz model provides results that differ from cycle to cycle.

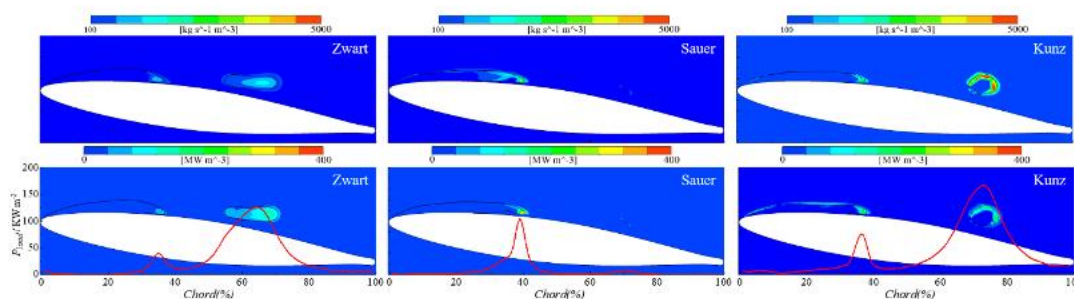


Figure 11. Results obtained with the Zwart (left), Sauer (middle) and Kunz (right) models at instant $T/T_{ref} = 0.5$ comprising contours of \dot{m} from vapor to water (top) and contours of power density and value of the power load on the surface along the chord (red line in bottom graphs). Black isolines of $\alpha_v = 0.1$ showing the location of the main vapor cavities at each instant.

Figure 12 represents compares the values of P_{tot_load} without setting any threshold value for two consecutive shedding cycles obtained with the three cavitation models. With the Zwart model, a similar shape and amplitude of the P_{tot_load} distribution is found in both cycles although the second one gives a slightly higher intensity. With the Sauer model, the two cycles show exactly the same result. In contrast, with the Kunz model a significant difference is found in the second half of the chord. More specifically, P_{tot_load} drops with a faster rate towards a very small amplitude at 80% of the chord during the second cycle, meanwhile P_{tot_load} decreases more gradually and it is still significant even at the trailing edge during the first cycle. Note that similar differences between two consecutive cycles are also observed along the 10 cycles shown in Figure 5 for all the cavitation models.

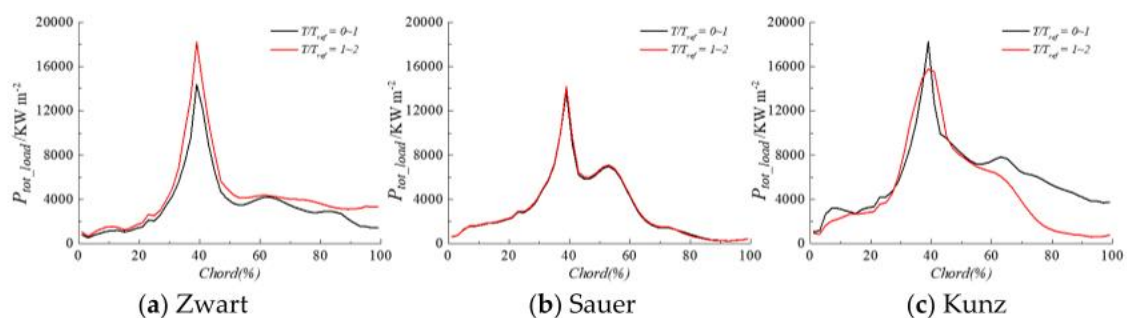


Figure 12. Comparison of P_{tot_load} distribution obtained for the first (black line) and second (red line) shedding cycles with the different cavitation models.

Another conclusion that can be extracted from Figure 12 is that the cavitation model also influences the erosion distribution along the chord. More specifically, all three models give the maximum values of P_{tot_load} around 40% of the chord at the attached cavity closure region but they give different results at the cloud cavity collapse region. With the Zwart model, the collapses of the clouds, shown on the left hand side of Figure 10, are less intense and they take place close to the trailing edge presenting a low amplitude of P_{tot_load} from 50 to 100% of the chord. With the Sauer model, the cloud collapses are concentrated from 50 to 60% of the chord and the results show a small peak around 55% of the chord. With the Kunz model, the results are sensitive to the shedding cycle being considered. According to the experimental results presented in Figure 2, the main eroded area was located from 30 to the 70% of the chord and the maximum erosion was found from 40 to 50% of the chord. Based on these results, it can be concluded that the cavitation power distribution predicted by the Sauer model agrees more precisely with the experimental observations.

Based on the previous discussion, it can be stated that different cavitation models give different results of cavitation aggressiveness regarding the condensation \dot{m} , which determines the level of P_{den} , and regarding the cavity topology, which determines the efficiency of the transmission from P_{den} to P_{load} on the surface and the size and location of the area subjected to the highest P_{tot_load} . Nonetheless, it can be concluded that the Sauer model gives a more accurate prediction of cavitation aggressiveness than the rest.

3.3. The Mechanism of Cavitation Erosion

In this section, the numerical results obtained with the Sauer model have been used to discuss the mechanisms of cavitation erosion based on the comparison with the experimental observations. For that, the second cycle results from instants 1 to 2 have been considered without any loss of generality because the Sauer model has shown a good repeatability for all the simulated shedding cycles.

Figure 12b shows that the maximum P_{tot_load} is found both at the closure region of the attached sheet cavity and at the location where the main cloud cavity collapses. Nevertheless, the calculation of P_{tot_load} without taking into account the fact that a $P_{threshold}$ level exists is not an accurate method to estimate the actual erosion risk. Therefore, a $P_{threshold}$ has been set to eliminate the contribution of low intensity collapses not being sufficiently high to cause material damage. For that, the number of effective time steps at which P_{load} is higher than $P_{threshold}$ at any chord location, N_{eff} , has been considered to estimate the average erosive power load, P_{ave_load} , at each effective time step and hydrofoil position with the following expression:

$$P_{ave_load} = \frac{P_{tot_load}}{N_{eff}} \quad (24)$$

If N_{ref} is the number of time steps in one cycle of duration T_{ref} , then the ratio N_{eff}/N_{ref} accounts for the percent time duration during one shedding cycle with P_{load} values higher than $P_{threshold}$.

In the present study, two $P_{threshold}$ levels with values of 30 kW m⁻² and 90 kW m⁻² have been considered to investigate the influence of the particular material resistance to cavitation erosion and the corresponding distributions of P_{tot_load} , N_{eff}/N_{ref} and P_{ave_load} along the chord have been plotted in Figure 13. Note here that it can be assumed that the lower level of 30 kW m⁻² represents copper and that the level of 90 kW m⁻² represents stainless steel since there is no doubt that copper has a lower yield strength than stainless steel.

For $P_{threshold}$ of 30 kW m⁻², the maximum values of P_{tot_load} and N_{eff}/N_{ref} are found at 40% of the chord but at this location P_{ave_load} is relatively small compared to the rest of values farther downstream. This is because small vapor structures are collapsing at the cavity closure region for a long time duration ($0.7 T_{ref}$) but they are individually inducing relatively small P_{load} . This prediction is in agreement with the experimental results that show a high pitting rate at this location but with a relatively small deformation volume rate. The second peak value of P_{tot_load} is located at 53% of the chord. In this case, N_{eff}/N_{ref} is around 0.2 while P_{ave_load} shows its maximum value. This indicates that, at the region of the cloud collapses, the erosion intensity is very high but its time duration during one cycle is relatively

short. This is again in agreement with the experiment that shows a relatively smaller pitting rate but with the highest deformation volume rate in the same position.

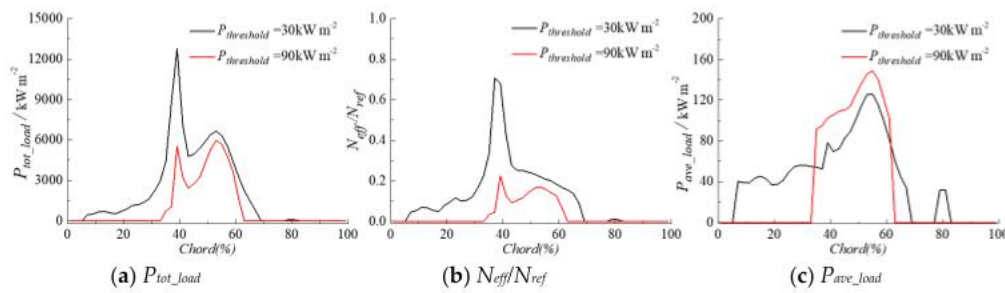


Figure 13. Distribution of P_{tot_load} , N_{eff}/N_{ref} and P_{ave_load} along the chord for $P_{threshold}$ levels of 30 and 90 kW m^{-2} .

When $P_{threshold}$ increases to 90 kW m^{-2} , the strongest erosions are also predicted at the sheet cavity closure and at the location where the main clouds collapse. However, it can be seen in Figure 13a,b that P_{tot_load} and N_{eff}/N_{ref} decrease significantly in the sheet cavity closure region but only slightly in the cloud collapse region when compared with the results obtained with 30 kW m^{-2} . Now the maximum P_{tot_load} is located at around 53% of the chord instead of 40%, which is also in accordance with the experimental results for the stainless steel specimen that showed the highest pitting rate at around the 50%. These numerical predictions confirm the existence of a threshold level and the fact that it permits the correction of the estimation of the cavitation erosion risk based on the cavitation aggressiveness. Increasing $P_{threshold}$, the contribution to erosion of the small intensity collapses taking place during a long time at the sheet cavity closure is dampened but it does not affect the results at the cloud collapse region where the P_{tot_load} is very high and clearly above $P_{threshold}$.

Therefore, the setting of $P_{threshold}$ is necessary to take into account the material resistance in the numerical prediction of cavitation erosion. Moreover, this is a concept that can also be used to explain the experimental observations found with different types of materials if it is assumed that it reproduces the effects of the material yield stress.

For example, the numerical P_{tot_load} and the experimental τ_n and τ_v have been normalized by their respective maxima along the chord and compared in Figure 14. It can be seen that the predicted results for $P_{threshold}$ of 30 kW m^{-2} compare well with the copper erosion measurements, and the ones for 90 kW m^{-2} compare well with stainless steel especially for the pitting rate observations. In addition, the numerical results show a zone with a low erosion intensity like a groove between the two maximum erosion picks for P_{tot_load} , which is due to the fact that in the simulations the boundary between the vapor and water phases is very well delimited whereas in reality these boundaries are quite unstable and the cavity wake is much fuzzier due to the flow turbulence [21].

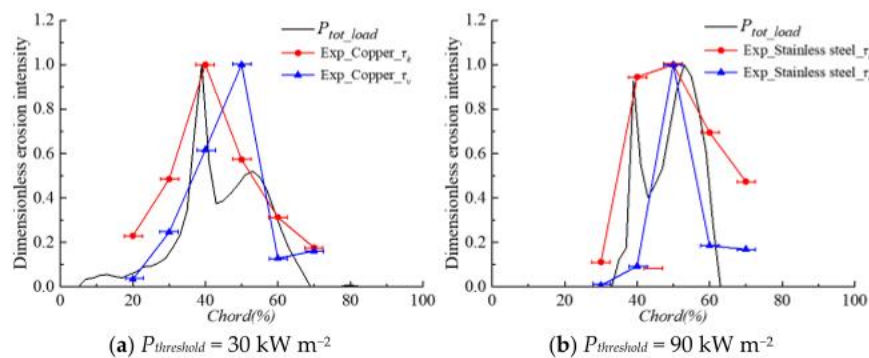


Figure 14. Comparison of dimensionless erosion intensity indicators between numerical and experimental results.

Given the good results obtained with the present simulations, the Sauer model has been further used to investigate the effect of the free stream velocity on the cavitation erosion power.

3.4. Free Stream Velocity Effects

Four different free stream water velocities, U_{inf} , have been simulated with the same numerical model corresponding to 15, 20, 25 and 30 m/s. The time step has been set inversely proportional to U_{inf} in order to keep the Courant number constant between all the simulations. In addition, the outlet pressure has been adjusted correspondingly in order to get always the same cavity length around the 40% of the chord as in the experiment. The model setup main parameters and the shedding frequencies calculated numerically and measured experimentally have been listed in Table 3. It can be seen that the simulations predict with good accuracy the shedding frequencies for any U_{inf} with a maximum percent deviation of 10.3%. Similarly to the results shown in Figure 4b, the time signals of the total vapor volume are repeatable from cycle to cycle for all the cases. Finally, the driving pressure has been based on the averaged instantaneous pressures over ten shedding cycles.

Table 3. Numerical and experimental shedding frequency results for the various flow conditions and numerical.

U_{inf} [m/s]	Time Step [s]	σ_{exp}	σ_{CFD}	f_{exp} [s ⁻¹]	f_{CFD} [s ⁻¹]	f_{dev} [%]
15	0.00004	1.55	1.55	96.1	106	10.3
20	0.00003	1.58	1.55	132.8	139	4.7
25	0.000024	1.60	1.55	175.5	177	0.8
30	0.00002	1.62	1.55	225.8	216	-4.3

To study the relationship between cavitation aggressiveness and flow velocity, the collapse efficiency proposed by Fortes-Patella et al., [39], $\eta_{collapse}$, has been used which quantifies the effective energy transfer between the potential power of the vapor volume and the actually erosive power. The value of $\eta_{collapse}$ is dependent on the initial gas pressure inside the bubble, P_{g0} , and the environment pressure, P_{∞} , but it is weakly dependent on the initial vapor volume so it can be calculated as:

$$\eta_{collapse} = 0.029(P_{g0}/P_{\infty})^{-0.54} \tag{25}$$

Equation (25) shows that, for a given P_{g0} , the efficiency is higher the higher is P_{∞} which means that for a given cavitation number, the collapses will release more energy for higher U_{inf} . In the present work, P_{g0} has been taken as 1500 Pa and P_{∞} has been calculated with the numerical cavitation number as done in [39]. Therefore, $\eta_{collapse}$ is a constant coefficient depending on U_{inf} as shown in Table 4. Then, the actual effective erosion power load, P_{eff_load} , can be calculated as:

$$P_{eff_load} = P_{tot_load}\eta_{collapse} \tag{26}$$

Table 4. Numerically calculated indicators of cavitation erosion for different flow velocities.

U_{inf} [m/s]	P_{tot_load} [kW m ⁻²]	P_{∞} [Pa]	P_{g0} [Pa]	$\eta_{collapse}$ [%]	P_{eff_load} [kW m ⁻²]	f_{CFD} [s ⁻¹]	P_{agg} [kW m ⁻² s ⁻¹]
15	5792	176,026	1500	38.0	2202	106	233,385
20	13,963	311,380	1500	51.7	7222	139	1,003,915
25	27,711	485,406	1500	65.7	18,216	177	3,224,249
30	48,033	698,105	1500	80.0	38,421	216	8,298,901

Since the experimentally obtained Strouhal number at different U_{inf} is constant with a value around 0.28 (see Table 1), the shedding frequency will increase linearly with U_{inf} and the collapsing frequency on the hydrofoil will also increase. Therefore, the cavitation erosion aggressiveness per unit time, P_{agg} , can be defined as:

$$P_{agg} = P_{eff_load}/T = P_{eff_load} \cdot f \tag{27}$$

All the calculated values of the various cavitation erosion indicators defined in this section have been listed in Table 4 and plotted in Figure 15, where several power law relations between them and U_{inf} have been found. Note that P_{tot_load} and P_{eff_load} are the accumulated potential power and the accumulated effective power for one complete shedding cycle, respectively, and P_{agg} is the accumulated effective power per unit time. The maximum P_{tot_load} along the chord, which is found at 40% of the chord for each U_{inf} because of no threshold has been considered, has also been selected to quantify the flow velocity effects.

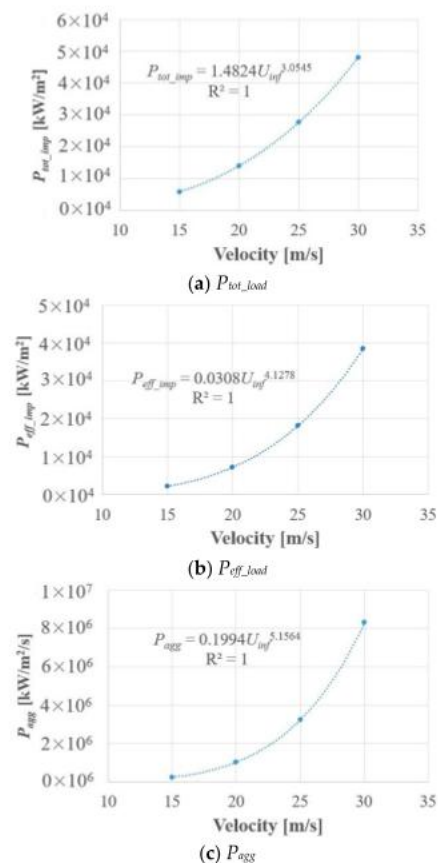


Figure 15. Predicted cavitation erosion intensity indicators at 40% of the chord as a function of flow velocity.

As observed in Figure 15a, P_{tot_load} increases approximately as U_{inf} to the third power for one shedding cycle, which is in accordance with the numerical results obtained by other researchers like Carrat et al., [23], Leclercq et al., [24] and Melissaris et al., [27], although they did not take into account the collapse efficiency. As observed in Figure 15b, P_{eff_load} increases approximately as U_{inf} to the fourth power when considering the efficiency which is in accordance with the numerical results obtained by Fortes-Patella et al. [39]. Finally, because the shedding frequency increases with the flow velocity, P_{agg} increases approximately as U_{inf} to the fifth power as shown in Figure 15c but this curve might rise faster, i.e., present a higher exponent, because the shedding frequency has been slightly overestimated for the lowest U_{inf} and underestimated for the highest U_{inf} in the present calculations. In addition, the experimental cavitation numbers are higher for the higher velocities than those in the numerical model, which implies higher environment pressures and higher collapse efficiencies for higher velocities. Consequently, the erosion rate may increase with an exponent higher than 5, which would be in agreement with the experimental investigations by Dular et al., [40,41] who found that the erosion damage followed a power law with n values from 5 to 8.

4. Conclusions

In the present study, the dynamic behavior and the erosion power of unsteady cloud cavitation on a 2D hydrofoil has been investigated numerically based on an energy balance approach. The influences of the driving pressure and of the cavitation model have been discussed in detail. The numerical prediction of erosion is in agreement with the experimental measurements and with the main erosion mechanisms. Moreover, the influence of flow velocity on erosion power has been quantified. As a result, the following conclusions have been obtained:

1. The selection of the driving pressure to estimate the power of the cavity collapse has a significant effect on the space-time distribution of the cavitation aggressiveness on the hydrofoil surface. The use of the average pressure gives more similar results to the experiment than the use of the instantaneous pressure.
2. The cavitation model influences significantly the power loaded on the hydrofoil surface both in terms of magnitude and spatial distribution along the chord. For the cases considered in the present study, the Sauer model performs better than the Kunz and Zwart ones.
3. Two main erosion mechanisms have been predicted that are in good agreement with experimental observations. One is induced by the high frequency of low-intensity collapses taking place at the closure region of the main sheet cavity attached to the hydrofoil surface. The other one is induced by the low frequency and high intensity collapses of the shed cloud cavities.
4. Power laws have been obtained that permit the calculation of the erosive cavitation intensity as a function of the flow velocity by taking into account the collapse efficiency and the shedding frequency. More specifically, the effective power load law grows with an exponent of 4, and the erosion aggressiveness per unit time grows with an exponent of 5.

Author Contributions: Methodology, L.G., J.C. and X.E.; software, L.G.; validation, L.G., J.C. and X.E.; investigation, L.G., J.C. and X.E.; writing—original draft preparation, L.G.; writing—review and editing, L.G., O.D.L.T. and X.E.; supervision, O.D.L.T. and X.E. All authors have read and agreed to the published version of the manuscript.

Funding: The present research work was financially supported China Scholarship Council.

Conflicts of Interest: The authors declare no conflict of interest.

References

1. Kim, K.H.; Chahine, G.; Franc, J.P.; Karimi, A. *Advanced Experimental and Numerical Techniques for Cavitation Erosion Prediction*; Springer: New York, NY, USA, 2014.
2. Li, Z.R. Assessment of Cavitation Erosion with a Multiphase Reynolds-Averaged Navier-Stokes Method. Ph.D. Thesis, Delft University of Technology, Wageningen, The Netherlands, 2012.
3. Hsiao, C.T.; Jayaprakash, A.; Kapahi, A.; Choi, J.K.; Chahine, G.L. Modelling of material pitting from cavitation bubble collapse. *J. Fluid Mech.* **2014**, *755*, 142–175. [[CrossRef](#)]
4. Fivel, M.; Franc, J.P.; Chandra Roy, S. Towards numerical prediction of cavitation erosion. *Interface Focus* **2015**, *5*, 20150013. [[CrossRef](#)] [[PubMed](#)]
5. Roy, S.C.; Franc, J.P.; Pellone, C.; Fivel, M. Determination of cavitation load spectra—Part 1: Static finite element approach. *Wear* **2015**, *344*, 110–119. [[CrossRef](#)]
6. Roy, S.C.; Franc, J.P.; Pellone, C.; Fivel, M. Determination of cavitation load spectra—Part 2: Dynamic finite element approach. *Wear* **2015**, *344*, 120–129. [[CrossRef](#)]
7. Joshi, S.; Franc, J.P.; Ghigliotti, G.; Fivel, M. SPH modelling of a cavitation bubble collapse near an elasto-visco-plastic material. *J. Mech. Phys. Solids.* **2019**, *125*, 420–439. [[CrossRef](#)]
8. Joshi, S.; Franc, J.P.; Ghigliotti, G.; Fivel, M. Bubble collapse induced cavitation erosion: Plastic strain and energy dissipation investigations. *J. Mech. Phys. Solids.* **2020**, *134*, 103749. [[CrossRef](#)]
9. Ochiai, N.; Iga, Y.; Nohmi, M.; Ikohagi, T. Numerical prediction of cavitation erosion intensity in cavitating flows around a Clark Y 11.7% hydrofoil. *J. Fluid Sci. Tech.* **2010**, *5*, 416–431. [[CrossRef](#)]

10. Wang, H.; Zhu, B. Numerical prediction of impact force in cavitating flows. *Trans. ASME J. Fluids Eng.* **2010**, *132*, 101301. [[CrossRef](#)]
11. Eskilsson, C.; Bensow, R.E.; Kinnas, S. Estimation of cavitation erosion intensity using CFD: Numerical comparison of three different methods. In Proceedings of the 4th International Symposium on Marine Propulsors, Austin, TX, USA, 31 May–4 June 2015.
12. Schnerr, G.H.; Sezal, I.H.; Schmidt, S.J. Numerical Investigation of Three-Dimensional Cloud Cavitation with Special Emphasis on Collapse Induced Shock Dynamics. *Phys. Fluids.* **2008**, *20*, 040703. [[CrossRef](#)]
13. Mihatsch, M.S.; Schmidt, S.J.; Adams, N.A. Cavitation erosion prediction based on analysis of flow dynamics and impact load spectra. *Phys. Fluids.* **2015**, *20*, 103302. [[CrossRef](#)]
14. Blume, M.; Skoda, R. 3D flow simulation of a circular leading edge hydrofoil and assessment of cavitation erosion by the statistical evaluation of void collapses and cavitation structures. *Wear* **2019**, *428*, 457–469. [[CrossRef](#)]
15. Nohmi, M.; Ikohagi, T.; Iga, Y. Numerical Prediction Method of Cavitation Erosion. In Proceedings of the ASME 2008 Fluids Engineering Division Summer, Jacksonville, FL, USA, 10–14 August 2008.
16. Li, Z.R.; Pourquie, M.; van Terwisga, T. Assessment of cavitation erosion with a URANS method. *Trans. ASME J. Fluids Eng.* **2014**, *136*, 041101. [[CrossRef](#)]
17. Fortes-Patella, R.; Reboud, J.L.; Briancon-Marjollet, L. A phenomenological and numerical model for scaling the flow aggressiveness in cavitation erosion. In Proceedings of the EROCAV Workshop, Val de Reuil, France, May 2004.
18. Patella, R.F.; Archer, A.; Flageul, C. Numerical and experimental investigations on cavitation erosion. In Proceeding of the 26th IAHR Symposium on Hydraulic Machinery and Systems, Beijing, China, 19–23 August 2012.
19. Koukouvinis, P.; Bergeles, G.; Gavaises, M. A cavitation aggressiveness index within the Reynolds averaged Navier Stokes methodology for cavitating flows. *J. Hydrodyn.* **2015**, *27*, 579–586. [[CrossRef](#)]
20. Ponkratov, D.; Caldas, A. Prediction of Cavitation Erosion by Detached Eddy Simulation (DES) and its Validation against Model and Ship Scale Results. In Proceeding of the 4th International Symposium on Marine Propulsors, Austin, TX, USA, 31 May–4 June 2015.
21. Dular, M.; Coutier-Delgosha, O. Numerical modelling of cavitation erosion. *Int. J. Numer. Methods Fluids.* **2009**, *61*, 1388–1410. [[CrossRef](#)]
22. Peters, A.; Sagar, H.; Lantermann, U.; el Moctar, O. Numerical modelling and prediction of cavitation erosion. *Wear* **2015**, *338*, 189–201. [[CrossRef](#)]
23. Carrat, J.B.; Fortes-Patella, R.; Franc, J.P. Assessment of cavitating flow aggressiveness on a hydrofoil: Experimental and numerical approaches. In Proceedings of the ASME 2017 Fluids Engineering Division Summer Meeting, Waikoloa, HI, USA, 30 July–3 August 2017.
24. Leclercq, C.; Archer, A.; Fortes-Patella, R.; Cerru, F. Numerical cavitation intensity on a hydrofoil for 3D homogeneous unsteady viscous flows. *Int. J. Fluid Mach. Syst.* **2017**, *10*, 254–263. [[CrossRef](#)]
25. Melissaris, T.; Bulten, N.; van Terwisga, T.J.C. On Cavitation Aggressiveness and Cavitation Erosion on Marine Propellers using a URANS Method. In Proceeding of the 10th International Symposium on Cavitation, Baltimore, MD, USA, 14–16 May 2018.
26. Schenke, S.; van Terwisga, T.J. An energy conservative method to predict the erosive aggressiveness of collapsing cavitating structures and cavitating flows from numerical simulations. *Int. J. Multiph. Flow* **2019**, *111*, 200–218. [[CrossRef](#)]
27. Melissaris, T.; Bulten, N.; van Terwisga, T.J. On the Applicability of Cavitation Erosion Risk Models With a URANS Solver. *Trans. ASME J. Fluids Eng.* **2019**, *141*, 101104. [[CrossRef](#)]
28. Leclercq, C. Simulation numérique du chargement mécanique en paroi généré par les écoulements cavitants, pour application à l'usure par cavitation des pompes centrifuges. Ph.D. Thesis, Université Grenoble Alpes, Grenoble Alpes, France, 2017.
29. Escaler, X.; Farhat, M.; Egusquiza, E.; Avellan, F. Dynamics and intensity of erosive partial cavitation. *Trans. ASME J. Fluids Eng.* **2007**, *129*, 886–893. [[CrossRef](#)]
30. Couty, P. Physical investigation of cavitation vortex collapse. Ph.D. Thesis, EPFL, Lausanne, Switzerland, 2002.
31. Geng, L.; Escaler, X. Assessment of RANS turbulence models and Zwart cavitation model empirical coefficients for the simulation of unsteady cloud cavitation. *Eng. Appl. Comp. Fluid Mech.* **2020**, *14*, 151–167. [[CrossRef](#)]

32. Coutier-Delgosha, O.; Fortes-Patella, R.; Reboud, J.L. Evaluation of the turbulence model influence on the numerical simulations of unsteady cavitation. *Trans. ASME J. Fluids Eng.* **2003**, *125*, 38–45. [[CrossRef](#)]
33. Zwart, P.J.; Gerber, A.G.; Belamri, T. A Two-Phase Flow Model for Predicting Cavitation Dynamics. In Proceedings of the International Conference on Multiphase Flow, Yokohama, Japan, 30 May–4 June 2004.
34. Schnerr, G.H.; Sauer, J. 2001 Physical and Numerical Modeling of Unsteady Cavitation Dynamics. In Proceedings of the 4th International Conference on Multiphase Flow, New Orleans, LA, USA, 27 May–1 June 2001.
35. Kunz, R.F.; Boger, D.A.; Stinebring, D.R.; Chyczewski, T.S.; Lindau, J.W.; Gibeling, H.J.; Venkateswaran, S.; Govindan, T.R. A Preconditioned Navier-Stokes Method for Two-Phase Flows with Application to Cavitation Prediction. *Comput. Fluids* **2000**, *29*, 849–875. [[CrossRef](#)]
36. Leclercq, C.; Archer, A.; Fortes-Patella, R. 2016 Numerical investigations on cavitation intensity for 3d homogeneous unsteady viscous flows. In Proceeding of the 28th IAHR Symposium on Hydraulic Machinery and Systems, Grenoble, France, 4–8 July 2016.
37. Asnaghi, A.; Feymark, A.; Bensow, R.E. Numerical investigation of the impact of computational resolution on shedding cavity structures. *Int. J. Multiph. Flow* **2018**, *107*, 33–50. [[CrossRef](#)]
38. Lu, N.X.; Bensow, R.E.; Bark, G. Indicators of erosive cavitation in numerical simulations. In Proceeding of the 7th international workshop on ship hydrodynamics, Shanghai, China, 16–19 September 2011.
39. Fortes-Patella, R.; Challier, G.; Reboud, J.L.; Archer, A. Energy Balance in Cavitation Erosion: From Bubble Collapse to Indentation of Material Surface. *Trans. ASME J. Fluids Eng.* **2013**, *135*, 011303. [[CrossRef](#)]
40. Bachert, B.; Dular, M.; Baumgarten, S.; Ludwig, G.; Stoffel, B. Experimental investigations concerning erosive aggressiveness of cavitation at different test configurations. In Proceedings of the ASME Heat Transfer/Fluids Engineering Summer Conference, Westin Charlotte, NC, USA, 11–15 July 2004.
41. Dular, M.; Sirok, B.; Stoffel, B. Influence of gas content in water and flow velocity on cavitation erosion aggressiveness. *Stroj. Vestn. J. Mech E.* **2005**, *51*, 132–145.



© 2020 by the authors. Licensee MDPI, Basel, Switzerland. This article is an open access article distributed under the terms and conditions of the Creative Commons Attribution (CC BY) license (<http://creativecommons.org/licenses/by/4.0/>).